



NTNU – Trondheim
Norwegian University of
Science and Technology

X-ray Studies of Capture, Storage and Release of CO₂

Karin Hveding Rustenberg

Master of Science in Physics and Mathematics

Submission date: June 2012

Supervisor: Jon Otto Fossum, IFY

Norwegian University of Science and Technology
Department of Physics

Abstract

We show experimentally that CO₂ intercalates into the interlayer space of the synthetic smectite clay Li-fluorohectorite (LiFh). The intercalation occurs for a range of conditions in terms of pressure (5 bar to 20 bar) and temperature (-20 °C to 5 °C). The mean basal spacing of the clay layers in LiFh intercalated by CO₂ is found to be approximately 12.0 Å.

We observe that the dynamics depends on the pressure, with a higher intercalation rate at increased pressure. Even under pressure of 20 bar, intercalation of CO₂ is slower than H₂O intercalation in fluorohectorites by orders of magnitude.

In situ observations show that LiFh is able to retain CO₂ in the interlayer space at room temperature, and the CO₂ only starts leaving the clay at temperatures exceeding 30 °C. Hydrated and CO₂-intercalated clays are indistinguishable by use of X-ray diffraction alone. The difference in behavior at higher temperatures is used as an additional confirmation that intercalation of residual water is not the cause of the observed swelling.

Furthermore, we report a new intercalation state corresponding to intercalation of more than one layer of CO₂ into the interlamellar space, and have also observed changes in the intercalation state of a monohydrated LiFh sample under exposure to CO₂.

We believe that the findings, concerning both intercalation and deintercalation, could be relevant for application of clays related to capture, transport or storage of CO₂.

Abstract

Vi viser eksperimentelt at CO₂ absorberes i syntetisk Li-fluorohektoritt (LiFh) leire, hvor den legger seg mellom leirelagene og blir en del av strukturen. Dette har blitt vist for flere trykk (5 bar til 20 bar) og temperaturforhold (-20 °C til +5 °C). Den gjennomsnittlige stableavstanden for leirelagene i LiFh interkalert med CO₂ er 12.0 Å, som tilsvarer en ekspansjon av enhetscella med 1.8 Å.

Vi har observert at dynamikken er trykkavhengig, der høyere trykk fører til raskere interkalering. Likevel er prosessen - selv ved 20 bar - flere størrelsesordre tregere enn interkalering av vann i fluorohektoritt.

Forsøk viser at LiFh kan holde på CO₂ ved romtemperatur, men ved temperaturer over 30 °C begynner CO₂ å forlate leira. Basert på røtgendifraksjon alene er det umulig å skille leireprøver med ett vannlag og CO₂ interkalert fra hverandre. Vi har likevel sett at slike prøver oppfører seg forskjellig ved oppvarming, som har gjort det mulig å utelukke at den observerte ekspansjonen skyldes interkalering av fuktighet.

Vi har observert en ny tilstand som tilsvarer mer enn ett lag CO₂ i mellomlaget til LiFh. I tillegg har vi registrert strukturelle endringer i en fuktig prøve som ble utsatt for CO₂ ved 20 bar.

Vi tror at funnene våre, både hva angår interkalering og leires evne til å holde på CO₂, kan være av relevanse for bruk av leire til fanging, transport og lagring av CO₂.

Contents

1	Theory	1
1.1	Clays	1
1.1.1	Clay structure	1
1.1.2	Intercalation	4
1.1.3	Hectorite clays	5
1.2	Carbon dioxide	7
1.3	Nitrogen	8
1.4	X-ray diffraction	9
1.5	X-ray sources	19
1.5.1	Electron impact source	19
1.5.2	Synchrotrons	19
1.6	Infrared spectroscopy	23
1.7	Fourier Transform Infrared Spectroscopy	27
2	CO₂ Intercalation Experiment	31
2.1	Experimental setup X-ray diffraction	31
2.1.1	Nanostar Bruker system	31
2.1.2	Sample holder	32
2.1.3	X-ray setup NTNU	34
2.2	Experimental method	36
2.2.1	Experiment at NTNU	36
2.2.2	Infrared Spectroscopy	38
3	Data analysis and discussion	39
3.1	Data acquisition and processing	39
3.2	Discussion of X-ray data	43

3.2.1	Intercalation	43
3.2.2	Heating and deintercalation	55
3.2.3	Humidity test	61
3.2.4	Hydrated CO ₂ intercalation states	67
3.2.5	Natural hectorite	73
3.3	Discussion of IR data	75
4	Concluding remarks	79
Appendix A	Additional WAXS data	85
A.1	Supplementary figures: Intercalation	86
A.2	Supplementary figures: Heating	91
A.2.1	Stepwise heating	91
A.2.2	Deintercalation at fixed temperature	92
A.3	Hydration states - peak shape	95
Appendix B	Preliminary studies	97
B.1	Experimental results MAX-lab	98
B.1.1	Exposure to high pressure CO ₂	98
B.1.2	Choice of clay	98
B.1.3	Particle size	100
B.1.4	Temperature dependence	100
B.1.5	Return to ambient conditions	102
Appendix C	Journal article draft	105
Appendix D	Poster Lofoten	113
Appendix E	CAS proceedings	117
	List of Figures	128
	Bibliography	129

Preface

This Master's thesis presents the work and research carried out in my final year of studies for the degree MSc in Technology in Applied Physics at the Norwegian University of Science and Technology (NTNU). The work has been carried out at the Complex Systems and Soft Materials Group (Complex) at NTNU, and preliminary experiments were conducted at MAX-lab in Lund, Sweden. While working on this topic, I have been privileged to get hands-on experience and knowledge of tools such as IR spectroscopy and Synchrotron - and laboratory X-ray diffraction equipment. The learning curve throughout the year has been steep, but it has been a very rewarding personal experience.

Motivation

At the Laboratory for Soft and Complex Matter Studies, my supervisor, Professor Jon Otto Fossum, has been studying phenomena in clays for years. Clays are *complex* materials which display many unique and interesting properties.

Clay minerals exist in abundance in the crust of the earth and are materials based on a two-dimensional stack of inorganic layers [1]. The subgroup of clays known as smectites has the ability to swell when other molecules are incorporated, or intercalated, into the space between the clay layers.

Water intercalates naturally in clays, and this phenomenon has been extensively studied with a wide range of techniques, such as neutron [2, 3] and X-ray scattering [4–7], NMR spectroscopy [8, 9], tracer experiments

[10] and numerical modeling [11–13]. It is also possible to intercalate other materials into the clay structure, to change and improve its properties [14].

In recent years, due to the focus on anthropogenic CO₂ emissions and its environmental impact, attention has been drawn to the interaction of CO₂ and clays, mainly because geological structures are being investigated as storage sites for CO₂. The cap-rock formations, which act as flow-barriers and seals in this context, are known to often contain high concentrations of clay minerals [15]. If clay rich formations are to be used for CO₂ storage, it is important that the gas is retained and does not leak back into the atmosphere [16, 17].

Experiments have shown that CO₂ intercalates in smectite clays, both in supercritical [18–23], and in gaseous or liquid form [22–28]. Experiments performed by the group of my supervisor, have also shown that CO₂ is able to intercalate Na-Fluorohectorite clay [24] at conditions close to ambient.

The motivation for this project was to study the interaction of CO₂ and smectite clays by use of Wide-Angle X-ray Scattering (WAXS). In addition to map CO₂ intercalation at different conditions in terms of temperature and pressure, we also wanted to verify that CO₂ was in fact intercalated in the clay - by use of infrared spectroscopy (IR). I also performed experiments where clay intercalated with CO₂ was heated, to study at what conditions CO₂ is retained in the clay structure.

The experiments performed for this Master's thesis are based on results obtained by Erlend G. Rolseth for his Master's thesis [29] and the resulting article by Hemmen et al [24], in addition to my own experimental results in association with my Master's project in the fall of 2011 [30]. A summary of the main findings of this project are presented in Appendix B.

Based on some of my findings, I have drafted a journal article in collaboration with Henrik Hemmen. It is presented in Appendix C

Karin Rustenberg

Trondheim, June 15, 2012

Acknowledgments

I would like to thank my supervisor, Jon Otto Fossum, for giving me the opportunity to work within an outstanding research environment of inspiring and skilled people. I consider myself lucky to have been able to visit some of the finest synchrotron facilities in Europe and work with such an interesting topic. It has been very educational and rewarding.

I am tremendously grateful for all guidance and help from PhD student Henrik Hemmen. I would probably not have learned this much if it wasn't for his creativity and ideas for new experiments and ability to provide sensible answers to my stupid questions, not to mention his patience, welcoming attitude and friendly advice.

Our lab technician, Ole Tore Buset, has always helped me out whenever the X-ray machine broke down. Without his help I would not have been able to get as far as I got.

Also, I would like to thank my great friends and colleagues with whom I have spent numerous hours by the coffee table. Their company and motivation got me through the disappointment of failed experiments and has been a source of many entertaining discussions. You will be missed.

Last, but not least, I would like to thank my family for all your support and motivation, and for raising me to believe anything is possible.

Chapter 1

Theory

This chapter gives an overview the theoretical background relevant for this thesis. Clay theory is presented, as well as the concepts of X-ray diffraction and its application to studies of intercalation in clays. A short introduction to infrared spectroscopy is also provided.

1.1 Clays

Clays are one of the most abundant materials in the earth's crust [31]. They represent one of the traditional materials, whose applications have been of importance throughout human history. In recent times the interest in clays have increased, both in modern materials science, but also because of their potential applications to CO₂ capture and retention. Due to their unique electrical, mechanical and rheological properties, they are called complex materials. This places clays in a group of interesting materials, such as liquid crystals, colloids, polymers and bio-materials [32]

1.1.1 Clay structure

Clays are categorized by their structure, the atoms contained in it and their layer charge. The structure is defined by tetrahedral and octahedral

CHAPTER 1 THEORY

sheets that may condense in either 1:1 or 2:1 proportions. The tetrahedral sheets consist of cations coordinated with four oxygen (O) atoms each, and the tetrahedra are connected by sharing three corners. In the octahedral sheets, the octahedra are connected by sharing edges. Each octahedron is composed of one cation coordinated with six oxygen atoms or hydroxyl (OH^-)¹ groups.

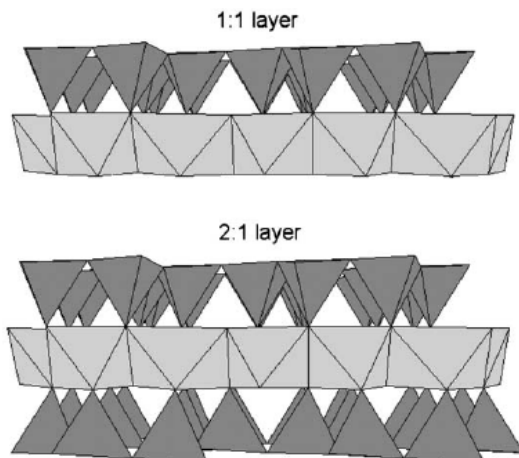


FIGURE 1.1: The composition of the tetrahedral (dark) and octahedral (gray) sheets that makes up one clay layer their respective layer structures. 1:1 (top) and 2:1 layer structures (bottom). Adapted from [33].

The stacking of these sheets determines the structure of the clay. The 1:1 layer configuration is characterized by an alternate stacking of octahedral and tetrahedral sheets. In the 2:1 layer configuration there is a repetition of one octahedral layer sandwiched between two tetrahedral layers. This structure also has the potential of variations with *interlayer* or *guest* cations, which are positioned between the layers [33]. Figure 1.1 shows the general structure of the 1:1 and 2:1 layer configurations. Most clay particles can be described as disc-shaped, and consist of up to hundreds of 1:1 or 2:1 layers stacked on top of each other.

¹Usual cations in the tetrahedral sheet are Si^{4+} , Al^{3+} and Fe^{3+} , while in the octahedral sheet Al^{3+} , Fe^{3+} , Mg^{2+} and Fe^{2+} are most common.

Unit cell

The unit cell of the 1:1 layered structure includes six octahedral sites and four tetrahedral. The 2:1 layer structure is characterized by six octahedral and eight tetrahedral sites.

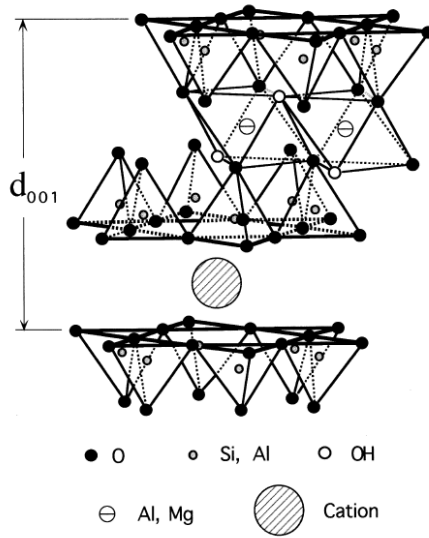


FIGURE 1.2: The structure of the unit cell of a typical 2:1 layered silicate clay. The basal spacing d_{001} is determined by the layer stacking geometry and potential guest substances between the layers [34].

Structures with all six octahedral sites occupied are known as trioctahedral, while the structure is said to be dioctahedral if only four of them are occupied. The structural formula of the unit cell is often reported on the basis of a half unit cell, and is thus based on three octahedral sites [33]. The basal spacing d_{001} is defined as the distance from a certain plane in one layer, to the corresponding plane in the closest parallel layer (see Figure 1.2). The basal distance includes the stacking geometry as well as any material present between layers [35].

CHAPTER 1 THEORY

Layer charge

When the tetrahedral and octahedral sheets form a layer, the structure can either be electrically neutral or have a net negative charge. A negative layer charge can arise from substitution of Al^{3+} for Si^{4+} in tetrahedral sites, substitution of Al^{3+} or Mg^{3+} for lower charge cations in octahedral sites, or presence of vacancies. The net negative charge of the clay layers is a very important feature of 2:1 layered clays, as it induces occupancy of the interlayer space by exchangeable cations. The attractive electrostatic forces between layers and cations minimize the distance between the cations and the negatively charged sites. Most 1:1 layered structures have a neutral layer charge [33, 36].

1.1.2 Intercalation

The phenomenon of intercalation, or swelling, is one of the most interesting characteristics of clays. This ability is possessed by a group of 2:1 layered silicates called smectites. These clays have a relatively low layer charge, which makes it possible for the unit cell to expand and host extraneous molecules within the space between the interlayer. The clay *swells* if this incorporation of guest substances causes an expansion of the unit cell. This is done in such a way that the *host layer*, the joined layer of tetrahedral and octahedral sheets, remains essentially unchanged. The space between the layers, which originally was occupied only by the interlayer cation, is often called the *guest layer* or *interlayer space* because of its ability to incorporate substances. The intercalation process depends on the layer charge and Coulomb interaction of clay layers and interlayer cations, as well as the intercalated molecules [34, 37, 38].

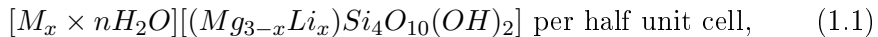
The most common type of intercalation is inclusion of water vapor in clays, which hydrates the interlayer cations. The discrete numbers of water layers or hydration states from this intercalation process are often denoted by 0 WL, 1 WL, 2 WL and 3 WL for the different hydration states respectively. The structures are quite well ordered along the stacking direction. The amount of water that is able to intercalate depends on the layer charge of the clay, the interlayer cation and the clay type. Furthermore, the water

vapor pressure around the particle, or water activity in a solution, has impact on the water absorption [5].

Recent research in terms of computer simulations and experiments show the possibility of intercalation of CO_2 in smectite clays [18–29]. Even though one does not yet have a satisfactory understanding of the molecular mechanisms of intercalation, clay minerals have been suggested a potential material for carbon capture and storage [29, 37]. In order to evaluate use of clays for this purpose, it is important to map CO_2 intercalation and retention at different conditions.

1.1.3 Hectorite clays

Hectorite is a trioctahedral smectite clay. It is composed of silicon tetrahedrons (SiO_4) and octahedrons of hydroxyls and magnesium (Mg^{2+}) and lithium (Li^+) ions. The composition of hectorites is given by



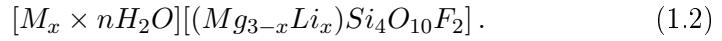
where x is the proportion of Li-ions per half unit cell. The first bracket expression denotes the guest layer, where M denotes a monovalent inter-layer cation and $n\text{H}_2\text{O}$ is a discrete number of water layers. The last set of brackets denotes the host layer [33].

Fluorohectorite

Fluorohectorite clays represent an extreme within the group of smectite clays in terms of size and charge [38]. The clay particles have a layer charge of approximately $1.2 e^-$ per unit cell can have a lateral size of up to $2 \mu\text{m}$. Fluorohectorites are synthetic clays, where all hydroxyl groups have been replaced by fluorine ions (F^-). They are used as representative model systems of natural smectite clays due to the small amount of impurities (which could mask the behavior of the clay), and the homogeneous layer charge distribution relative to their natural counterparts [39].

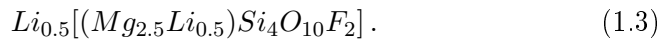
CHAPTER 1 THEORY

The fluorohectorites are categorized by their interlayer cation. This results in the general formula



Commonly used fluorohectorites are sodium fluorohectorite (NaFh) and lithium fluorohectorite (LiFh) where Na and Li are the interlayer cations, respectively. Through a cation exchange process one can also fabricate synthetic clays with mono- or multivalent interlayer cations, such as copper (CuFh), iron (FeFh) or niobium (NbFh).

Lithium fluorohectorite is a clay type which has proved convenient for studying intercalation of CO₂ in synthetic clays, due to the relatively fast process compared to NaFh. The formula of dehydrated LiFh is



1.2 Carbon dioxide

Carbon dioxide (CO_2) is a colorless and odorless gas which is found everywhere in nature. It is one of the main products of combustion of organic material. CO_2 is a greenhouse gas, which means it is one of the gases which greatly influence the temperature on the earth's surface. Lately, interest has been raised to reduce the human-caused increase of CO_2 in the atmosphere, because of the effect it has on the earth's climate. One area of focus has been technology to capture and sequester CO_2 [38, 40].

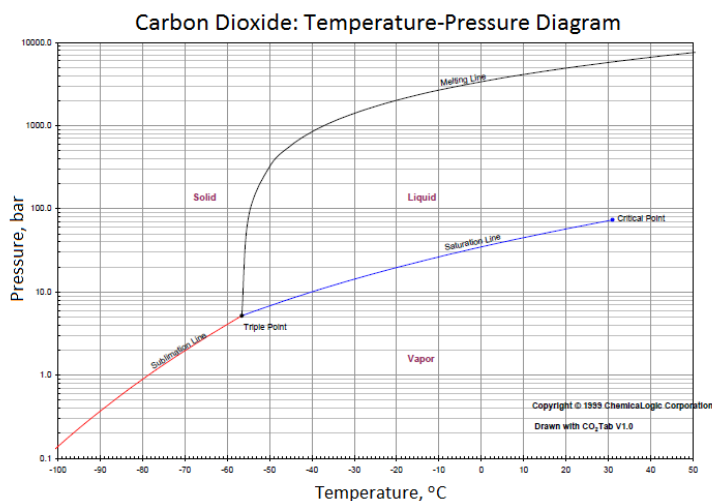


FIGURE 1.3: Temperature-pressure phase diagram of CO_2 . CO_2 has three aggregation states; solid, liquid and gas/vapor.

CO_2 is a linear molecule, consisting of a central carbon atom which forms double covalent bonds with two oxygen molecules. Because of the linearity, the molecule has no net dipole moment. Figure 1.3 shows the phase diagram for CO_2 , and makes it clear that CO_2 exists in three aggregation states; gas/vapor, liquid and solid.

CHAPTER 1 THEORY

1.3 Nitrogen

Nitrogen (N_2) is a diatomic gas consisting of two nitrogen atoms which makes up 78.09% of the air in the atmosphere. Because it has no odor, color or taste, is nonflammable and has a nonreactive nature with many materials, it is often used as an inert gas. At its boiling point, $-195.5\text{ }^\circ\text{C}$, nitrogen condenses to a colorless liquid [41].

1.4 X-ray diffraction

X-ray diffraction can be used to study basal spacings of layered nano-materials, such as clays. This section gives an introduction to scattering theory. A good starting point is to evaluate scattering from electrons, which are structureless particles. Subsequently, scattering from more complex systems will be discussed; atoms, molecules and clay powder.

Scattering from an electron

When an electron is placed in the electric field of an X-ray beam (see Figure 1.4) with wave vector \mathbf{k} , it will start oscillating in phase with the field. Consequently, it acts as a small dipole and radiates with the same frequency as the incoming wave, assuming elastic scattering, or *Thomson scattering*. From Maxwell's equations, the radiated field at a distance R from the electron can be derived. If Ψ is the angle between \mathbf{k} and the observation point, the relation between the amplitudes of the radiated and incident waves at a distance R from the electron is [42]

$$\frac{E_{rad}(R, t)}{E_{in}} = - \left(\frac{-e^2}{4\pi\epsilon_0 mc^2} \right) \frac{e^{ikR}}{R} \cos \psi, \quad (1.4)$$

where

$$r_0 = \left(\frac{-e^2}{4\pi\epsilon_0 mc^2} \right) = 2.82 \times 10^{-5} \text{ \AA}. \quad (1.5)$$

The above is known as the classical electron radius, or the *Thomson scattering length*, and describes the electron's ability to scatter. In calculating the amplitude at an observation point $X(R, \psi)$ in (1.4), the factor $\cos \psi$ has been included to account for the angle change of the wave vector.

The ratio between the radiated and incident intensities, $I = |E|^2$, leads to the definition of the *differential cross-section*. This term is defined as the number of scattered photons per second into a solid angle $d\Omega$, divided

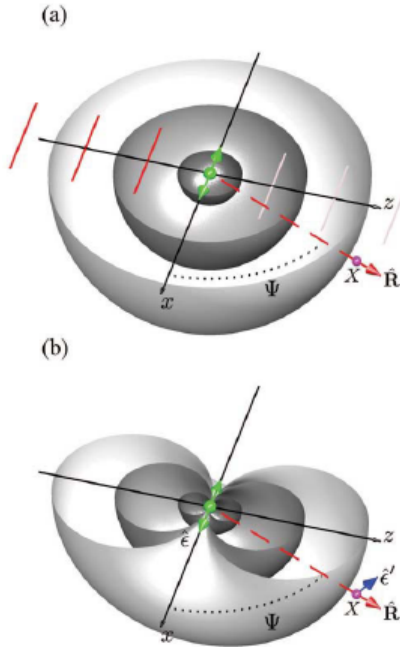


FIGURE 1.4: The classical description of the scattering of an X-ray by an electron. (a) The electric field of an incident plane wave sets an electron in oscillation which then radiates a spherical wave. The incident wave propagates along the z-axis and its electric field is polarized along x. The observation point X lies in the same plane as the polarization, and the observed acceleration has to be multiplied by a factor $\sin \Psi$. (b) From geometry, $\sin \Psi = -\hat{\epsilon} \cdot \hat{\epsilon}'$ where $\hat{\epsilon}'$ represents the polarization of the incident (scattered) beam. The effect of this factor on the radiated wave is illustrated by surfaces of constant amplitude. Adapted from [42].

1.4 X-RAY DIFFRACTION

by the incident flux multiplied with the same solid angle. The differential cross-section for Thomson scattering is given by

$$\left(\frac{d\sigma}{d\Omega}\right) = r_0^2 P \quad (1.6)$$

where P is the polarization factor, which depends on the X-ray source [42]:

$$P = \begin{cases} 1 & \text{synchrotron: vertical scattering plane} \\ \cos^2\psi & \text{synchrotron: horizontal scattering plane} \\ \frac{1}{2}(1 + \cos^2\psi) & \text{unpolarized source.} \end{cases} \quad (1.7)$$

Scattering from an atom

When considering scattering by an atom, one must take into account that the atom consists of one or more scattering electrons that move about the center of the atom. The scattered radiation is a superposition of contributions from different volume elements. The electron distribution is given by the number density at a distance \mathbf{r} from the mass center, $\rho(\mathbf{r})$. The distribution introduces the concept of the *atomic form factor*, which is the Fourier transform of $\rho(\mathbf{r})$:

$$f(\mathbf{Q}) = \int \rho(\mathbf{r}) e^{i\mathbf{Q}\cdot\mathbf{r}} \quad (1.8)$$

$$\mathbf{Q} = \mathbf{k}_i - \mathbf{k}_f. \quad (1.9)$$

\mathbf{Q} is the scattering vector which describes the difference between the incident and scattered wave vectors, while i and f denote the initial and final (scattered) wave vectors, respectively (see Figure 1.5). The magnitude of the atomic scattering length is obtained by multiplying the form factor with the Thomson scattering length, which means that $f(\mathbf{Q})$ describes the total scattering power of the atom. In the forward direction ($\mathbf{Q} = 0$), the form factor is simply the atomic number Z .

CHAPTER 1 THEORY

The intensity of the scattered radiation is proportional to the absolute square of $|f(\mathbf{Q})|^2$. Since a detector measures the intensity of radiation, the imaginary part in equation (1.8), the phase factor, is lost [42]. Thus, it is not possible to obtain the charge distribution directly by an inverse Fourier transform of the intensity.

The Fourier transform is a very powerful tool in scattering theory. It provides a mathematical relationship between the morphology of investigated structures and the observed scattering patterns.

Scattering from a unit cell

Crystal structures can be described by the basis of their unit cell. Conversely, scattering by the unit cell also describes scattering by a crystal. The unit cell can consist of different atoms. The form factor of the unit cell, F_{str} , is given as the sum of contributions from each atom j in the unit cell. \mathbf{r}_j is the position of the j 'th atom in the unit cell, and f_j is its atomic form factor:

$$F_{str}(\mathbf{Q}) = \sum_j f_j \mathbf{Q} e^{i\mathbf{Q}\mathbf{r}} d\mathbf{r} e^{-M_j}. \quad (1.10)$$

Here, e^{-M_j} is known as the Debye-Waller factor, which represents a reduction in scattering intensity as a result of lattice vibrations. The Debye-Waller factor is different for each type of atom since lighter atoms vibrate more easily than heavier ones [42].

Bragg's law of diffraction

The defining property of a crystalline material is its periodicity. With the scattering vector given by (1.9), and assuming elastic scattering, one can conclude that the size of the incident and scattered wave vectors are of the same magnitude, k .

At certain scattering angles there will be constructive interference between waves scattered by different planes. These angles are said to fulfill the

1.4 X-RAY DIFFRACTION

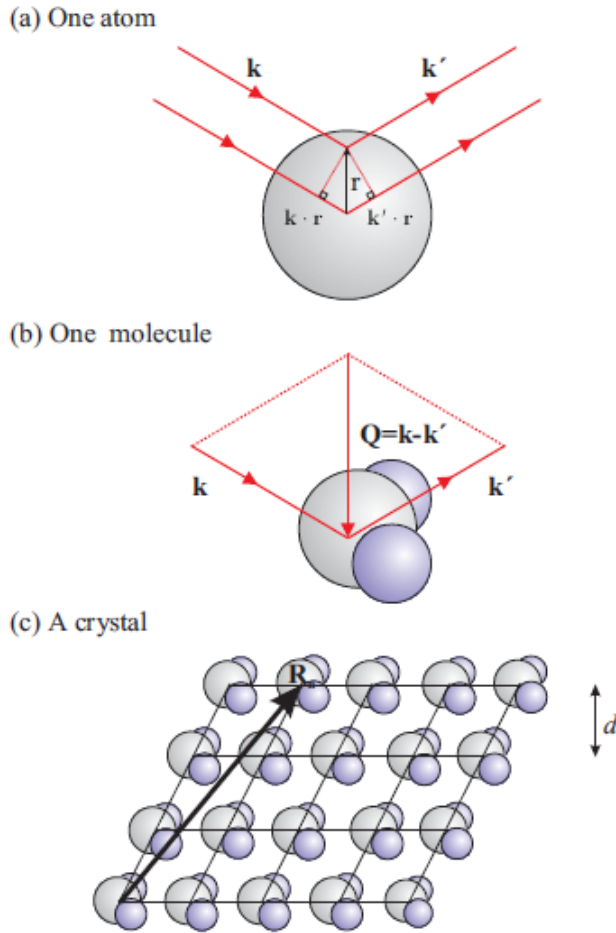


FIGURE 1.5: (a) Scattering from an atom. An X-ray with wavevector \mathbf{k} scatters from an atom to the direction specified by \mathbf{k}' . The scattering is assumed to be elastic, which means $|\mathbf{k}| = |\mathbf{k}'| = 2\pi/\lambda$. The difference in phase between a wave scattered at the origin and one at a position \mathbf{r} is $(\mathbf{k} - \mathbf{k}') \cdot \mathbf{r} = \mathbf{Q} \cdot \mathbf{r}$. This defines the scattering vector \mathbf{Q} . (b) The scattering from a molecule. The relation between \mathbf{k} , \mathbf{k}' and \mathbf{Q} is shown. (c) The scattering from a crystal lattice, where the unit cells are placed at positions \mathbf{R}_n , and d is the lattice spacing [42].

CHAPTER 1 THEORY

Bragg condition. The phase shift for waves scattered from two different planes is an integer number of 2π . Thus the difference in path length is an integer number of the wavelength λ . If the angle of incidence to a set of adjacent lattice planes separated by a distance d_{hkl} is the Bragg angle θ ; then the Bragg equation is given by

$$2d_{hkl} \sin \theta = n\lambda. \quad (1.11)$$

Reciprocal space and the Laue condition

There is an inverse relation between the structure and form of a sample and the detected diffraction pattern. The *reciprocal space* can be used to illustrate and understand this relationship. It is based on the fact that the Fourier transform can take us from real space to reciprocal space, or vice versa. The scattering vector \mathbf{Q} is a vector in reciprocal space. The reciprocal vector that corresponds to the distance between two scatterers in the reciprocal space is given by the *reciprocal lattice vector*. This vector gives the allowed directions of scattering, and is given by

$$G_{hkl} = h\mathbf{a}^* + k\mathbf{b}^* + l\mathbf{c}^*. \quad (1.12)$$

Here hkl are the miller indices, and \mathbf{a}^* , \mathbf{b}^* and \mathbf{c}^* are the reciprocal lattice vectors which satisfy the conditions

$$\mathbf{a} \cdot \mathbf{a}^* = \mathbf{b} \cdot \mathbf{b}^* = \mathbf{c} \cdot \mathbf{c}^* = 2\pi \quad (1.13)$$

and

$$\mathbf{a}^* \cdot \mathbf{b} = \mathbf{a}^* \cdot \mathbf{c} = \mathbf{b}^* \cdot \mathbf{c} = \mathbf{c}^* \cdot \mathbf{b} = 0. \quad (1.14)$$

The reciprocal equivalent to Bragg's law is the Laue condition, which is fulfilled when the scattering vector \mathbf{Q} is equal to \mathbf{G}_{hkl}

1.4 X-RAY DIFFRACTION

$$\mathbf{Q} = \mathbf{G}_{hkl} = 2\pi \frac{\hat{\mathbf{n}}_{hkl}}{d_{hkl}}. \quad (1.15)$$

Compared to (1.12) this equation describes the crystal structure in terms of crystal planes separated by d_{hkl} , rather than atomic positions. $\hat{\mathbf{n}}_{hkl}$ is the unit vector perpendicular to the plane (hkl) .

The Laue condition imposes limitations on the scattering, known as selection rules. When summing over the selection rule the *interference function* $S_{lc}(\mathbf{Q})$ for an ideal crystal is obtained. $S_{lc}(\mathbf{Q})$ is dependent on the size and orientation, or stacking direction, of the crystallites.

Scattering from layered clay

The unit cell structure factor (1.10) is given as a function of the scattering vector \mathbf{Q} which is defined by discrete indices hkl (1.15). This yields that the structure factor is not continuous in \mathbf{Q} .

Since clays are described as a composition of layers, they can in many ways be considered two dimensional. This allows for a change from discrete to continuous structure factor. If the system is considered to be centrosymmetric one can define a *layer structure factor* $G(\mathbf{Q})$ as

$$G(\mathbf{Q}) = \sum_j n_j f_j(\mathbf{Q}) \cos(\mathbf{Q}z_j) \cdot e^{-M_j}, \quad (1.16)$$

where n_j is the number of atoms of type j located in a distance z_j from the origin of the system. It is clear that $G(\mathbf{Q})$ is continuous in \mathbf{Q} [43].

Diffraction from clay powder

When studying scattering from a layered structure, like clay, Bragg peaks corresponding to diffraction by the layers of the sample can be observed. The dominant scattering direction of clays is along the 001 direction, which corresponds to the direction perpendicular to the clay layers. In X-ray

CHAPTER 1 THEORY

diffraction experiments with clays, the main contribution to the scattered intensity comes from the interlayer spacing, d_{001} .

A clay powder ideally consists of many thousands of microcrystallites with random, *isotropic*, orientations. This means that there is always a fraction of the crystallites that fulfills the Laue condition necessary to observe diffraction.

Another factor that must be taken into account in diffraction experiments is the *Lorentz-polarization factor* $L_p(Q)$, which is an important experimental quantity that controls the X-ray intensity with respect to diffraction angle. The Lorentz factor accounts both for the powder ring distribution factor, ψ , which describes the number of crystals favorably oriented for diffraction at any Bragg angle, and the irradiated volume of a crystal as a function of 2θ .

Taking all factors into account the measured intensity for scattering experiments is given by

$$I(Q) = |G(Q)|^2 S_{lc}(Q) L_p(Q). \quad (1.17)$$

The unit cell structure factor, the interference function and the Lorentz factor all contribute to the intensity. Because of the isotropic distribution of the clay particles in the powder the diffraction pattern is shaped like a circular cone. If any guest substances are intercalated in the clay it can change the d_{001} -spacing and result in a change in both the layer structure factor and the interference function. One result is a decreased cone radius, and due to this effect intercalation can be observed by X-ray diffraction.

Diffraction peaks

Peak shape and width could be important parameters in analysis of an X-ray diffraction pattern. However, for most studies related to intercalation processes in clays the peak positions and intensities are the most important parameters. Still, providing an as good as possible peak description is always beneficial.

1.4 X-RAY DIFFRACTION

The width of the peaks is a result of contributions from the sample and instrument. In many cases the width of the instrument is so small that one can assume that the measured width is approximately equal to that of the signal produced by the sample. Still, in some cases it is necessary to separate the two contributions. The Pseudo-Voigt function makes this possible.

The measured signal is a convolution of a Gaussian instrument function and a Lorentzian function from the scattered intensity, which is described by a Voigt function. The Pseudo-Voigt function is a linear sum which approximates the respective contributions.

$$\Phi(q) = \frac{\eta}{\pi\Gamma\sqrt{\ln 2} \left(1 + \left(\frac{q-q_c}{\Gamma\sqrt{\ln 2}}\right)^2\right)} + \frac{(1-\eta)}{\sqrt{\pi}\Gamma} e^{-\left(\frac{q-q_c}{\Gamma}\right)^2} \quad (1.18)$$

$\Phi(q)$ is related to the measured intensity by $I(q) = C(q)\Phi(q)$, where $C(q)$ is related to the scattering structure and polarization factors, and can be approximated to constant in the region around each (001) peak since it varies slowly with q compared to the peak widths [5]. Γ is the experimental width at half maximum and η a mixing constant on the interval $[0, 1]$ which changes the shape of the curve from Gaussian to Lorentzian. The widths of the Gaussian and Lorentzian components are given by Ω_G and Ω_L , respectively. They are related to Γ and η by

$$\Gamma = (\Omega_G^5 + 2.6927\Omega_G^4\Omega_L + 2.4284\Omega_G^3\Omega_L^2 + 4.471\Omega_G^2\Omega_L^3 + 0.0784\Omega_G\Omega_L^4 + \Omega_L^5)^{1/5} \quad (1.19)$$

$$\eta = 1.36603\frac{\Omega_L}{\Gamma} - 0.47719\frac{\Omega_L^2}{\Gamma^2} + 0.11116\frac{\Omega_L^3}{\Gamma^3}. \quad (1.20)$$

As Ω_G is associated with the instrument width it is expected to be constant [5].

CHAPTER 1 THEORY

Hendricks-Teller state

Hendricks-Teller peaks are a result of mixed intercalation states, and typically appear in the transition between two states. They were mathematically explained by S. Hendricks and E. Teller in [44] in 1942, thereby the name. When several kinds of layers are present, the phase shifts result in intensity fluctuations which are manifested as an extra peak representing the average form factor. The position of the distribution associated with this mixed state depends on the fraction of particles that are in the different intercalation states.

1.5 X-ray sources

X-rays were discovered by W.C. Röntgen in 1895, and is one of the most common probes for studying the structure of matter. Since their discovery the sources and methods of generating X-rays for structural investigation have come a long way. In 1912 Coolidge developed the X-ray tube, but the biggest breakthrough was making use of synchrotron radiation as a high intensity source.

1.5.1 Electron impact source

In stationary sources, electrons are excited from a cathode filament and accelerated towards an anode target resulting in generation of X-rays. The limiting factor in terms of intensity is the maximum power the metal anode can withstand. By rotating the anode, the maximum power can be increased. The spectrum from an X-ray tube has discrete fluorescent lines superimposed on the continuous *Bremsstrahlung* radiation spectrum (see Figure 1.6). These lines correspond to the transitions between discrete atomic energy levels in the anode material [42]. The wavelength can be chosen to one of the discrete energies by letting the beam pass through an optical system.

1.5.2 Synchrotrons

In the 1970s one started to make use of synchrotron radiation as an X-ray source. This radiation was emitted from charged particles circulating at constant energy in storage rings at high energy nuclear physics experiment facilities. This kind of source was much more versatile and intense than any of the previously used stationary sources [42]

Synchrotron radiation

When an electron (or positron) is accelerated it emits radiation. In synchrotrons one exploits that a charged particle moving with velocity \mathbf{v} will

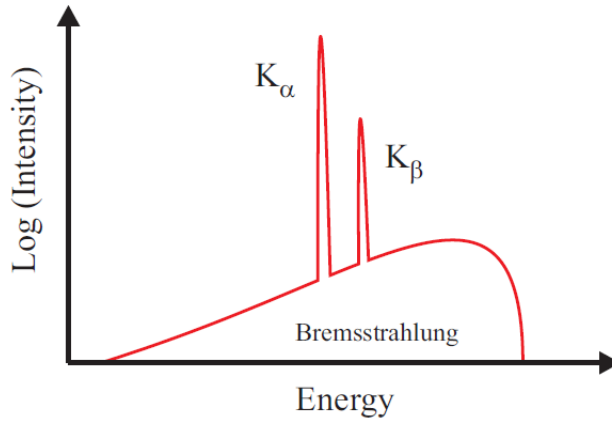


FIGURE 1.6: Characteristic X-ray radiation spectrum from a stationary source. Discrete peaks are due to transitions between atomic energy levels in the anode material. Adapted from [42].

be accelerated by an electromagnetic field. The classical equation of motion, in terms of the momentum \mathbf{p} , in an electric, \mathbf{E} , and magnetic, \mathbf{B} , field is given by the Lorentz formula

$$\left| \frac{d\mathbf{p}}{dt} \right| = e(\mathbf{E} + \mathbf{v} \times \mathbf{B}) \quad (1.21)$$

However, in synchrotrons, the charged particles are strongly relativistic. By replacing the classical momentum with the relativistic invariant quantity $d\mathbf{P}/d\tau$

$$\left| \frac{d\mathbf{P}}{d\tau} \right|^2 = \left| \frac{d\mathbf{p}}{d\tau} \right|^2 + \frac{1}{c^2} \left(\frac{dE}{d\tau} \right)^2 \quad (1.22)$$

the power, S , radiated by an electron is given by the Larmor formula. Since $v \approx c$, it can be expressed by

$$S = \frac{e^2 c}{6\pi\epsilon_0} \frac{1}{(m_e c^2)^4} \frac{E^4}{R}, \quad (1.23)$$

where R is the radius of the storage ring. Since the acceleration is perpendicular to the direction of movement, the charged particles will move in a circular path. Also, because the velocity of the particles in the storage ring is so high, the radiation is emitted mostly in the direction of movement, taking on the shape of a narrow cone with opening angle $1/\gamma$.

In storage rings it is thus possible to generate very sharp cones of radiation, with high intensity. This is described with the concept of brilliance, which is given as the number of emitted photons per second in a narrow energy bandwidth, per unit solid angle. The synchrotron radiation gives a continuous wavelength spectrum. The wavelength can be tuned in the beamlines to correspond to energies ranging from infrared to hard X-rays, and is therefore attractive for many scientific fields [29].

Storage rings and insertion devices

A storage ring synchrotron radiation source is an arrangement of components that enables a current of charged particles to circulate a closed orbit at high speed for periods of several hours, while synchrotron radiation is emitted. Some radiation comes from the bending magnets, but most comes from specially designed *wiggler* and *undulator* devices. The radiation leaves the ring through tangential ports, *beamlines*, which allows the radiation to pass to experimental stations placed around the storage ring [45]. General schematics of a synchrotron are displayed in Figure 1.7.

The stored beam circulates in a vacuum chamber at velocities close to the velocity of light. The storage ring is filled with particles from an injector, i.e. a linear accelerator. Over time, the intensity of the stored beam will decrease, and must be refilled with particles.

In a synchrotron different magnet arrangements are used to control the circulation of the charged particles and to maintain small transversal dimensions of the beam.

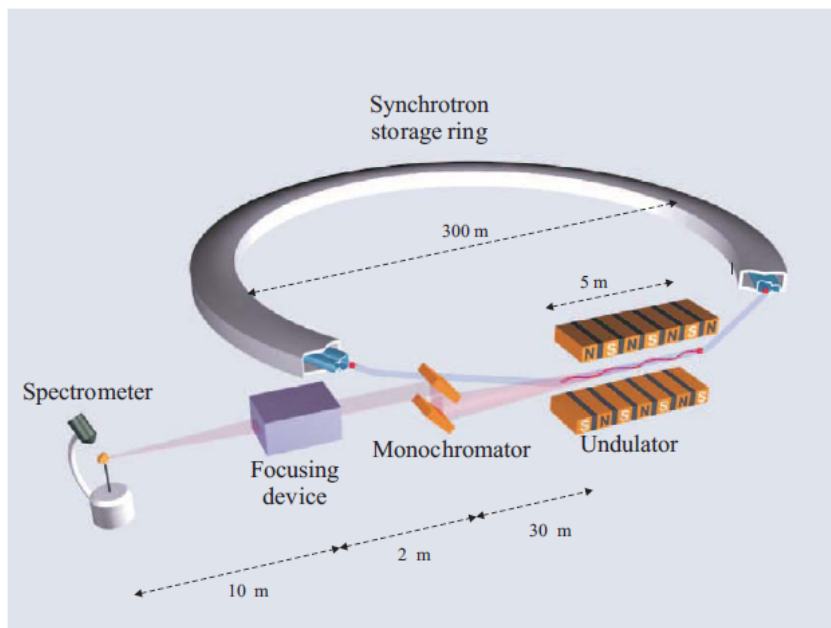


FIGURE 1.7: Schematic figure of a typical X-ray beamline at a third generation synchrotron X-ray source. Bunches of charged particles (electrons and positrons) circulate the ring. The ring is designed with straight sections where an insertion device, such as an undulator, is placed. The lattice of magnets in an insertion device forces the particles to oscillate and they produce intense beams of radiation. This radiation passes through a number of optical devices, such as a monochromator and a collimator, to obtain a beam with the desired properties on the sample. Adapted from [42].

1.6 Infrared spectroscopy

Infrared spectroscopy can provide information on other features of clays, such as characteristic chemical bonds and molecular energies. This section gives a brief introduction to the principles of this technology.

Molecular vibrational modes

Due to thermal energy atoms are in constant motion, which in molecules is seen as variations in lengths of atomic bonds, vibrations. Transitions between quantized vibrational energy states of molecules result in transition energies within the infrared spectrum. The vibrations can range from the simple coupled motion of the two atoms in a diatomic molecule to the complex motion of each atom in a large molecule. Molecules of N atoms have $3N$ degrees of freedom, out of which three represent translational motion in mutually perpendicular directions. Three represent rotations about these axes respectively. The remaining $3N-6$ degrees of freedom give the number of ways in which the atoms in a nonlinear molecule can vibrate. For linear molecules, such as CO_2 , rotation about the axis of the bond does not involve displacement of the atoms. Thus, one of the rotational degrees of freedom is lost and the molecule has an additional vibrational degree of freedom [46].

In modes of simple harmonic motion which follow Hooke's law, all atoms vibrate with the characteristic frequency ν_i in the potential energy states V_{iv} , given by

$$V_{iv} = h\nu_i \left(v_i + \frac{1}{2} \right), \quad (1.24)$$

where v_i is the vibrational quantum number. Transitions with $\Delta v_i \pm 1$ are allowed if they result in a change in the dipole moment μ . Some vibrational modes may be degenerate and others forbidden with respect to the dipole moment, so in practice the number of vibrational modes is lower than the theoretical.

CHAPTER 1 THEORY

The harmonic description is valid only for small values of v_i . More generally the vibrational motion can be described by a Morse-type potential function. The first order approximation of this potential is valid also for 'large' v_i and includes a mode-dependent anisotropy constant, χ_i , which typically takes on values between -0.001 and -0.02 [46]:

$$V_{iv} = h\nu_i \left(v_i + \frac{1}{2} \right) + h\nu_i \chi_i \left(v_i + \frac{1}{2} \right)^2. \quad (1.25)$$

The anharmonicity relaxes the selection rule, and bands caused by $\Delta v_i > 1$ become allowed. Thus, in the mid-infrared spectrum of organic compounds one can observe overtone ($\Delta v_i = 2, 3, \dots$) and combination ($\Delta v_i = 1$; $\Delta v_j = 1$, where j represents a different mode) bands, which commonly appear weakly along with the bands due to fundamental transitions ($\Delta v_i = 1$).

Every molecule has a unique set of vibrational modes, which means that its infrared spectrum can be used for identification. In many modes only a few atoms have large displacements while the rest of the molecule is almost stationary. The frequency of such modes is characteristic of the specific functional group in which the motion is centered, and is to a small extent affected by the nature of the other atoms. Consequently, observation of activity in a certain region of the spectrum often indicates presence of a specific chemical functional group in the molecule.

Other bands involve significant motion from only a few atoms, yet their frequencies varies from one molecule containing the functional group to another. Such modes are useful to distinguish molecules containing the same functional groups, and are known as *fingerprnt bands*. *Skeletal modes* are due to significant displacement of many atoms, and can be used to distinguish structurally similar compounds. These modes usually have low vibrational frequencies and are thus often found in the far-infrared region. They also yield useful information on heavy atoms and hydrogen bonds within the molecule [46].

Vibration-rotation spectroscopy

Samples in all phases of matter can be studied with infrared spectrometry, although spectra of gases, liquids and solids have different characteristics. Spectra of small molecules in the vapor phase show considerable fine structure because transitions between quantized rotational energy levels occur at the same time as vibrational transitions. Similar features are rarely observed for larger molecules in the vapor phase (because the individual rotational transitions are too close together to be resolved) or liquids (because the collision rate by far exceeds the rotational frequency).

Diatomic molecules have the simplest vibration-rotation spectra. The rotational energy levels of such molecules are characterized by a single *rotational quantum number*, J . If the molecule is assumed to be a rigid rotor with constant bond length the rotational energy is

$$E_J = BJ(J + 1), \quad (1.26)$$

where B is the *rotational constant*, given by

$$B = \frac{h}{8\pi^2 I c}. \quad (1.27)$$

Here, I is the moment of inertia of the molecule and c the velocity of light. The selection rule for transitions between rotational energy states for linear molecules is $\Delta J = \pm 1$, which corresponds to energy changes of

$$E_J - E_{J-1} = BJ(J + 1) - BJ(J - 1) = 2BJ. \quad (1.28)$$

For a perfectly rigid rotor the pure rotation spectrum would be a series of lines with equal spacing of $2B \text{ cm}^{-1}$. For most molecules B is sufficiently small so that the pure rotation spectrum is found in the microwave region of the spectrum; however, for light molecules such as H_2O and CO_2 , these transitions absorb in the far infrared.

Diatomic molecules have a single fundamental vibrational mode, of wave-number $\tilde{\nu}_0$, which is infrared active only if the molecule consists of two

CHAPTER 1 THEORY

different atoms. For any allowed vibrational transition of a gaseous diatomic molecule, a simultaneous rotational transition must occur; that is

$$\Delta v = \pm 1 \text{ and } \Delta J = \pm 1. \quad (1.29)$$

Thus, the vibration-rotation spectrum of a rigid diatomic molecule consists of a series of equally spaced lines, or *rotational fine structure*, above and below $\tilde{\nu}_0$ which correspond to $\Delta J = +1$ and $\Delta J = -1$, respectively. These lines are often referred to as the P- and R branch. There is no absorption line at $\tilde{\nu}_0$ (Q branch) because $\Delta J \neq 0$, which corresponds to no change in the dipole moment.

As molecules are not actual rigid rotors, but display an increase of molecular bond lengths with angular velocity (due to centrifugal forces), the simple model does not hold in practice. The effect of centrifugal distortion is to decrease the rotational constant B at high J . This is, to a first approximation, taken care of by introducing a *centrifugal distortion constant*, D , which is typically 3-5 orders of magnitude smaller than B . Because of the centrifugal distortion, the spacing of the lines decreases with increasing frequency. This corresponds to lines in the P-branch being further apart for lower lower wavenumbers. Correspondingly, the spacing of lines in the R-branch decreases as the frequency increases.

Larger and less symmetrical molecules display vibration-rotation spectra with smaller spacing of the lines. Different selection rules apply for all modes, depending on the symmetry of the vibration involved. Linear molecules have two equal principal moments of inertia, while nonlinear molecules usually have three. These spectra can become very complex [46].

CO₂ spectrum

CO₂ is a linear molecule with two stretching modes, in which the molecule stays linear throughout the vibration, and a bending mode. The symmetric stretching mode does not involve change in the dipole moment and is thus not infrared active. However, the antisymmetric stretching mode does involve a change. For this mode the selection rules are the same as for diatomic molecules, and the spectrum has a similar appearance. It has frequency 2349 cm⁻¹. The bending mode of CO₂ is degenerate and permits a vibrational transition without a simultaneous change in the rotational quantum number. This causes a strong line in the spectrum corresponding to $\Delta J=0$, as can be observed in Figure 1.8(b). The bending mode of CO₂ is found at 667 cm⁻¹.

H₂O spectrum

As H₂O is a nonlinear molecule, it has three principal moments of inertia and consequently a very complex vibration-rotation spectrum. Its bending mode is displayed in Figure 1.9.

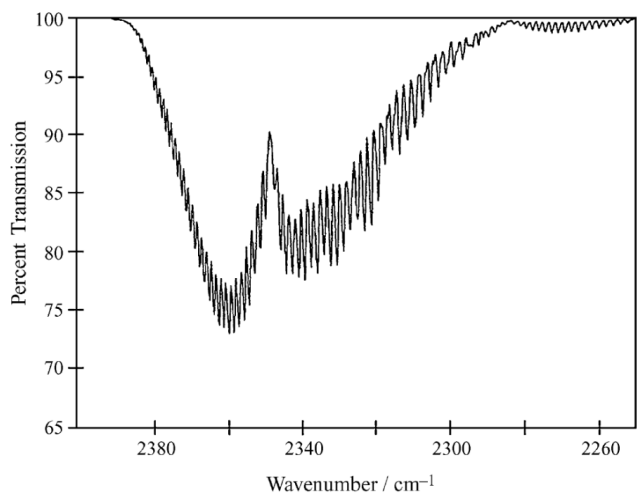
1.7 Fourier Transform Infrared Spectroscopy

In infrared spectroscopy infrared radiation is passed through a sample, where some of it is absorbed by the sample and some is transmitted. The resulting spectrum represents the molecular absorption and is a molecular fingerprint of the sample.

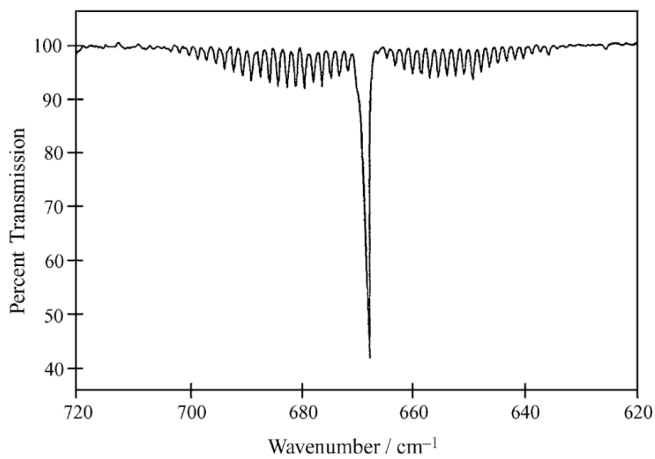
Traditional IR spectroscopy made use of prisms or gratings to separate the individual frequencies of energy transmitted from the infrared source. The detector measured the amount of energy at each frequency which had passed through the sample, providing an intensity versus frequency spectrum.

Fourier transform infrared spectroscopy (FTIR) has several advantages over the traditional dispersive methods of infrared spectral analysis. It

CHAPTER 1 THEORY



(a)



(b)

FIGURE 1.8: Infrared active vibration-rotation fundamental bands of CO₂. (a) Antisymmetric stretching mode, 2349 cm⁻¹, and (b) Bending mode, 667 cm⁻¹. Adapted from [46].

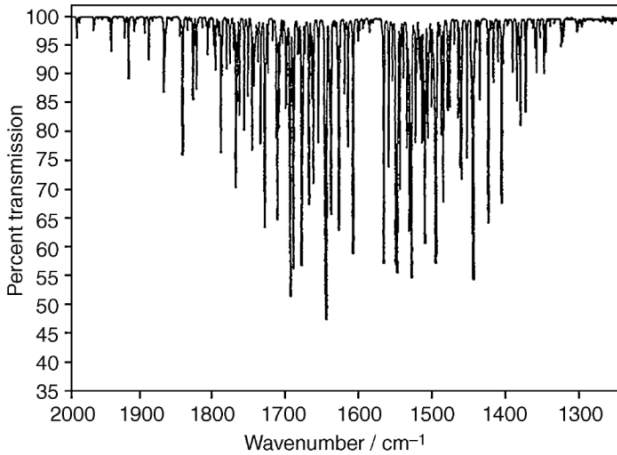


FIGURE 1.9: Infrared spectrum of bending mode of H_2O . Adapted from [46].

has increased sensitivity and speed, greater optical throughput and provides precise measurements without need of external calibration. The instrument is also mechanically simple; with only one moving part. FTIR provides a method of measuring all frequencies simultaneously. This is possible by use of an interferometer. It produces a signal with all the frequencies of interest encoded into it.

In the interferometer the incoming beam is divided into two optical beams by a beam splitter. One beam is reflected off a flat stationary mirror, while the other is reflected off a mirror which can be moved a small distance away from the beam splitter. The two beams reflect off their respective mirrors and are recombined back at the beam splitter.

The movable mirror is constantly shifting its position, thus continuously changing the difference in path length traveled by the two beams. The signal leaving the interferometer, the interferogram, is the result of the beams interfering with each other. This signal holds a unique property; every data point which makes up the signal (a function of the moving mirror position) holds information on every infrared frequency coming from the source [47]. Thus, when the interferogram is measured, all frequencies can be measured simultaneously, which in turn means fast scans.

CHAPTER 1 THEORY

To decode the individual frequencies of a measured interferogram the Fourier transformation is performed by the computer, and spectral information of the sample is obtained. A simple layout of a FTIR spectrometer is presented in Figure 1.10. The instrument employ a HeNe laser as an internal wavelength standard and is thus self-calibrating.

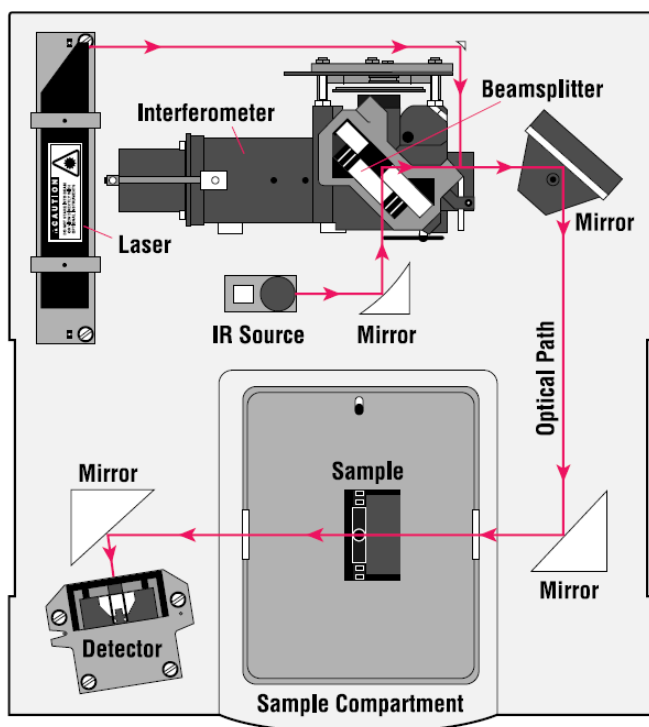


FIGURE 1.10: Schematics of a Fourier Transform interferometer. The incoming beam from the IR source passes through an interferometer. It is split and reflected by stationary and movable mirrors, resulting in a net beam encoded by the interference of the reflected beams. The beam is transmitted through the sample, where some radiation is absorbed due to corresponding molecular vibrational energies of the sample. The detected beam is decoded by applying the Fourier transformation. The laser ensures self-calibration. Adapted from [47].

Chapter 2

CO₂ Intercalation Experiment

All experiments for this thesis was performed at the laboratory of the Complex group at NTNU. This chapter describes the setup and methods used in experiments with both X-ray diffraction and IR spectroscopy.

2.1 Experimental setup X-ray diffraction

2.1.1 Nanostar Bruker system

Technical specifications Nanostar Bruker System	
Wavelength	1.5418 Å
Source	Stationary, Cu-K _α
Monochromator	Curved multilayer mirror
Collimation	3 pinholes
Spot size on sample	0.4×0.4 mm ²
Experimental techniques	SAXS, WAXS
Detector	Multiwire grid, Xe-gas
Resolution	1024×1024 pixels

TABLE 2.1: Technical data for the Nanostar Bruker system.

CHAPTER 2 CO₂ INTERCALATION EXPERIMENT

The setup at NTNU makes use of a stationary source. Technical data for the setup are given in Table 2.1. Measurements were performed using a Bruker NanoSTAR X-ray scattering instrument. A Xenox electron impact source with copper anode is used, selecting the Cu-K_α peak with $\lambda = 1.5418$ nm. Monochromation is done by use of a multilayer mirror, which ensures that only Cu-K_α is selected, and monochromatic X-rays come out. Collimation is done by three pinholes, and ensures a 0.16 mm² beam on the sample. The deviation of λ and the divergence of the incoming beam, together with the finite sample length, determine the instrumental resolution function. Detection is done with a Xe-gas multiwire grid detector, with a pixel resolution of 1024×1024.

The detector was placed at a distance from the sample holder corresponding to wide-angle X-ray scattering (WAXS) detection, yielding an available range of momentum transfer q on the detector of $(2.5 < q < 7.5)$ nm⁻¹.

2.1.2 Sample holder

For the experimental setup a custom built sample cell was used. It was designed to ensure that a sufficient amount of sample stays within the scattering volume, while also limiting the thickness of the sample and thereby limiting the loss of signal. The cell is an improved version of the one used by Hemmen and Rolseth [24, 29].

The cell, which is displayed in Figure 2.1, has three main parts: a hollow base; a ring, which is screwed inside the base; and a bolt shaped cover. The cover and base are held together using screws. On the outside there are two valves for letting gas in and out of the sample volume.

The base has a diameter 6 mm opening covered with a Kapton film. This is the exit window for the scattered radiation, and is held in place by the ring. The inner diameter of the ring is the same as that of the window, to ensure that the sample stays within the volume from which scattering can be detected. The bolt shaped cover serves several functions. It has a diameter 1 mm window, covered with Kapton, through which the X-rays can enter the cell. Along the sides of the bolt thin channels lead gas into the sample volume. The bolt has the same outer dimensions as the inner

2.1 EXPERIMENTAL SETUP X-RAY DIFFRACTION

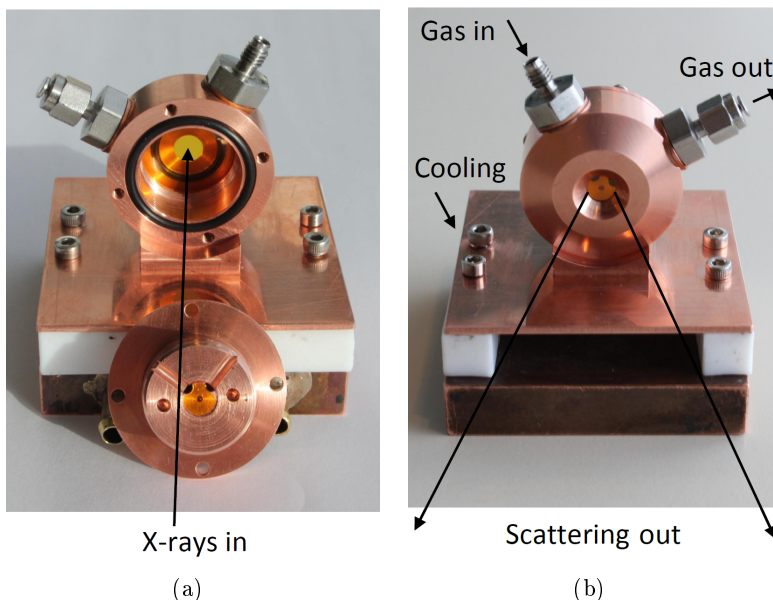


FIGURE 2.1: Image of test cell. (a) Back side, demonstrating how the bolt shaped cover and ring fit together. (b) Front window through which the scattered X-rays leave the cell. During experiments gas can enter and leave the cell through the valves.

dimensions of the base (with the ring in place). The parts are attached by screws, with a rubber O-ring in between, to keep the cell airtight.

Cooling, isolation and pressure control

In order to cool the cell to the desired temperature a combination of a Peltier element and heat sink was used. The heat sink consists of two stacked copper blocks, with internal channels through which fluid can flow, which were connected to a circulator filled with anti-freeze.

The Peltier element makes use of the thermoelectric effect to generate a temperature difference, when a voltage is applied to it. The Peltier element merely provides a temperature difference between the two sides, thus, the

CHAPTER 2 CO₂ INTERCALATION EXPERIMENT

heat sink must hold a sufficiently low temperature to get the test cell even colder. To avoid thermal exchange with the surroundings the test cell and heat sink were wrapped in isolating tape. The sample cell and heat sink were separated by Teflon to prevent them from exchanging heat directly. The tubes connecting the heat sink and circulator were also isolated from the surrounding air. The setup is showed in Figure 2.2.

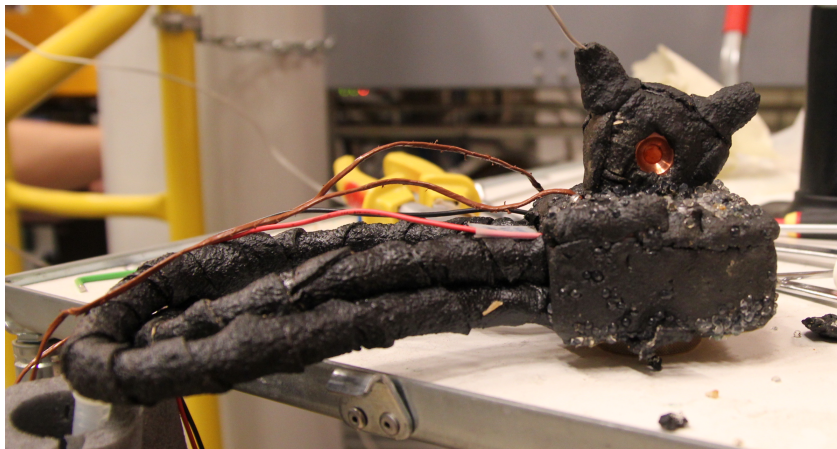


FIGURE 2.2: The sample cell covered by isolating tape. During intercalation experiments one valve was tightly closed while the other was connected to the gas supply.

A thermocouple could be placed inside a small hole on the sample cell, close to the sample, to provide information on the temperature. The pressure was controlled manually by standard reduction valves and the output was limited by the flask pressure and range of the reduction valves.

2.1.3 X-ray setup NTNU

The experimental setup consisted of the sample cell aligned with the incoming X-ray beam, and the other components described above. It is displayed in Figure 2.3. As the circulator could go to very low temperatures, removing excess heat generated by the Peltier element went smoothly and a stable temperature could be obtained (within the temperature range $-30 < T < 45$).

2.1 EXPERIMENTAL SETUP X-RAY DIFFRACTION

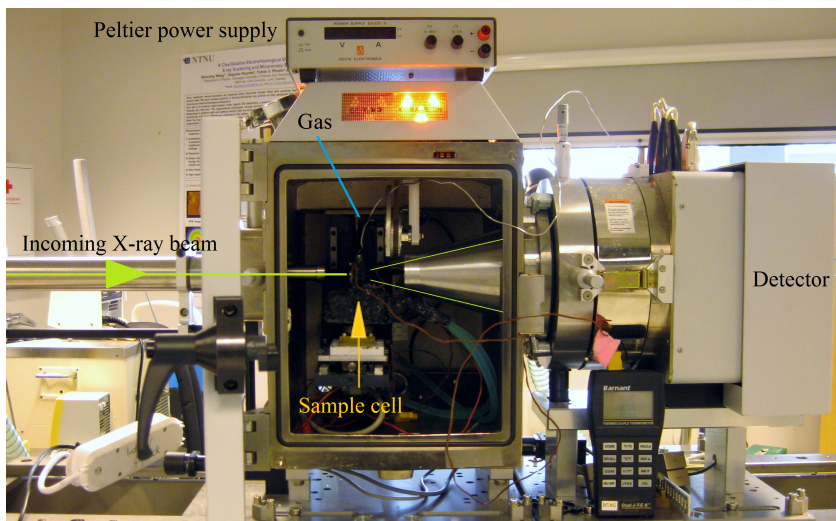


FIGURE 2.3: The cell mounted inside the hutch at NTNU. During the experiments the gas was connected, and the cell was wrapped in isolating tape to minimize heat exchange with the environment. Since it is black, its position is indicated. Other important components are also labeled.

A stationary source has significantly lower beam intensity than a synchrotron radiation source. To obtain a satisfactory signal-to-noise ratio and limit the signal loss due to absorption in the sample volume, experiments were mainly not performed beyond the condensation point of CO_2 .

When the sample cell gets very cold, there are problems related to air humidity condensing and freezing on the outside of the sample cell. If the Kapton windows get covered by ice the transmitted intensity gets significantly reduced. To reduce humidity a container filled with silica gel was placed inside the hutch.

2.2 Experimental method

2.2.1 Experiment at NTNU

Samples and preparation

The LiFh clay used in experiments was purchased from Corning Inc, and the natural clay sample from Source Clay Repository. The clay powder samples were grinded in order to break up aggregates and heated to 170 °C for more than 5 hours in order to dehydrate them.

LiFh films were prepared by dissolving ~ 1 g of LiFh in 200 mL distilled water and stirred for 1 hour at 40 °C . The dispersion was centrifuged for 10minutes at 1500rpm. Approximately 30 mL of the suspension was dried in a beaker on a plate heated to 80 °C .

The CO₂ used for the experiments had a purity of 99.999% (Yara Praxair, grade 5.0). The N₂ used was Yara Praxair Nitrogen 6.0 Ultra Plus.

Intercalation

The sample cell was loaded with a small amount of clay (~ 10-15 mg), and the cover was tightened very quickly to avoid intercalation of humidity in the surrounding air. Flushing with N₂ was started shortly after loading to reduce residual humidity and prevent any other air from entering the sample cell, and a scan was recorded to ensure that the sample was dehydrated.

Subsequently, the sample cell was cooled to the target temperature before the gas was changed to CO₂. The gas outlet of the cell was closed and the pressure increased. The pressure was left on for several hours, while the temperature was kept stable (± 1 °C).

2.2 EXPERIMENTAL METHOD

Heating and deintercalation

After a LiFh sample had been exposed to CO₂ for sufficiently long time and reached a stable maximum intercalation, the sample was heated to investigate at what temperature CO₂ leaves the clay. Water is known to deintercalate fluorohectorite when the sample is heated, and it is of interest to investigate if CO₂ also exhibits this behavior. The pressure of CO₂ was released and flushing with N₂ resumed while heating the cell to the target temperature. Experiments with heating the cell either in steps or directly to high temperature were conducted. For comparison, similar experiments were performed on both humid and dry clay samples, after exposure to high pressure N₂ or CO₂, respectively.

Data acquisition

WAXS diffractograms were recorded for dry and humid hectorite samples. The q-range of interest was approximately 2.5-7.5 nm⁻¹. The acquisition time ranged from 1500 to 3600 seconds, depending on the background noise and the X-ray absorption of the sample.

In order to study the time evolution of the intensity versus scattering vector scans were taken continuously during intercalation and deintercalation. The cell was kept in the same position while recording the scattered intensity. The resulting scans provide *in situ* information on changes in the clay interlayer spacing.

2.2.2 Infrared Spectroscopy

Initial measurements were done to investigate the transmission through the LiFh films. FTIR apparatus was attempted wrapped in a glove bag because it is of interest to do the FTIR measurements in a controlled dry N₂ atmosphere, both to keep the samples dry and avoid signal loss due to background absorption. As the films were very thin, water from the surrounding air would intercalate almost immediately in normal humid air. However, it proved challenging to obtain a pure nitrogen atmosphere. The machine was too large to wrap in a glove bag (to be completely surrounded by N₂ atmosphere) and it was difficult to completely close off the sample volume. Therefore, simply an overpressure by N₂ in the sample chamber was used. The optics of the machine was flushed with N₂ gas to reduce absorption by the background.

The IR-measurements were performed on a Spectrum RX I FTIR spectrometer from Perkin Elmer, in transmission mode. Scans were taken on the wavenumber interval 400-4000 cm⁻¹. Measurements were done in *ratio mode*, where the detected signal for each frequency is given as a ratio of transmitted intensity relative to that of a background scan.

The films provide a very small scattering contribution when studied with X-ray diffraction. This is mainly due to the orientation of the layers, which are primarily oriented orthogonal to the incoming X-ray beam. This orientation yields no reflections on the detector. Furthermore, as the films are very thin they scatter very little radiation. Consequently, extra care had to be taken upon loading the cell to ensure that the sample remained dry, as this could not be verified by X-ray diffraction.

The film was exposed to CO₂ at temperature and pressure conditions known to invoke intercalation, namely -30 °C and 20 bar. The film was left to intercalate for several hours, until the majority of the interlayers was expected to be occupied by CO₂. The sample cell was moved to the glove bag with N₂, to prevent unnecessary contact with humidity. The film was moved to the IR spectrometer in dry N₂ atmosphere.

Chapter 3

Data analysis and discussion

This chapter describes the method used to extract data from X-ray diffractograms. Further, we discuss observations made regarding intercalation and retainment of CO₂ in LiFh clay. An overview of the experiment using IR spectroscopy is also given, along with a discussion of what we expected to observe.

3.1 Data acquisition and processing

In order to make the data from X-ray diffraction experiments easier to analyze, it is convenient to extract intensity profiles rather than studying two dimensional scattering patterns. There are several steps involved in the procedure of transforming the frames recorded by the detector during the separate scans into one dimensional plots of intensity versus scattering vector and other figures which can be used for analysis.

Software

The native SAXS Bruker software of the setup was used for data collection, and the information registered by the detector was stored as Bruker .gfrm files. The files also contain a header with scan parameters, such as

CHAPTER 3 DATA ANALYSIS AND DISCUSSION

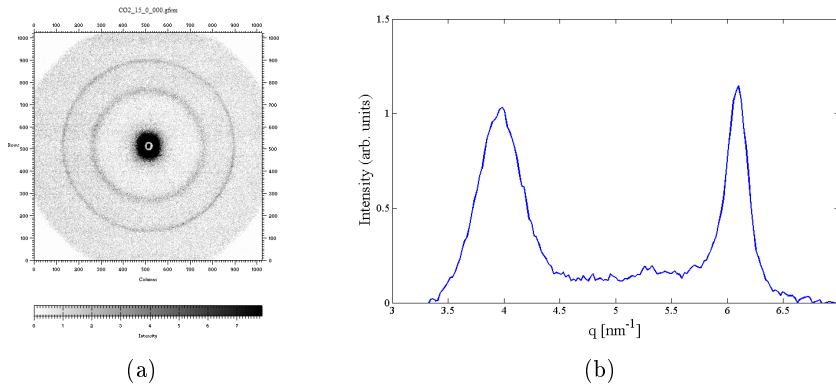


FIGURE 3.1: (a) Typical 2D diffraction pattern recorded by the detector (b) Integrated 1D representation of the same diffraction pattern. The intensity is given as function of the scattering vector q .

time of scan, spatial coordinates and exposure time. The Fit2D software, developed at ESRF by Dr. Andy Hammersley [48], was used both for calibration with AgBh and integration of the Bruker files.

A MATLAB script written by PhD student Henrik Hemmen was used to generate macros for Fit2d. MATLAB was also used for all further analysis and plotting.

Calibration

In order to find the right position of the beam center and sample-to-detector distance, a calibration was performed. The calibration sample was a silver behenate (AgBh) powder, which has well known and clearly defined Bragg peaks. By comparing the diffraction peaks, or rather circles, to tabulated values for silver behenate, the correct beam center and sample-to-detector distance was found. Finding the right values for these parameters is crucial for the data integration, as they are directly related to the Bragg scattering angle θ .

3.1 DATA ACQUISITION AND PROCESSING

Background subtraction

A background subtraction was performed in order to distinguish the intensity due to scattering by the sample, from the background noise. A simple approach is to seek out regions in the plot where the intensity should be more or less unaffected by scattering by the sample. The background can typically be expressed as a power law or a linear relation. A suitable function is fitted to the intensity distribution, on intervals which receive a satisfactory small scattering contribution from the sample.

In the regions between peaks, the peaks on both sides contribute to the intensity. Thus, this range of momentum transfer q was not used for the background fitting. Only the approximately linear sections for q -values smaller and larger than those corresponding to the peaks produced by the kapton window and dehydrated clay, respectively, were used. One should also avoid the regions around the beam center and detector edges. Since only two sections were used to fit the background in this experiment, a linear profile was chosen.

After finding a good fit for the background, based on the chosen q -range, the background was subtracted from the intensity. An example of how this was done is displayed in Figure 3.2.

Profile extraction and peak position determination

A MATLAB script running macros in Fit2d was used to integrate the frames azimuthally, to obtain 1D profiles of the intensity versus scattering vector. Figure 3.1 shows an example of a two dimensional scattering pattern and the corresponding intensity profile.

Due to the instrument width and the fact that the scattering peaks are not perfectly distributed, each peak was fitted to a Pseudo-Voigt profile, given by equation (1.18). The fitting was automated by using data points in the regions where the respective scattering peaks were expected to appear as basis for the fits. From the fits we obtained peak intensity maxima I_{max} and corresponding q , as well as the width Δq .

The intensity profiles of each scan have been normalized by the Kapton

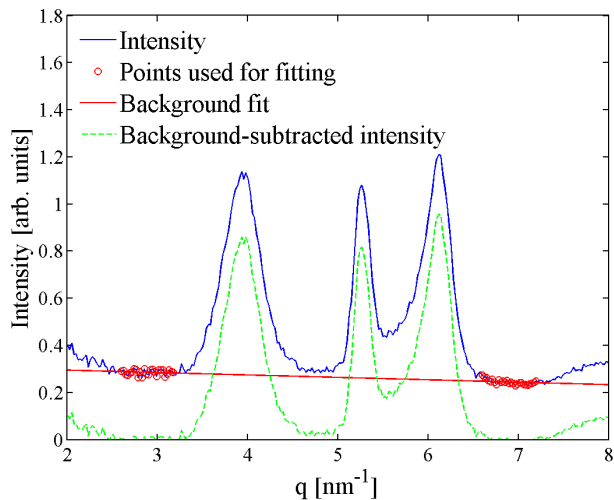


FIGURE 3.2: Subtraction of background from intensity. A background is fitted to the regions in q -range that are not affected by scattering from the sample, and subtracted from the intensity. The left peak is produced by the Kapton window, while the middle one and the one to the right are produced by CO_2 -intercalated and dehydrated LiFh clay, respectively.

peak intensity. A Pseudo-Voigt profile was fitted to the Kapton peak and the resulting maximum was used for normalization.

3.2 Discussion of X-ray data

3.2.1 Intercalation

One of the goals of the experiments has been to get a better understanding of which parameters influence the intercalation process. Attempts have been made to map the dependence of the intercalation rate on temperature and pressure, during exposure to CO₂.

In situ measurements were performed until the 0 WL peak was negligible at temperature -20 °C; for pressures 20 bar, 11.5 bar and 10 bar. One partial intercalation was also observed at -20 °C and CO₂ at 5 bar. In terms of temperature variation, samples were exposed to 20 bar CO₂ at -15 °C, -10 °C and +5 °C, in addition to the series at -20 °C.

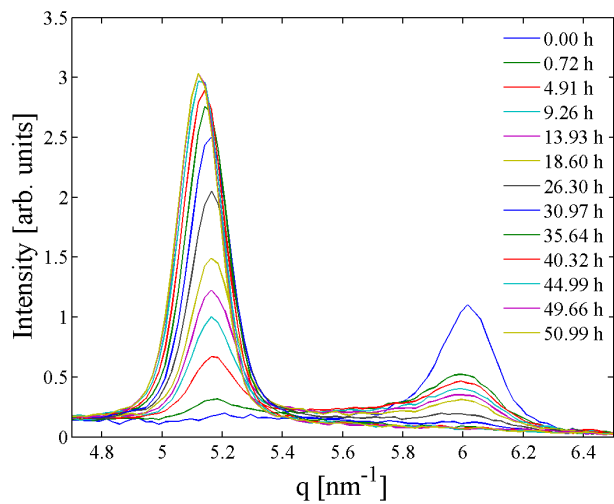
During experiments attention was primarily paid to the one dimensional intensity distributions (Figure 3.3(a)), and, in most cases, exposure to CO₂ ended when the 0 WL peak was considered negligible.

Some samples were exposed to CO₂ even after this point. The intensity curves show that the peak intensity increases some more, before stabilizing at a level which appears to be the maximal intensity of the one-CO₂-layer intercalation state. One experiment also indicated a consecutive two-CO₂-layer state, but there was not enough time to investigate this further.

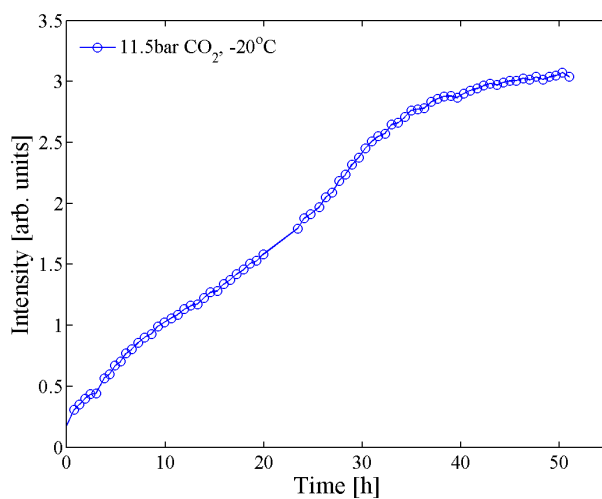
Figure 3.3(b) shows the peak intensity as function of time for a sample exposed to CO₂ until the peak intensity of intercalated CO₂ started to converge towards a stable level of *maximal intercalation*. The sample was kept at a low temperature, -20 °C, and intermediate pressure of 11.5 bar during exposure to CO₂.

In the initial phase of exposure, the intercalation peak intensity appears to be almost linear with time. In some cases the slope appears to change after some time. The process seems to accelerate before stabilizing at a higher rate of intercalation. At this higher rate, the curve is still more or less linear.

The reason for these irregularities is unknown. They could possibly reflect the dynamics of intercalation under the given conditions; e.g. if the



(a)



(b)

FIGURE 3.3: (a) Intensity distributions at different times during exposure. The peak to the right is produced by dehydrated LiFh, while the peak to the left is due to scattering by clay intercalated with CO_2 . (b) CO_2 intercalation peak intensity as function of time. Exposure to gaseous CO_2 at -20°C and 11.5 bar.

3.2 DISCUSSION OF X-RAY DATA

interlayer CO_2 molecules are organized in a fashion which allows faster absorption of CO_2 beyond a certain filling level. Another option is that the change in intercalation rate can be credited to variations in pressure or temperature. As experiments were run both night and day it was not possible to constantly monitor the conditions. Changes in the room temperature could have influenced the temperature of the test cell.

As the intensity approaches what appears to be the maximum intercalation, the process slows down. It makes sense that the the peak intensity increases less when most of the clay interlayer gaps become filled with CO_2 . As there are fewer sites for the molecules to occupy, it is natural that the number of additional interlayer gaps which are expanded by CO_2 molecules, per unit time, decreases.

When all interlayer gaps are occupied by CO_2 the peak intensity is not expected to increase further. Still, reorganization of the molecules within the interlayer gaps could potentially make room for more CO_2 , and allow absorption of more gas. Also, reorganization could change the structure factor, resulting in e.g. a narrower peak with higher intensity.

As the intensity curves seem to have a linear nature in the early phases of intercalation, one would perhaps expect that the slope could be used to quantify the kinetics of the process, for a given pressure-temperature (PT) condition. However, this proves to be somewhat problematic. Even though the amount of clay sample used in the experiments was comparable, differences in terms of absorption by ice on the sample holder, variations in detector vacuum (yielding more background scattering), and absorption of CO_2 under different conditions (there is more CO_2 in the scattering volume at higher pressures), can affect the measured intensities and thus the calculated slopes of intercalation.

A more convenient measure for comparing intercalation rates could be determining a time constant for when the maximum intensity is reached, or a certain percentage of it. Another option could be to compare the times for the CO_2 peak intensity to exceed that of 0 WL.

Width and position of CO₂ intercalation peak

The width, position and basal spacing of the peak produced by intercalated CO₂ could possibly provide complementary information on the dynamics of intercalation. Figure 3.4 shows an example of the peak width Δq , the peak position q and corresponding basal spacing d_{001} as functions of time.

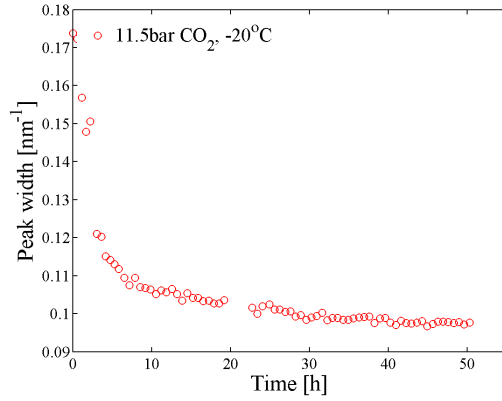
The scattered intensity distributions in Figure 3.3(a) demonstrates that before exposure to CO₂, the sample contributes to a very small extent to scattering into the range used for fitting ($\sim 4.9 < q < 5.4$). Also, in the early phases of exposure the contribution to the scattered intensity in this range is small, and the scattering does not correspond to one well-defined intercalation state, but a range of basal spacings close to d_{001} typical for CO₂-intercalated LiFh.

This is reflected by the width Δq of the fitted peak, which is displayed in Figure 3.4(a). The peak is wide in the early phase of exposure to CO₂ and becomes narrower as the intercalation peak becomes more pronounced and well-defined. When, according to the intensity curve, the intercalation is near a stable maximum, Δq approaches a constant value.

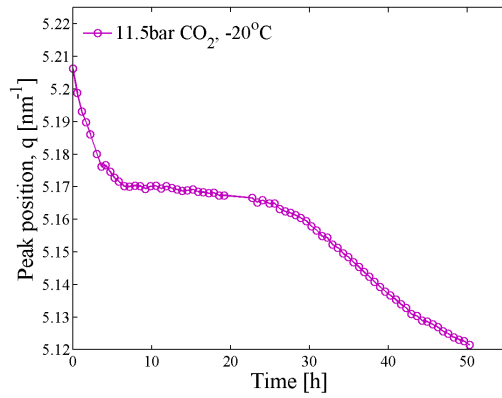
This behavior is expected, as a significant uncertainty is associated with the fit parameters of the intercalation peak in the first few measurements. At this point, a very small fraction of the crystallites are in an intercalated state, and they contribute very little to scattering into the q -range used for fitting. As the background scattering is not perfectly subtracted from the measured signal, it will always, to some extent, contribute to the intensity distribution. When the signal from the sample is small, the effect of the background influences more, and imposes larger uncertainty on the Pseudo-Voigt fit. However, as the scattering by the intercalation peak becomes dominating, the influence of the background is reduced, and the Pseudo-Voigt fit is based primarily on scattering by the sample.

The error bars of the basal spacing (Figure 3.4(c)) reflect this. They correspond to 95% confidence intervals, calculated from goodness-of-fit parameters for the Pseudo-Voigt profile. In the early phase, the Pseudo-Voigt fit corresponds to a wide peak of small amplitude. The fitted position is somewhat arbitrary within the indicated interval and has a large uncer-

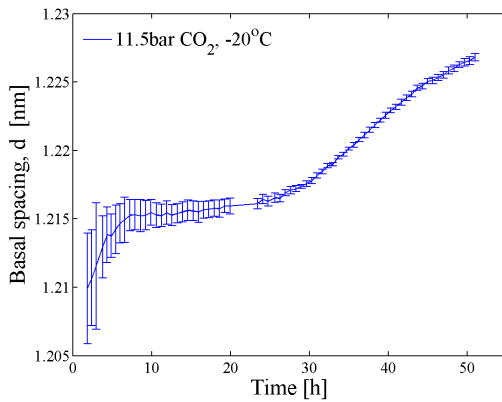
3.2 DISCUSSION OF X-RAY DATA



(a)



(b)



(c)

FIGURE 3.4: (a) Width Δq , (b) Position of intercalation peak, and (c) Basal spacing d_{001} as functions of time, during exposure to CO_2 at 11.5 bar and -20°C . The error bars reflect 95% confidence intervals, calculated from the goodness-of-fit parameter.

CHAPTER 3 DATA ANALYSIS AND DISCUSSION

tainty associated with it. As intercalation progresses, the uncertainty is significantly reduced.

A shift towards lower values of q is observed for the peak produced by CO_2 during the intercalation process. This corresponds to an increase in basal spacing d_{001} . Examples of the q -shift and corresponding basal spacing, as functions of time, are displayed in Figure 3.4.

We have found LiFh clay intercalated by CO_2 to have basal spacing $12.0 \text{ \AA} \pm 0.3 \text{ \AA}$, which means an expansion of the unit cell by $\sim 1.8 \text{ \AA}$ compared to the dehydrated state. It is worth noting that in our experiments the CO_2 peak has appeared at slightly different positions, which resulted in different values for the basal spacing. However, the variations are small; of same magnitude as the observed shifts in peak position. They could for instance be due to small differences in the calibration. Figure 3.4(c) corresponds to one of the largest observed basal spacings. A collection of figures for the other experiments is provided in Appendix A.1

CO_2 and H_2O intercalated smectite clays are almost indistinguishable by use of X-ray diffraction alone, due to the similar swelling behavior. Our findings are in line with this statement, as the basal spacing of monohydrated LiFh was found by Tenório et al [31] to be $d_{001} \sim 12.1 \text{ \AA}$.

The expansion of the unit cell Δd_{001} owing to CO_2 and H_2O intercalation in NaFh have been reported to be approximately 2.5 \AA [24] and 2.4 \AA [39], respectively. Also this clay show small differences in expansion, depending on the intercalated substance. However, the differences are so small that they could be a result of expected variations, as observed for LiFh intercalated by H_2O .

NaFh is observed to expand more than LiFh as a result of intercalation. The difference is most likely linked to the larger size of Na^+ as counterion. The dependence on cation-size for the unit cell expansion has been observed for several types of clays, such as montmorillonite [22, 49]. Furthermore, Fripiat and Aylmore [25, 49] linked the difference in cation size to the pore volume and absorption potential of smectite clays.

The observed shifts in d_{001} for the CO_2 -intercalated state during intercalation are of magnitude $\sim 0.1 \text{ \AA}$. The shift is probably due to a contin-

3.2 DISCUSSION OF X-RAY DATA

uous increase of CO_2 in the interlayer space, or reorganization of already intercalated molecules. A similar phenomenon has previously been observed for intercalation of H_2O in fluorohectorite clay [4], and is therefore not unexpected. The underlying mechanism is not yet understood, but the observation is in line with that intercalation of CO_2 resembles that of H_2O .

One possible explanation of the similar phenomena for hydrated clays is offered by da Silva et al [6]. They suggest that intercalated water can be categorized as localized or mobile, which have different influences on the rigidity and expansion of the clay crystallites. Thus, one possible explanation of the additional swelling could be assigned to mobile CO_2 . A more thorough presentation of their arguments and analogy to CO_2 is given in Section 3.2.2, in the discussion of peak width and position.

An extensive collection of peak widths, positions and basal spacings is presented in Appendix A.

Pressure dependence

It has already been shown that the rate of CO_2 intercalation in NaFh is pressure dependent, where higher pressure yields a faster process [24, 29]. We wanted to confirm a consistent behavior of LiFh.

Four experiments were performed for different pressures, at -20°C , to study the influence of pressure on the intercalation rate. Two of them were taken at similar pressures, 10 bar and 11.5 bar, while in the third experiment the dehydrated sample was exposed to CO_2 at 20 bar. The last experiment was not carried through until a stable intensity was reached, but still gives an indication of the intercalation rate at 5 bar pressure and -20°C .

In Figure 3.5 the intensity curves of these experiments are plotted together. They are normalized to their respective Kapton peak intensities. In line with previous observations by our group [24], we find the intercalation rate to be much higher in the sample exposed to CO_2 at high pressure, whereas the two series taken for similar pressures display almost identical slopes in the initial linear phase of exposure. The intercalation rate associated with the experiment at 5 bar is almost negligible compared to the other

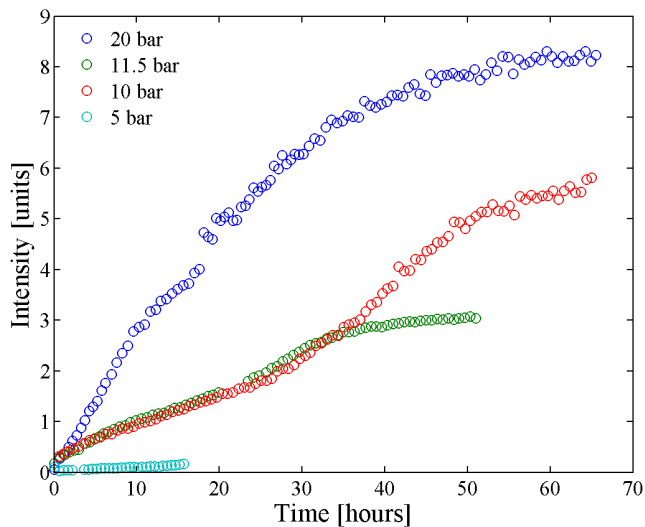


FIGURE 3.5: Comparison of intercalation peak intensities of different pressures, plotted together. Samples were cooled to -20 $^{\circ}\text{C}$.

experiments. Albeit a slightly steeper slope for the sample subjected to CO_2 at 11.5 bar, compared with the 10 bar experiment, it is not assumed to directly demonstrate the pressure dependence. The difference could be due to other variations, such as the amount of sample in the scattering volume, and is considered too modest to retrieve quantitative information on the pressure dependence.

Because four points are hardly enough to find a mathematical relationship between the pressure and temperature, I will not speculate further on what kind of relation this is. Still, our results support a pressure dependence of the intercalation rate, where higher pressure yields faster intercalation.

The curves display significant differences in terms of maximal intercalation peak intensity. The origin is unknown, but could for instance be due to different amounts of sample within the scattering volume.

3.2 DISCUSSION OF X-RAY DATA

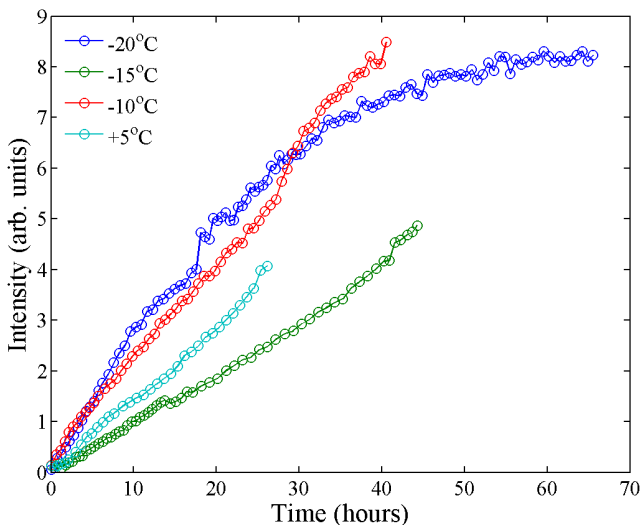


FIGURE 3.6: Comparison of intercalation peak intensities of different temperature conditions, plotted together. CO_2 at 20 bar pressure was used in all experiments.

Temperature dependence

The preliminary studies (Appendix B) indicated a possible temperature- or phase dependence of the kinetics of intercalation. However, the results from NTNU do not provide evidence of a relation between the intercalation rate and temperature.

The intensity curves in Figure 3.6 do not display a consistent behavior with temperature variations. The measurements carried out at 20 bar and 20 °C, -10 °C and 5 °C show a tendency of faster intercalation rate (in the linear regime) with temperature. However, the experiment carried out at the same pressure, but cooled to -15 °C displays a lower rate than any of the other experiments.

Some external factor might have caused the deviating behavior of the intercalation experiment at -15 °C. Potentially, more measurements might show that the trend observed for the remaining experiments represent the actual

CHAPTER 3 DATA ANALYSIS AND DISCUSSION

dependency of temperature and intercalation rate. The observed variations could also be due to other influencing factors and completely unrelated to the temperature.

Even if we are not able to draw any definite conclusions based on these results, it is worth noting that the differences in intercalation rate displayed upon temperature variation are much smaller than what was observed for different pressures. Thus, if CO₂ intercalation proves to be dependent of temperature, it is probably so to a much smaller extent than it is affected by pressure.

It is still not known what drives the intercalation process, and, to some degree, what the limiting factors are. If the intercalation of CO₂ into the interlayer can be assessed as a diffusion process, it would be expected to speed up with temperature. Closer packing of the clay would slow it down. As discussed, the issues associated with normalizing and comparing the intensity curves make it difficult to determine if slope differences are linked to the temperature conditions.

Based on the current results I would not be surprised if further experiments confirm that temperature has a minor effect on the dynamics of intercalation. However, even if it is the case, I find it probable that the effect of temperature is negligible only below a limit - as observed for deintercalation (see Section 3.2.3).

Indications of a two-CO₂-layer intercalation state

One LiFh sample was exposed to CO₂ at 20 bar and -20 °C for a long time after the intensity seemed stable. After more than 70 hours of exposure, a shoulder appeared to the left of the peak produced by intercalated CO₂. Slowly, the shoulder became more pronounced and a new peak appeared, at $q \sim 4.7 \text{ nm}^{-1}$. Figure 3.7 shows the scattered intensity as function of momentum transfer q for different times during exposure. Such a further expansion has, to my knowing, not previously been reported for CO₂-intercalated clay. It indicates a configuration where more than one layer of CO₂ is incorporated in the clay structure. The basal spacing of the new state corresponds well with a previously observed hydration state of LiFh.

3.2 DISCUSSION OF X-RAY DATA

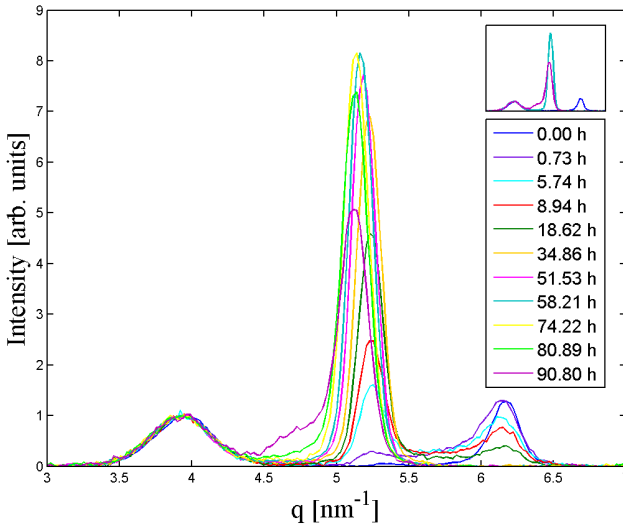


FIGURE 3.7: Scattered intensity as function of momentum transfer at different times during exposure to CO_2 . After reaching a stable intercalation peak intensity, another transition towards a state corresponding to higher basal spacing is observed. The transition is very slow. The inset shows the distributions of the sample in the dehydrated and one- CO_2 -layer states, in addition to the final scan which shows a distinct shoulder to the left of the peak produced by the latter.

Tenório et al observed a stable intercalation state of hydrated LiFh with $d_{001} \sim 14 \text{ \AA}$ [31]. This corresponds well with the 1.5 water layer state predicted Tambach et al [12], based on free-energy simulations on swelling montmorillonite clays with Li^+ as interlayer cation. The same behavior is not observed experimentally, or in simulations, for neither fluorohectorite nor montmorillonite clays with Na^+ as gallery cation. Tambach et al explained the phenomenon by the smaller size of the Li^+ cation and that it is well-accommodated in the water network. They claimed that the thermodynamic origin of swelling is a free-energy surface which separates the layered hydrates. The surface is dominated by the breaking and formation of hydrogen bonds within and between the water layers. Hydration states corresponds to minima of the surface. Li-montmorillonite was found to

CHAPTER 3 DATA ANALYSIS AND DISCUSSION

have one more of these than the same clay with e.g. Na^+ as gallery cation. The basal spacing of the additional hydration state is intermediate those of the 1 WL and 2 WL hydration states. The energy barrier which must be overcome for the clay to swell was also found to be lower for smaller cations.

As CO_2 molecules are nonpolar and do not form as strong intermolecular bonds as H_2O , one cannot uncritically employ the same model to CO_2 intercalation. Nevertheless, based on that the swelling behavior has been found to be similar upon intercalation with H_2O and CO_2 , and that the position of this new intercalation peak overlaps with the 1.5 WL state in the same way as the monohydrated and ordinary CO_2 -intercalated state; it is not unlikely that the model - with some modification - can provide new information on the swelling of smectite clays caused by CO_2 .

An alternative, explanation of the 1.5 WL peak is that it is caused by a simultaneous occurrence of two or more swelling states. When water is intercalated in for instance montmorillonite, 1 WL and 2 WL are in most cases found to be the most stable states. Peaks in the X-ray diffraction patterns, between the q-values of these hydration states, have been attributed to structural or chemical heterogeneities in the clay samples which could cause interstratification of intercalation states and result in an average basal spacing [50].

Without regard to which of these explanations hold for LiFh, they both correspond to an intercalation state where the interlayer expansion exceeds that corresponding to the previously observed one- CO_2 -layer state ($d_{001} \sim 12 \text{ \AA}$).

3.2 DISCUSSION OF X-RAY DATA

3.2.2 Heating and deintercalation

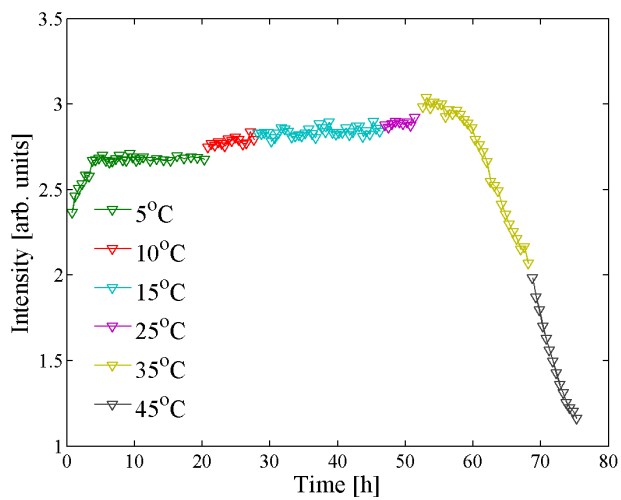
Experiments with stepwise increasing temperatures were performed to test at what temperature the CO₂ leaves the clay. If the peak produced by intercalated CO₂ peak remains unchanged, it indicates that the intercalation state is stable under the given condition, ergo; the molecules are retained within the clay structure. On the other hand, if the CO₂ peak intensity starts to decay, accompanied by a reappearing 0 WL peak, it can be interpreted as CO₂ leaving the clay interlayer. We call this deintercalation. Peak intensity curves for the heating experiments are presented in Figure 3.8. CO₂ is observed to stay intercalated in LiFh for temperatures up to 30 °C.

Beyond this limit deintercalation appears to speed up with increasing temperatures. The changes in peak width and position are in line with this tendency. Δq is inversely correlated to the peak intensity.

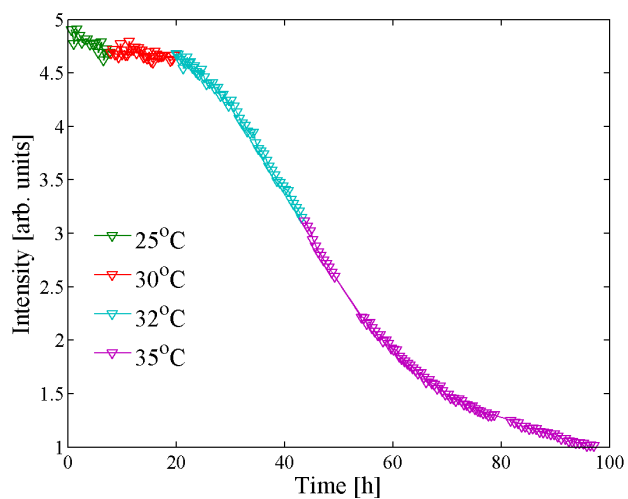
Figure 3.8(a) demonstrates a slight increase in intercalation peak intensity with time, for temperatures below the critical limit. The reason for this increase is not clear, but is likely due to either changes in X-ray absorption or reorganization of intercalated CO₂. The peak position is observed to shift even at temperatures where the peak shape remains unchanged. Similar behavior is observed for a humid sample at the same conditions (Section 3.2.3), and could also be due to reorganization of CO₂ within the clay layers. More data is presented in Appendix A.

In order to map the deintercalation process more closely, measurements were performed on a sample heated directly from -20 °C to 45 °C after the exposure to CO₂ was terminated. The cell was flushed with dry N₂ gas. Figure 3.9 shows the intensity distribution at different times while keeping the temperature fixed. The intercalation peak, initially at $q \sim 5.3 \text{ nm}^{-1}$, decreases in intensity and shifts towards higher q .

While heating, the peak produced by CO₂ becomes asymmetric and after a few hours a shoulder appears to the right of the peak. In Figure 3.9 it is recognizable in the frames taken after 13 hours of heating. The peak shape indicates a coexistence of intercalation states; dehydrated clay and layers still intercalated by CO₂. With time the dehydrated peak makes itself



(a)



(b)

FIGURE 3.8: Intensity as function of time, with stepwise increasing temperatures. (a) Stepwise heating from 5 to 45 °C. (b) Temperatures ranging from 25 to 35 °C.

3.2 DISCUSSION OF X-RAY DATA

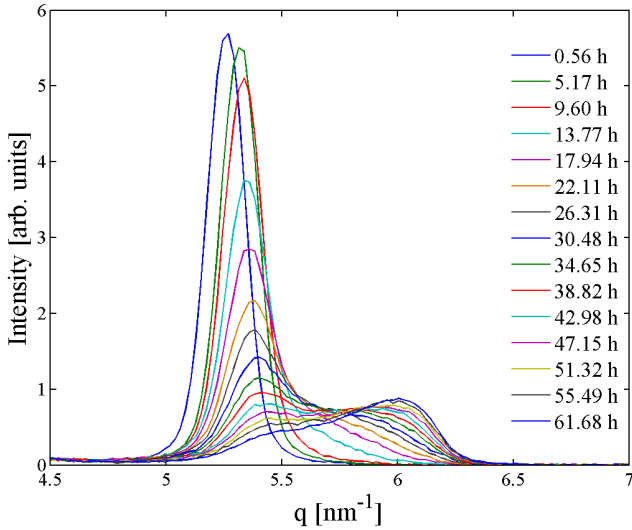


FIGURE 3.9: Intensity distribution as function of time, during deintercalation at 45 °C. Each curve represents the integrated intensity distribution of one frame. The CO₂ intercalation peak at $q \sim 5.2 \text{ nm}^{-1}$ decreases with time, while it shifts towards higher q . A peak corresponding to the dehydrated state reappears at $q \sim 6 \text{ nm}^{-1}$.

more pronounced. By the end of the experiment, after about 60 hours, the dehydrated peak intensity dominates that of intercalated CO₂.

The time evolution of the CO₂ peak intensity is displayed in Figure 3.10. In the beginning, the decay is slow, but speeds up after a few hours at high temperature. Subsequently, the peak intensity drops significantly for about 10 hours, before gradually approaching a value corresponding to no contribution to scattered intensity from clay with intercalated CO₂.

Peak width and position

Figure 3.11 displays the peak width Δq , peak position and basal spacing as functions of time, for a CO₂-intercalated sample kept at 45 °C. As ex-

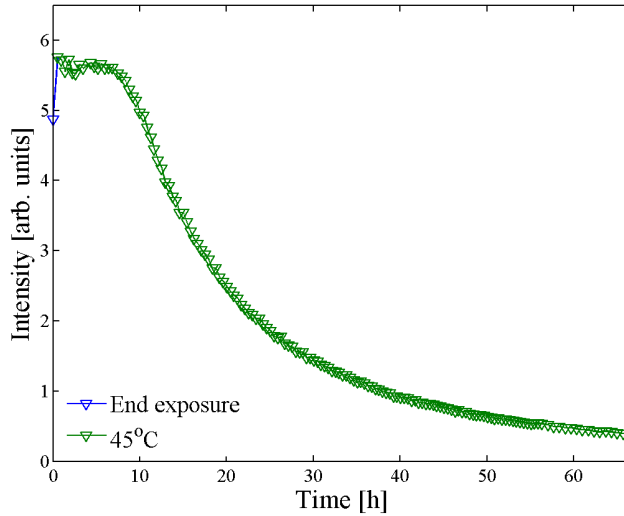


FIGURE 3.10: Intensity of intercalation peak as function of time, during deintercalation at 45 °C.

pected, as a counterpart to the observed behavior for CO_2 intercalation (Figure 3.4(a)), Δq is found to increase during deintercalation. When some interlayer gaps become dehydrated, or are no longer maximally expanded by CO_2 molecules, there will be a range of different interlayer spacings present in the sample. The observed intercalation peak will be a superposition of scattering by all coexisting states with basal spacing similar to d_{001} of the well-defined CO_2 -intercalated state. The result is a peak widening, as the variations in expansion by CO_2 and correspondingly the range of d_{001} increases, causing a growing portion of the incoming radiation to be scattered corresponding to smaller interlayer spacing.

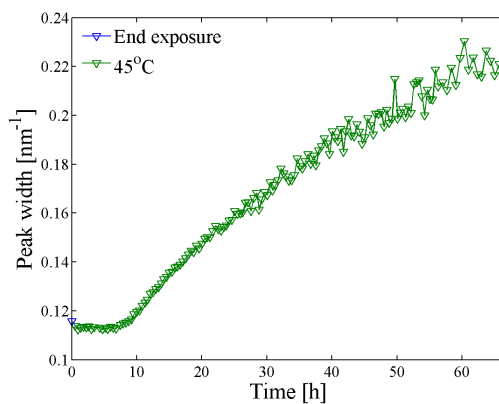
In line with this, the peak position (Figure 3.11(b)) is observed to shift towards higher q , corresponding to smaller d -spacing. After the initial slow phase, the increase is almost linear with time. There seems to be two contributions to the shift. One of them is of debatable origin (see Section 3.2.3), and is also observed when CO_2 - or water - is retained in the clay structure. This effect has also been reported for hydrated Li- and

3.2 DISCUSSION OF X-RAY DATA

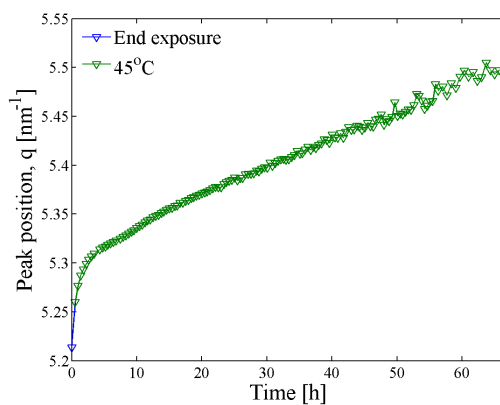
Na-fluorohectorite clays [4, 31].

The other source of the peak shift can be explained by the same phenomenon which is responsible for the peak widening. During the deintercalation process the shape of the diffraction patterns change gradually. When an increasing portion of the scatterers find themselves in a state corresponding to smaller d-spacing, the contribution to the diffraction pattern for q -values larger than the accurate position of the well-defined CO₂ intercalation state is increased. In the Pseudo-Voigt analysis a peak is fitted to the intensity distribution for scattering vector close to the expected center of the CO₂ peak, under assumption that it is due to diffraction solely from one characteristic interlayer spacing. The position of the net intensity peak consequently shifts towards higher q when an increasing portion of radiation is scattered corresponding to smaller expansion of the unit cell.

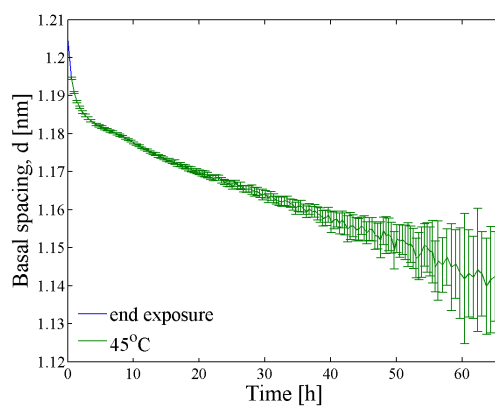
The observed behavior of the peak intensity, width Δq , position and corresponding basal spacing d_{001} is consistent for other samples heated to the same temperature.



(a)



(b)



(c)

60 FIGURE 3.11: (a) Width, (b) Position of CO_2 peak, and (c) Basal spacing as function of time, during deintercalation at 45°C . The error bars reflect 95% confidence intervals, calculated from the goodness-of-fit parameter.

3.2 DISCUSSION OF X-RAY DATA

3.2.3 Humidity test

A problem related to intercalation in clay samples, is that samples intercalated by H₂O and CO₂ are practically indistinguishable when only X-ray diffraction is used to probe the process, as the expansions of the interlayer in the monohydrated and CO₂-intercalated states are almost identical. Investigation of samples by means of other techniques, such as IR spectroscopy [18, 25], have been employed to provide direct evidence of presence of CO₂.

Here we have shown that even if the appearance of the respective peaks is similar, the response to heating is quite different. A sample of humid LiFh was loaded and cooled while flushing N₂, as in the standard intercalation experiment. When the target temperature was reached the gas outlet was plugged and the sample exposed to high pressure N₂ gas. Samples prepared in this way were put through similar heating experiments as samples intercalated by CO₂. Both kinds of samples were heated in steps in order to map the behavior of the respective intercalation peaks. The evolutions of the peak intensities are displayed in Figure 3.12.

From these curves it is evident that the CO₂ intercalation peak intensity starts decaying for temperatures exceeding 35 °C, while the 1 WL peak remains at least as intense as before. The slight increase in intensity, which can be observed for the hydrated sample, could be due to reorganization of the intercalated water. This could also explain the curve shape of the CO₂ peak intensity for temperatures below 35 °C¹.

Because the time scales of these temperature series differ somewhat, another heating experiment was performed to rule out that a time dependency influenced the outcome of the test. New samples were heated directly to 45 °C in dry N₂ atmosphere.

Figure 3.13 shows the behavior of the CO₂ intercalation peak in comparison with a monohydrated sample at 45 °C. The intensity of the CO₂ peak drops after some time, while the peak produced by intercalated water remains stable for more than 25 hours.

¹Closer investigation indicates deintercalation of CO₂ for temperatures exceeding 30 °C, as discussed in Section 3.2.2

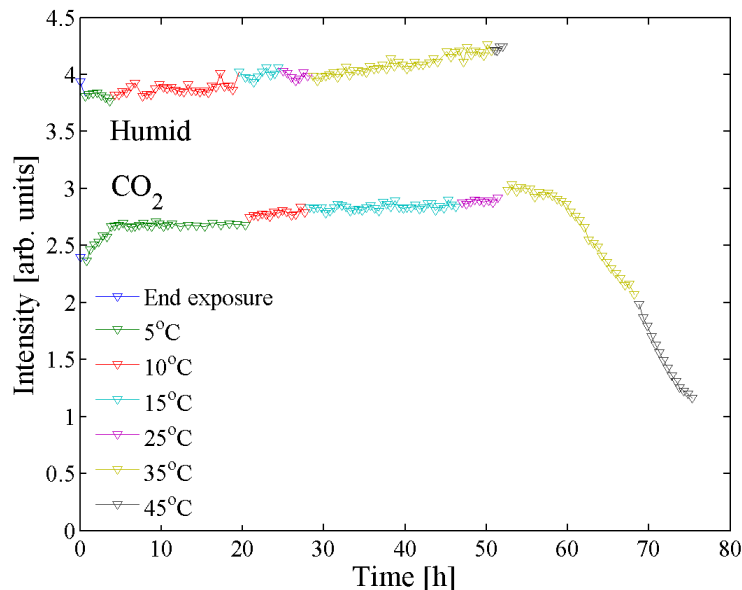
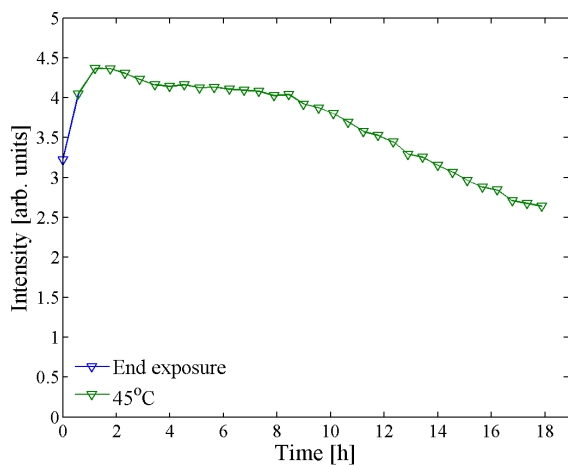


FIGURE 3.12: Intensity evolutions at different temperatures. Time series for LiFh samples intercalated with one water layer (upper) and CO_2 (lower), respectively. The intercalation peak of the sample with CO_2 decreases for temperatures exceeding 35°C , while that of the humid sample remains stable.

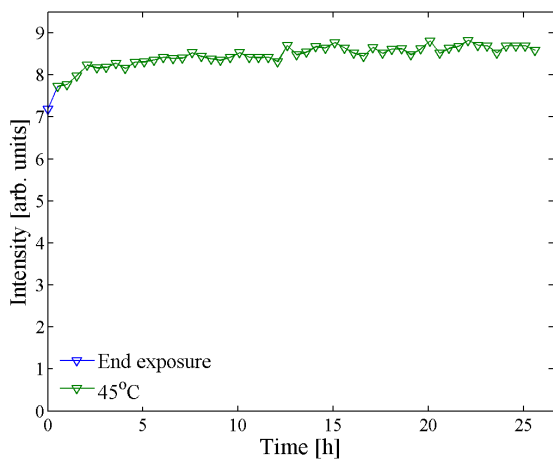
For the structurally similar clay NaFh, da Silva et al [6] found the monohydrated configuration to be the stable state, for temperatures between 35°C and 70°C . The same group also observed [31] a new hydration state of LiFh, between a 1 WL and 2 WL hydrate. The 1.5 WL state of LiFh is primarily stable within the range of relative humidity (RH) where NaFh is found in the 2 WL state. For LiFh the monohydrated state was found to be stable for relative humidity below $\sim 45\%$, compared to $\sim 50\%$ for NaFh.

This suggests that the two clays should be stable in the monohydrated state on a similar temperature range. Thus, it is likely that, in an atmosphere of moderate humidity and 45°C , the monohydrated state is the stable configuration also for LiFh.

3.2 DISCUSSION OF X-RAY DATA



(a) CO₂



(b) H₂O

FIGURE 3.13: Intensity evolutions during heating to 45 °C, while flushing with N₂ gas. (a) Dehydrated LiFh intercalated with CO₂, (b) LiFh with one water layer intercalated.

CHAPTER 3 DATA ANALYSIS AND DISCUSSION

If the samples in the heating experiments were intercalated by the same substance one would have expected similar behavior. Thus, the substance which causes the structural changes observed by in situ X-ray diffraction is neither residual H₂O nor caused by a leak of ambient humidity. This supports the previous observations [24] that CO₂ can penetrate the interlayer and cause expansion of fluorohectorite clays.

CO₂ deintercalates the LiFh interlayer at temperatures exceeding a certain temperature, while water stays intercalated at temperatures beyond this limit. This is not surprising, as the hydrated state has previously been observed [6] to be the preferred state of NaFh for temperatures up to 60 °C. Heating a LiFh sample to a temperature between the retainment limits of CO₂ and H₂O could be a means to distinguish the two substances with X-ray diffraction as only probe (without use of IR or NMR spectroscopy), which has until now not been considered possible.

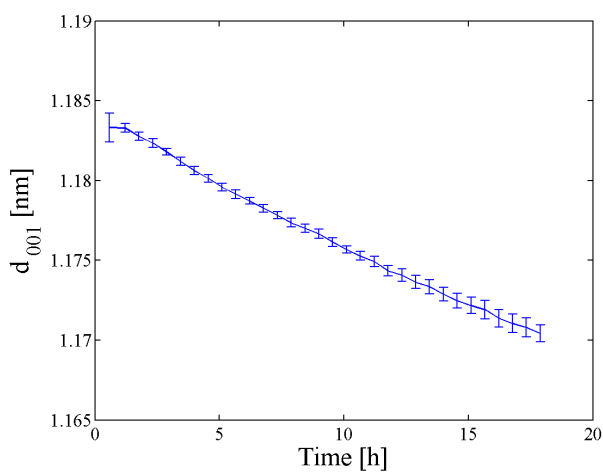
Peak widths and positions upon heating

As discussed in Section 3.2.2 and shown in Figure 3.11(a), the width Δq of the peak produced by intercalated CO₂ increases when the guest substance leaves the interlayer gap. The humid sample does not display a significant peak widening, as is expected when water is retained within the clay.

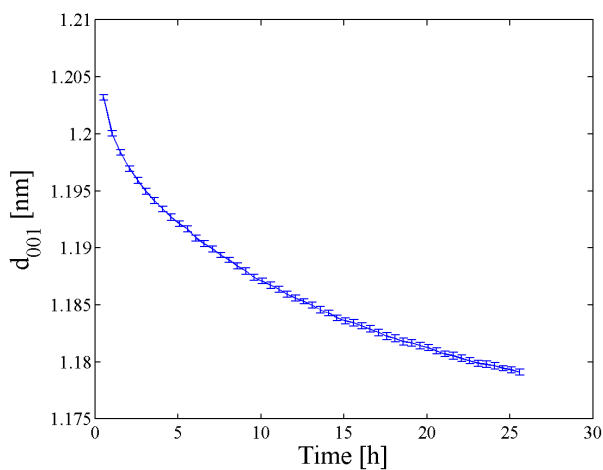
The peak positions shift corresponding to a decreased basal spacing for both samples. The reasons for this have already been discussed for LiFh intercalated by CO₂. It is not known why this also occurs in samples which do not seem to undergo any major structural changes, but a similar observation by da Silva et al [6] might shed some light on the phenomenon.

They observed a decreasing basal spacing of the 1 WL state upon heating of hydrated NaFh, at temperatures beyond 35 °C. They offered an explanation based on water mobility simulations in clay systems [51], suggesting that a stable situation includes two distinct populations of intercalated water molecules: A mobile nonlocalized fraction; and an immobile fraction which can be identified with the hydration shell of the cations or lying within the hexagonal ring of SiO₄ tetrahedra. Da Silva et al suggested that the decreasing basal spacing in monohydrated smectites upon heating can

3.2 DISCUSSION OF X-RAY DATA



(a) CO_2



(b) H_2O

FIGURE 3.14: Basal spacing d_{001} as function of time for (a) Sample intercalated by CO_2 , and (b) Humid sample, at 45°C . The spacing is observed to decrease both for the deintercalating CO_2 sample and the humid sample, which is stable.

CHAPTER 3 DATA ANALYSIS AND DISCUSSION

be attributed to the localized water, which contributes to the rigidity of the clay-water system. If such a change in the structure of the localized water occurs also at a fixed temperature, it could be the reason for the observed change in basal spacing, as demonstrated in Figure 3.14(b).

As CO_2 is nonpolar, and thus not strongly coupled to the interlayer cations, the fraction of localized CO_2 is probably smaller than for H_2O intercalation. For a humid sample, it is expected that an increasing amount of mobile H_2O intercalating the clay demands more space, and vice versa during heating. The observations for H_2O [6, 51] provides a possible explanation for the shifting intercalation peak position also during exposure to CO_2 .

3.2 DISCUSSION OF X-RAY DATA

3.2.4 Hydrated CO₂ intercalation states

As CO₂ capture and storage is becoming a reality, it is important to gain a better understanding of, and optimize, the processes involved; transportation, injection and long-term effects of storage. Experiments and simulations are performed to study flow of CO₂ in pipelines [52, 53], and intercalation of CO₂ [22, 54, 55] under conditions relevant for geological storage.

Both oil- and sub-terrain reservoirs are often naturally clay-rich and humid environments. Thus, CO₂ would have to intercalate clays which are already hydrated. The conditions used for our experiments are far less extreme than those relevant for geological storage ($P \gtrsim 25$ bar and $T \gtrsim 80$ °C). Still, we found it interesting to investigate if intercalation occurred at conditions close to ambient.

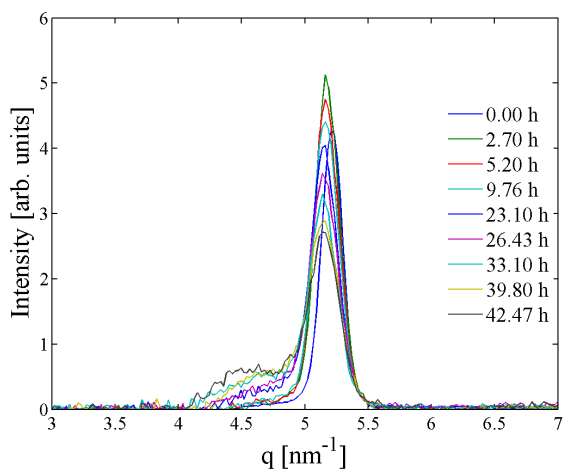
We performed one experiment to attempt CO₂ intercalation in a hydrated state. A sample of humid LiFh was exposed to CO₂ at -20 °C and 20 bar. Some possible outcomes could have been a mixed intercalation state, an exchange of H₂O for CO₂ in the interlayer gap, or an unchanged configuration.

Exposure to CO₂

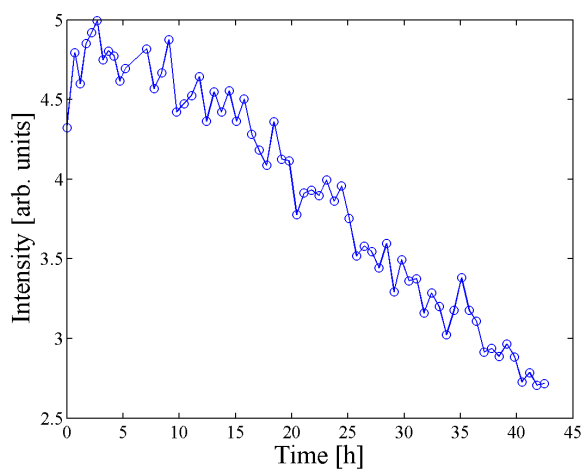
Figure 3.15 shows how the intensity distribution and peak intensity evolve under exposure to CO₂. It is clear that the characteristics differ from what is observed for dehydrated clay samples. In the case of a hydrated sample, the initial intensity distribution corresponds to a strong intercalation peak with q -value close to that of samples intercalated with one layer of CO₂. This peak is produced by the monohydrated state (1 WL).

As can be seen in Figure 3.15 the intensity starts decreasing almost immediately after exposure is initiated, and decreases more or less linearly throughout the experiment. The peak width Δq also increases almost linearly with time (displayed in Appendix A, Figure 3.16(a)).

One very interesting feature which can be seen in Figure 3.15(a) is the second Bragg peak which appears at $q \sim 4.5 \text{ nm}^{-1}$. It indicates a mixed



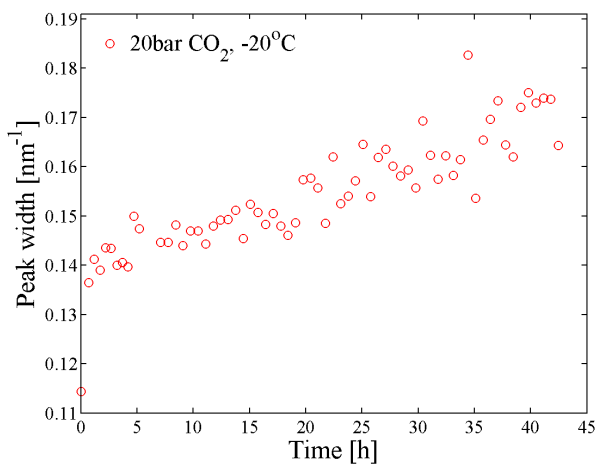
(a)



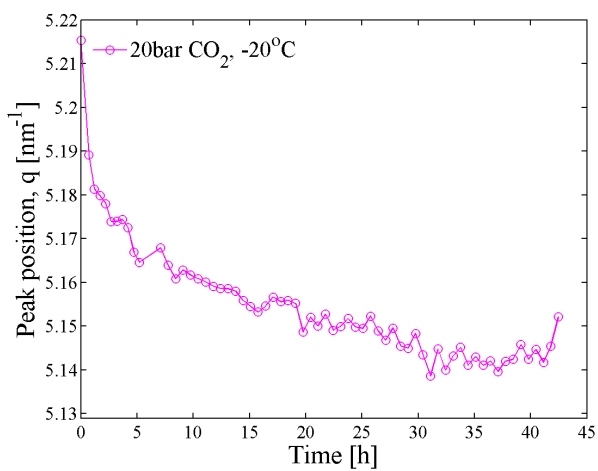
(b)

FIGURE 3.15: Humid LiFh sample exposed to CO_2 at -20°C and 20 bar. (a) Intensity distribution at different times during exposure, and (b) Peak intensity as function of time.

3.2 DISCUSSION OF X-RAY DATA



(a)



(b)

FIGURE 3.16: (a) Peak width Δq , and (b) Position q as function of time, for humid LiFh sample exposed to CO_2 at -20°C and 20 bar.

CHAPTER 3 DATA ANALYSIS AND DISCUSSION

intercalation state. The q -value of the second peak corresponds well with that of 1.5 water layers reported by Tenório [31]. It could be due to an intercalation state of 1.5 water layers separated from CO₂, or CO₂ and H₂O both incorporated into the same interlayer. It is also possible, although unlikely, that the peak stems from a state of more than one layer of CO₂.

If the peak originates from a pure 1.5 WL state, it would correspond to H₂O becoming more closely packed in a small fraction of the particles. Any intercalated (single-layer) CO₂ would contribute with scattering at similar q as the 1 WL state. Another possibility is that the new peak is due to a state where the two substances occupy the same interlayer. It is also possible that there is a coexistence of multiple intercalation states in the sample; CO₂, 1 WL, 1.5 WL, and a state where CO₂ and H₂O occupy the same interlayer. The configuration that is the natural state under the given conditions, would be that corresponding to a free energy minimum under the given conditions.

Independently of which configurations are present in the sample, it is clear that an additional expansion of the interlayer gap occurs in a small fraction of the sample. The additional Bragg peak does not seem to correspond to a preferred configuration, as the transition was very slow and the peak disappeared quickly after exposure to CO₂ was terminated.

Conformable to other samples, the peak position shifts to lower q during exposure to CO₂. The peak becomes wider during the transition to the mixed intercalation state. The contribution from the growing shoulder to the left of the peak is to some degree accounted for in the Pseudo-Voigt analysis by fitting the peak from its right side.

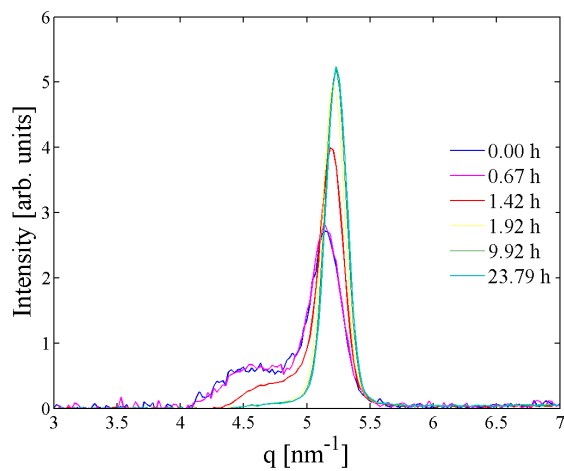
3.2 DISCUSSION OF X-RAY DATA

Heating

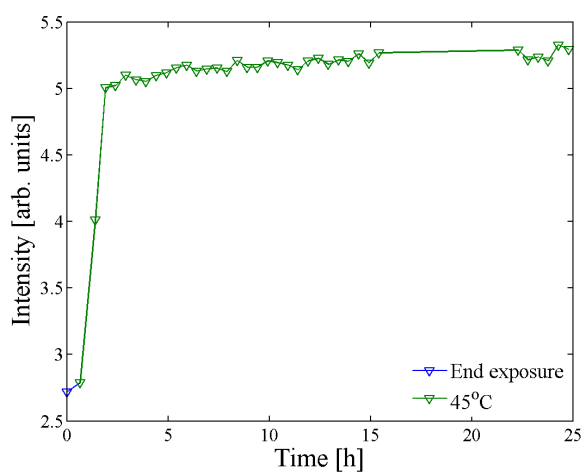
The source of the second peak has not been identified. When the sample was heated to 45 °C in a dry N₂ atmosphere, the peak disappeared within an hour or two (see Figure 3.17(a)). This shows that the resulting configuration after exposure was not stable at those conditions. CO₂ is expected to deintercalate otherwise dehydrated LiFh at the given conditions. Furthermore, based on the findings by Ternório and da Silva [6, 31] H₂O is expected to be retained in LiFh at 45 °C (see discussion in Section 3.2.3), but in the monohydrated state. Consequently, if the second peak observed at low temperature and high pressure was produced by either a 1.5 WL state or a configuration involving CO₂, the observed change in diffraction patterns is expected.

Flushing with N₂ at a lower temperature could possibly yield a different behavior. Still, it is likely that - even if the observed peak is associated with intercalated CO₂ - the behavior in the hydrated state would differ from that observed for dehydrated clay. Thus, the temperature limit for deintercalation would probably not be the same.

If the clay was, at some point, intercalated by CO₂, it does not appear to remain in this state. Reorganization back to the initial hydrated 1 WL configuration seems to occur shortly after heating started. After a short phase of increasing CO₂ peak intensity (see Figure 3.17(b)), it remains almost constant. This behavior is in line with that of a humid sample at 45 °C (Figure 3.13(b)).



(a)



(b)

FIGURE 3.17: (a) Intensity distribution at different times, and (b) Intercalation peak intensity as function of time, for humid LiFh sample after exposure to CO_2 . Heating to 45°C in dry N_2 atmosphere. The second intercalation peak disappears within two hours.

3.2 DISCUSSION OF X-RAY DATA

3.2.5 Natural hectorite

Intercalation was also attempted for natural hectorite samples. Due to an overlap of the intercalation peak with that produced by the Kapton window, it was more difficult to conclude on the results. The intensity of the dehydrated peak was observed to decrease, but the overlap hindered us from determining how the shape of the intercalation peak changed. Furthermore, it was not possible to tell whether the sample was in fact dehydrated before exposure to CO_2 .

Examples of diffractograms recorded for the natural hectorite clay SHCa-1 in dehydrated and 1 WL intercalation state are presented in Figure 3.18.

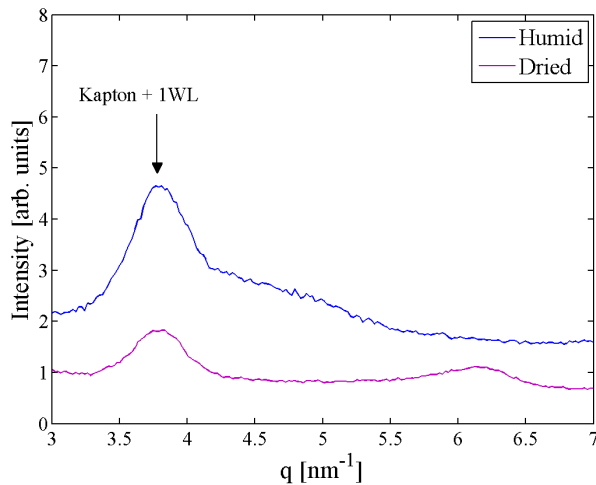


FIGURE 3.18: The natural hectorite clay SHCa-1 in dried (pink) and 1 WL hydrated (blue) states. It is clear from the intensity distribution of the hydrated sample that there is an overlap of the peaks from the sample and that produced by the Kapton window, at $q \sim 3.8 \text{ nm}^{-1}$.

Other sources of uncertainty in these experiments are the contribution to scattering from other substances in the clay and variations in the structure, which can mask the behavior of the clay. Natural clays have a less homogeneous layer charge distribution, compared to synthetic clays, which yields

CHAPTER 3 DATA ANALYSIS AND DISCUSSION

a coexistence of intercalation states within the clay crystallites [39]. This is reflected in the diffraction pattern as wide and poorly defined peaks. Some major impurities in natural clay samples are quartz, carbonates and iron oxides [56]. By purifying the samples through sedimentation or centrifugation we could probably have obtained less dubious diffraction patterns.

3.3 Discussion of IR data

When evaluating vibrational spectra, it is important to know where to look for an effect of the phenomenon of interest. Clays display many characteristic bands and modes, which have been well mapped for many types of clay [57]. One would expect differences in the spectra of samples intercalated by CO₂, H₂O and dehydrated clay samples. For instance, there should be differences in the bands originating from H₂O (wavenumbers $\sim 1630\text{ cm}^{-1}$) and the bands caused by interaction of the hydration water and interlayer cation. Also, for clays containing hydroxyl groups, changes in the OH stretching mode at $\nu \sim 3600\text{ cm}^{-1}$ would be expected.

Under extreme heating conditions it has also been observed that bands shift and change intensity, due to e.g. dehydroxylation (which occurs in natural hectorites and other clays with OH-groups in the octahedral layers) [58], or charge reduction (in hectorites this is caused by substitutions of Li⁺ by Mg⁺ in the octahedral sheet upon heating) [59]. One outcome of charge reduction is a shift of the SiO stretching band, usually detectable somewhere between 990 and 1040 cm⁻¹, to lower wavenumbers.

One of the easiest ways to identify intercalated CO₂ is to look for additional absorption at frequencies close to characteristic CO₂ modes, compared to a dehydrated or humid clay sample. Loring et al [18] investigated the changes in the asymmetric CO stretching band in Ca-saturated Montmorillonite, under exposure to supercritical CO₂. This was the same band Fripiat et al [25] used to advocate CO₂ intercalation in smectites. The CO asymmetric stretch contributes to absorption at $\nu \sim 2350\text{ cm}^{-1}$.

For the IR measurements we used an old FTIR spectrometer, which is normally used for educational purposes. As we do not have direct access to a modern FTIR spectrometer, this equipment was used for a first attempt to study the clay films by use of IR.

Even though the sample chamber atmosphere was primarily N₂, the IR radiation also passes through a chamber with presence of atmospheric gases. In spite of our efforts to reduce the background by flushing the optical system with N₂ gas (which reduced the humidity), CO₂ still caused a substantial amount of absorption. This can be seen by the strong line at $\nu \sim$

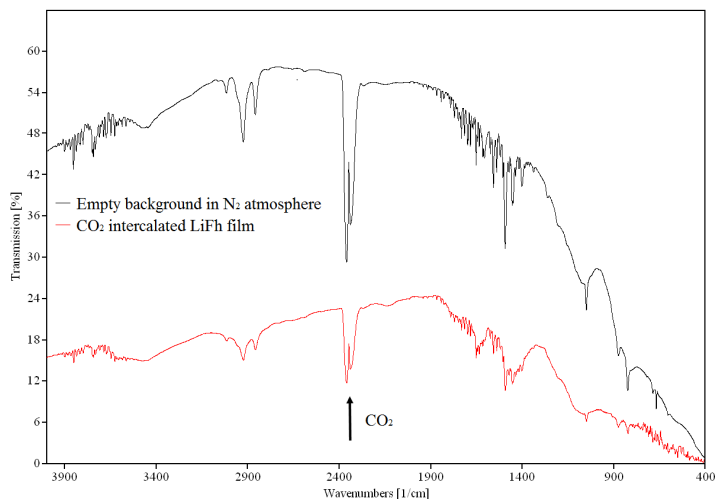


FIGURE 3.19: IR transmission spectra of the background of the experimental setup and LiFh film. The absorption by humidity is within acceptable range, but atmospheric CO_2 causes a loss of sensitivity. The antisymmetric CO stretch is indicated.

2350 cm^{-1} of the background scan displayed in Figure 3.19. This causes a considerable loss of sensitivity at frequencies corresponding rotation-vibrational modes of CO_2 .

For comparison, spectra were taken for a CO_2 -intercalated sample and one which had been kept at ambient conditions. We observed some differences in the spectra from the films. Still, they are too small to provide evidence of CO_2 in the films. Figure 3.20 displays a the ratio spectrum of the LiFh film, relative to the background. It displays a difference in absorption for the antisymmetric CO stretch, but not sufficiently to determine if it is due to the film or random variations in the background. Due to the low sensitivity around the line of the asymmetric CO_2 stretch, it is impossible to determine whether the differences in absorption by CO_2 can be credited to CO_2 in the LiFh film, or if they must be credited to random variations in the background.

As the thickness of the LiFh film (order of magnitude μm) is very small

3.3 DISCUSSION OF IR DATA

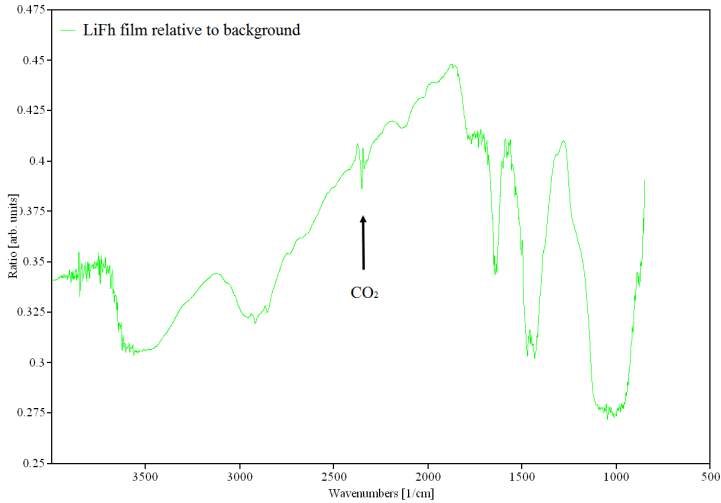


FIGURE 3.20: IR absorption spectrum of self-sustaining LiFh film relative to background. The antisymmetric CO stretch is indicated.

compared to the total optical path, the expected amount of CO_2 confined in the film is almost negligible compared to the total amount of CO_2 in the beam path. In order to get conclusive results, a setup with higher sensitivity for CO_2 must be used. This would preferably be one where the radiation passes through vacuum or a satisfactory inert atmosphere.

For measurements taken with a sufficiently high sensitivity for CO_2 presence, one would expect to see a difference in spectra of CO_2 -intercalated and humid film in the region corresponding to the asymmetric CO stretch. The sample exposed to CO_2 is expected to absorb more at wavenumbers in proximity to this mode. Also, the peak shape could provide some information on how closely packed the CO_2 is.

If the molecules are packed closer together than in the gaseous state, the observed peak formation centered around $\nu \sim 2350 \text{ cm}^{-1}$ is likely to be a double peak. The two peaks would be caused by the P- and R bands of the asymmetric CO stretching mode. At low gas pressures the molecules can rotate almost freely. Thus, in the spectra, the rotational-vibrational

CHAPTER 3 DATA ANALYSIS AND DISCUSSION

lines are visible. As the pressure increases, molecule collisions become more frequent, which limits the free rotation. This rotational relaxation is reflected by a broadening of rotational fine structure, which collapses into broad peaks on either side of the vibrational center, corresponding to $\Delta J = 0$ (Q-branch). At even high relative pressures (beyond 60 bar for CO_2), the P and R rotational-vibrational branches are expected to merge into the Q-branch, taking on a Lorentzian-like shape [60].

Chapter 4

Concluding remarks

We have shown that CO_2 is able to intercalate in LiFh for a range of conditions in terms of pressure (5 bar to 20 bar) and temperatures (-20 °C to 5 °C). The basal spacing of the intercalated state is found to be approximately 12.0 Å, corresponding to an expansion of the unit cell by 1.8 Å. The observed swelling behavior is very similar to that observed for hydrated LiFh.

We have observed that the rate of intercalation increases with higher pressure, similar to the case of NaFh. In order to further map and quantify this dependence, more experiments will have to be performed. More investigations will also have to be done to conclude on the temperature dependence, but the temperature appears to affect the intercalation to a smaller extent than pressure. In any case, CO_2 intercalation is a slow process. Even under pressures of 20 bar, intercalation of CO_2 is slower than H_2O intercalation in fluorohectorites by orders of magnitude.

Previous studies have indicated that the size and charge of the interlayer cation influence the swelling properties of clay, for intercalation of both H_2O and CO_2 . The results presented in this manuscript, along with those obtained for LiFh and NaFh in the preliminary measurements, support this observation.

In situ observations of CO_2 -intercalated LiFh upon heating revealed that

CHAPTER 4 CONCLUDING REMARKS

CO₂ is retained within the interlayer at room temperature, and only starts leaving the clay above 30 °C. To our knowledge, this is the first time CO₂ retention in clays has been shown at room temperature. The observed differences in behavior for samples intercalated by CO₂ and H₂O also suggests a new method for distinguishing the two substances solely by X-ray diffraction, without having to confirm presence of CO₂ by NMR or IR spectroscopy.

For the first time, to my knowing, a state corresponding to intercalation of more than one layer of CO₂ into the interlamellar space of fluorohectorite has been observed by X-ray diffraction. In terms of basal spacing it corresponds well with the 1.5 WL hydration state observed by Ténorio et al [31]. Considering the very slow transition to the second intercalation state, it is rather unlikely that a consecutive transition to a CO₂ intercalation state similar to the 2 WL state will occur at these conditions. If this transition also occurs at lower pressure and other temperatures is still unknown.

We have also observed changes in the intercalation state of a monohydrated LiFh sample under exposure to CO₂. Simulations for montmorillonite clays [12] offer a possible explanation as to why this hydration state, and the new CO₂ intercalation state, are not observed in NaFh clays. Based on free-energy calculations, the stable hydration states depend on the size of the interlayer cation. The smaller size of Li⁺ compared to Na⁺ results in a slightly different configuration with the intercalated water.

We believe that the findings, concerning both intercalation and deintercalation, could be relevant for the ongoing research related to application of clays for capture, transport or storage of CO₂.

Further studies

To better understand intercalation of CO₂ in fluorohectorite clays, the pressure and temperature dependence should be further mapped. Closer investigation of the pressure dependence at different temperatures might lead to a more quantitative model of the dynamics.

It would also be interesting to explore the limits of retention in other

clays. Heating experiments should be conducted for synthetic and natural samples such as NaFh and montmorillonite clays. Further, one could investigate if the humidity test is valid also for these clays.

Regarding application of clays for geological storage of CO₂, it would be interesting to study the behavior of CO₂-intercalated clay under exposure to humid air. In this context, further studies on CO₂-intercalation in clays with different relative humidity could prove useful. However, in this context it would probably be more relevant to study the behavior at pressure and temperature conditions closer to those used for geological storage.

To provide direct evidence of CO₂ intercalation in LiFh, IR measurements should be performed on LiFh films using an FTIR spectrometer with vacuum or dry N₂ atmosphere.

Appendix

Appendix A

Additional WAXS data

The following Appendix provides complementary data and analysis related to the experiments conducted for this Master's thesis. Experiments were carried out at the laboratory of the Complex group at NTNU.

APPENDIX A ADDITIONAL WAXS DATA

A.1 Supplementary figures: Intercalation

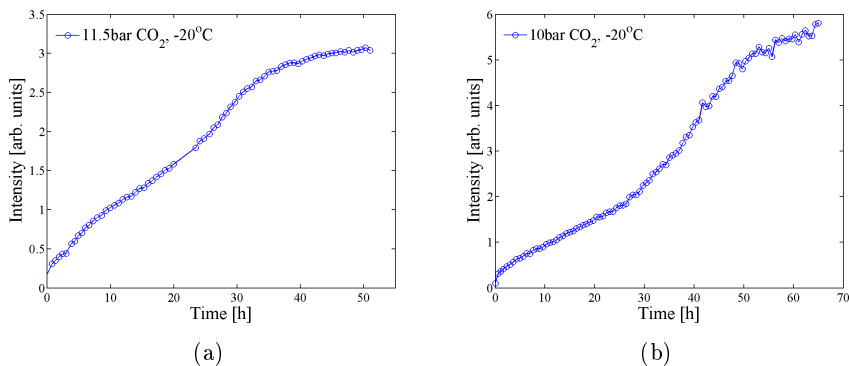


FIGURE A.1: Intensity of the intercalation peak as function of time during exposure to gaseous CO_2 at -20°C and pressures (a) 11.5 bar and (b) 10 bar. These are comparable conditions, but the shape of the curves show slightly different behavior in terms of linearity with time.

Figure A.1 presents the intensity of the intercalation peak as function of time for two experiments. As the majority of experiments were presented in the discussions of pressure - and temperature dependence in 3.2.1, they are not presented here. The two series are good examples of variations in curve shape for the experiments. They both correspond to intercalation experiments where LiFh was exposed to CO_2 for sufficiently long time to reach a stable maximum intensity.

Figure A.1(b) is a good example of how the intercalation rate seems to change during exposure to CO_2 , in the case presented here it occurs after about 25 hours. The process seems to accelerate before stabilizing at a higher rate of intercalation, where the curve is still more or less linear with time.

A.1 SUPPLEMENTARY FIGURES: INTERCALATION

Peak shape and position

The peaks were fitted to Pseudo-Voigt profiles. In Section 3.2.1 examples of the resulting peak widths, positions and basal spacings as functions of time were shown. In the following, we provide a more extensive collection of plots for the different experiments.

Figure A.2 shows the width Δq of the peak produced by CO₂-intercalated clay, as function of time, for several experiments. The behavior is consistent for all series, where the peak starts off as large, but as the intercalation sample becomes saturated with CO₂, Δq approaches a constant value.

Peak positions q of the CO₂ intercalation peaks are displayed in Figure A.3, and Figure A.4 shows the corresponding basal spacings d_{001} , with error bars representing 95% confidence intervals of the Pseudo-Voigt fit parameters.

A shift of the peak position towards lower q has been observed for all experiments. The shift is most likely due to a reorganization of intercalated CO₂, or further expansion as more CO₂ is absorbed by the clay. The change in q per unit time does not appear to depend on the pressure or temperature. The somewhat stepwise manner in which the position changes is very interesting, but the meaning is still not clear to us.

The basal spacing increases with time, in line with what is expected when more CO₂ is incorporated into the interlayer. Based on the associated uncertainty (reflected by the error bars), which decreases with time, it is clear that the clay takes on a well-defined intercalation state corresponding to all clay layers being similarly spaced.

APPENDIX A ADDITIONAL WAXS DATA

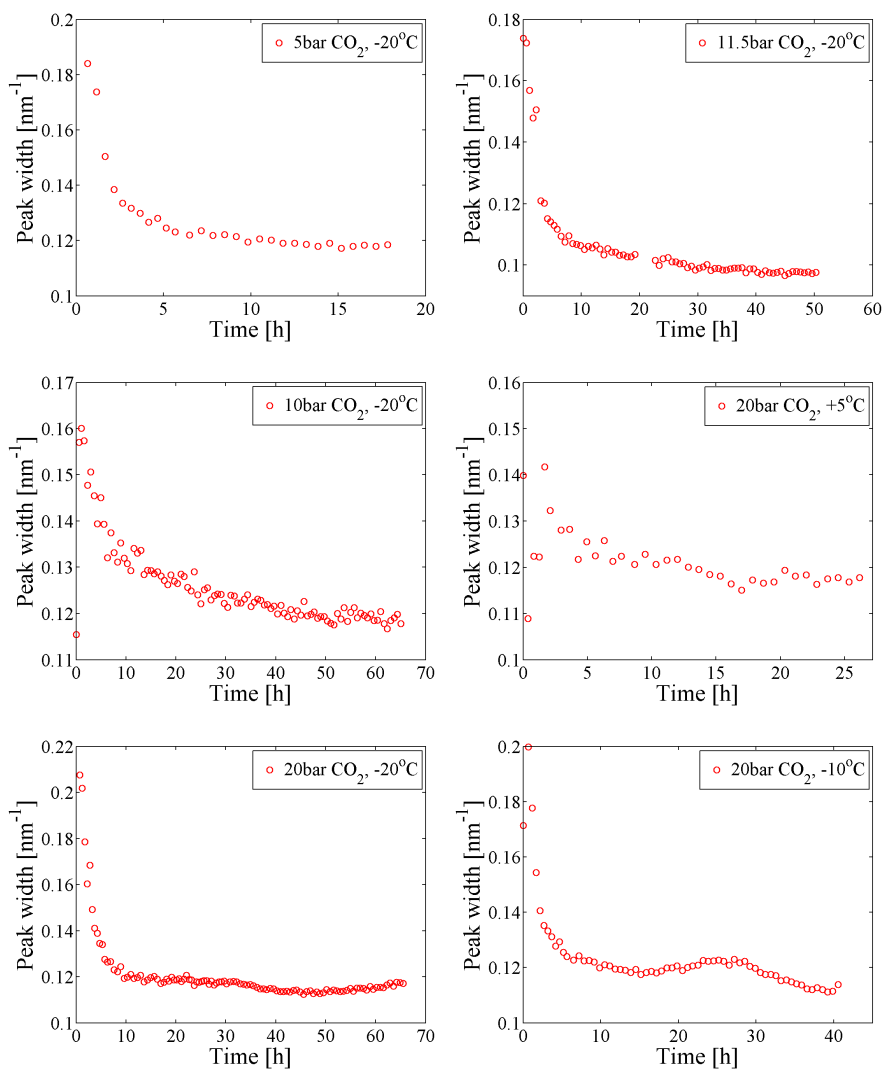


FIGURE A.2: Widths Δq of intercalation peaks as function of time, during exposure to CO_2 at different conditions.

A.1 SUPPLEMENTARY FIGURES: INTERCALATION

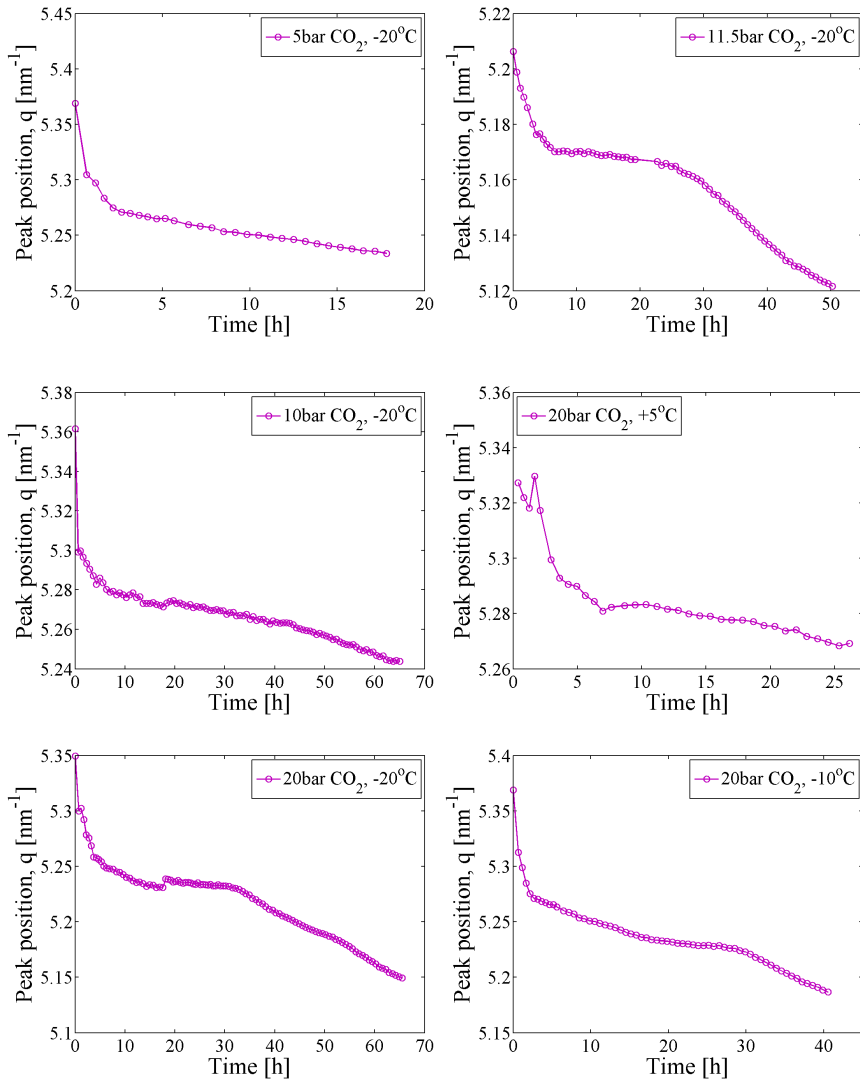


FIGURE A.3: Positions q of intercalation peaks as function of time, during exposure to CO_2 at different conditions.

APPENDIX A ADDITIONAL WAXS DATA

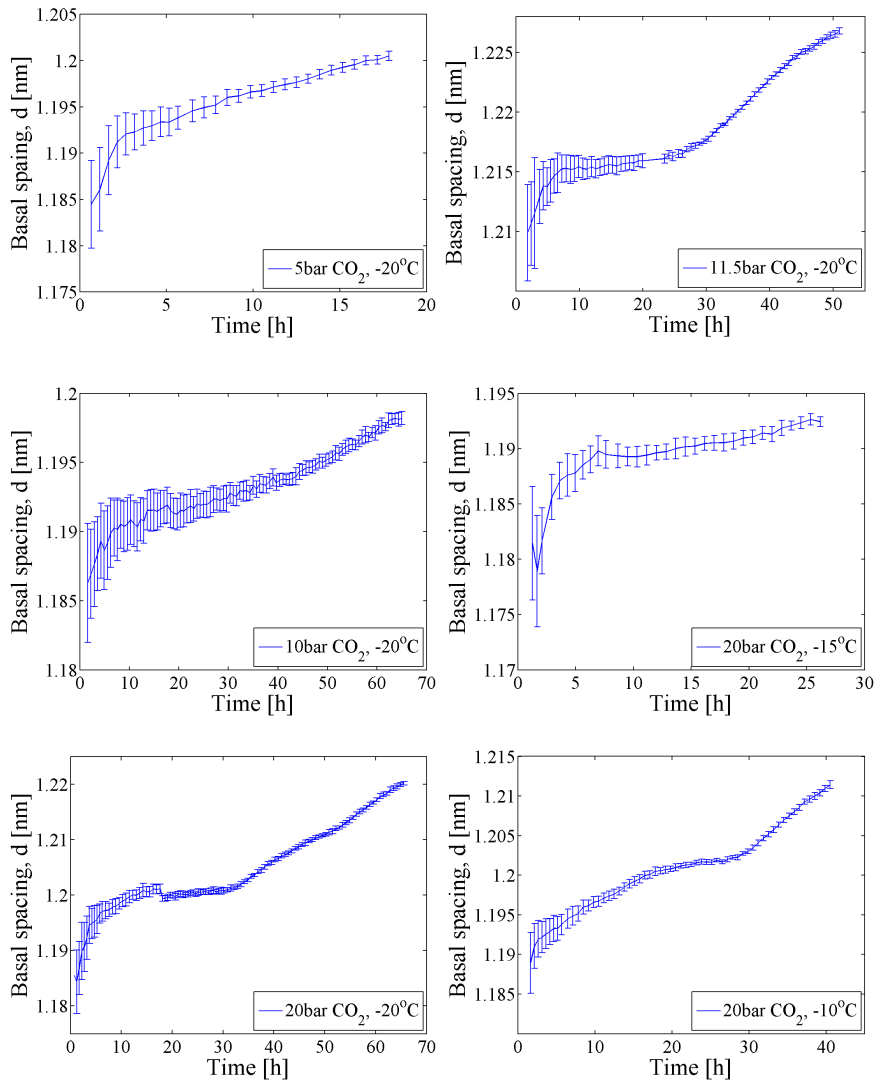


FIGURE A.4: Basal spacing d_{001} of the unit cell as function of time, during exposure to CO₂ at different conditions. Error bars reflect 95% confidence intervals, calculated from the goodness-of-fit parameter of the Pseudo-Voigt profiles.

A.2 Supplementary figures: Heating

A.2.1 Stepwise heating

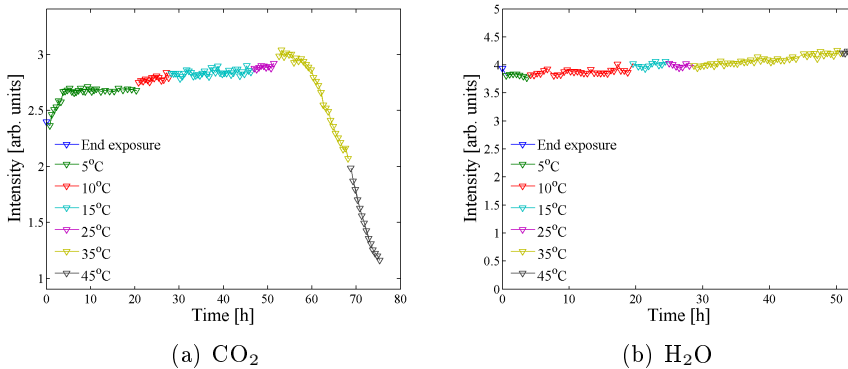


FIGURE A.5: Intercalation peak intensities at different temperatures, as functions of time. (a) Dehydrated LiFh intercalated with CO₂, and (b) Monohydrated LiFh.

Figure A.5 displays the behavior of LiFh clay intercalated by CO₂ and a monohydrated sample, while heated in steps in the range 5 °C to 45 °C. It is evident that the behavior is different for LiFh intercalated by the two substances, for temperatures exceeding 35 °C.

Figure A.6 displays the peak widths Δq and positions q for the experiments of heating CO₂-intercalated LiFh in steps. Δq remains stable at temperatures where the peak intensity curves indicates retention. This is in line with an unchanged peak shape, and supports the observation that CO₂ is retained in LiFh for temperatures up to 30 °C.

The peak positions shifts constantly during heating, correspondingly to a decrease in basal spacing. This is most likely due to a reorganization of the intercalated clay, and occurs even when CO₂ is assumed to remain intercalated. Based on the slope of Figure A.6(c), the decrease in basal spacing appears to speed up with higher temperature.

APPENDIX A ADDITIONAL WAXS DATA

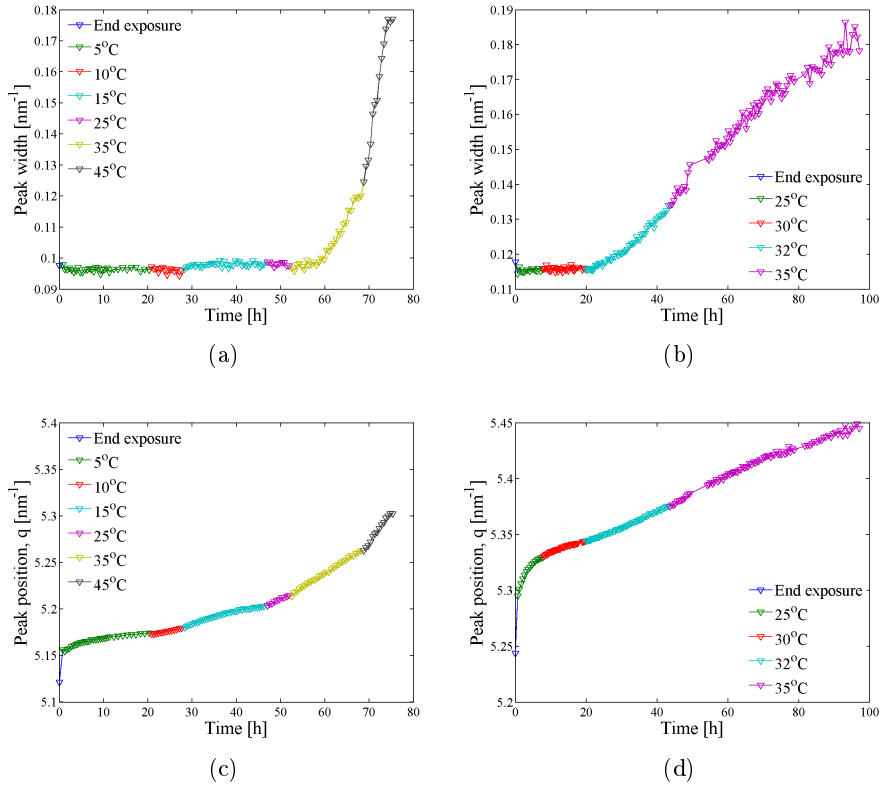
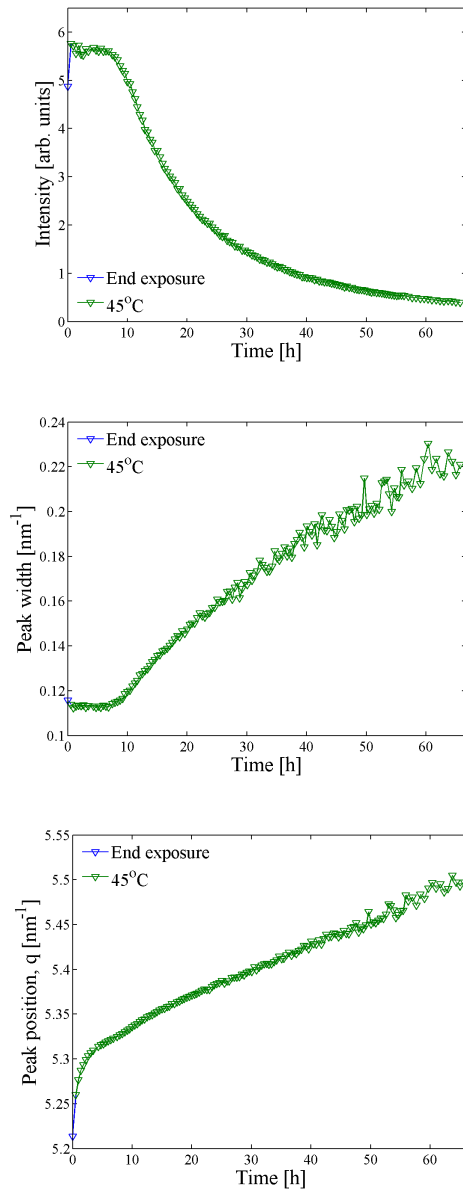


FIGURE A.6: Widths and positions of CO₂ intercalation peaks during stepwise heating. In (a) and (c) temperatures range from 5 °C to 45 °C. In (b) and (d) temperatures are in the range of 25 °C to 35 °C. A stable peak width is observed for both experiments until CO₂ starts leaving the clay, while the peak position shifts towards higher q -values even before deintercalation occurs.

A.2.2 Deintercalation at fixed temperature

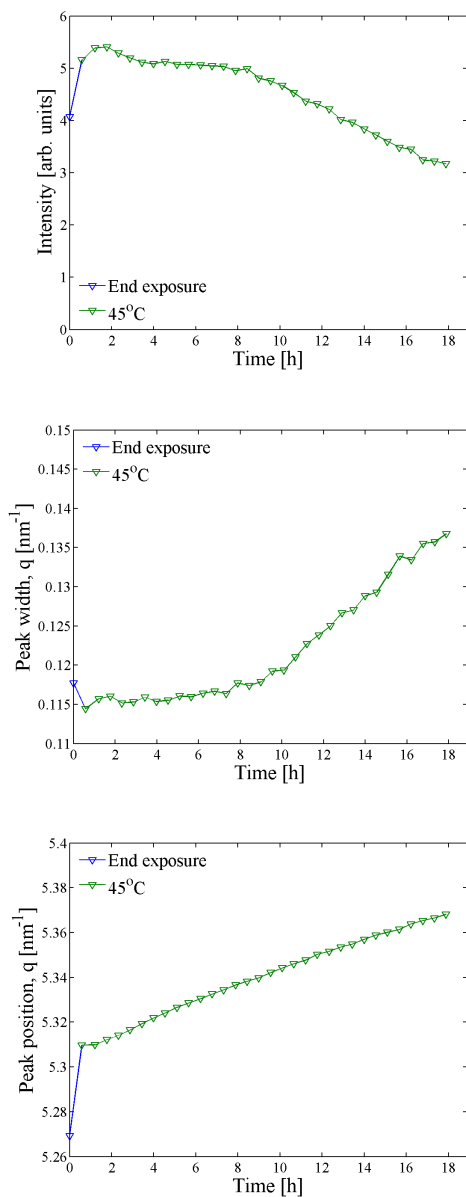
Figure A.7 displays the peak intensity, width and position of two experiments with CO₂-intercalated LiFh. In these experiments the samples were heated directly from -20 °C to 45 °C to avoid hysteresis effects. The time frames are different, but the two series show similar behavior in the initial

A.2 SUPPLEMENTARY FIGURES: HEATING



(a)

APPENDIX A ADDITIONAL WAXS DATA



(b)

FIGURE A.7: Intensity evolutions (top), peak widths (middle) and positions (bottom) of intercalation peaks as functions of time, during deintercalation at 45 °C. Figures (a) have a time frame of more than 60 hours, while in (b) the sample was kept at 45 °C for 18 hours.

A.3 HYDRATION STATES - PEAK SHAPE

phase. This supports that the reported observations represent consistent behavior.

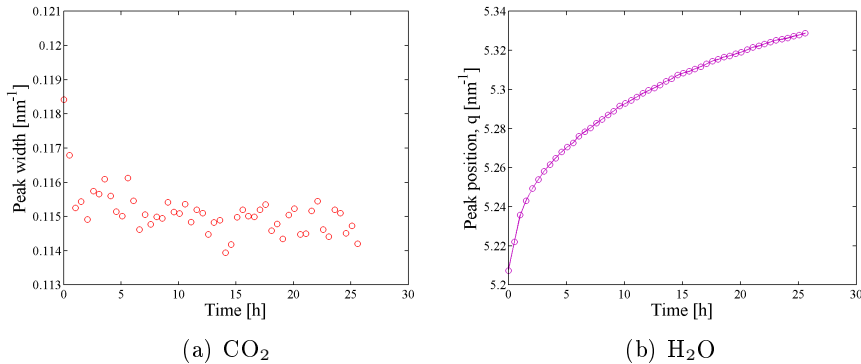


FIGURE A.8: (a) Peak width Δq , and (b) Position q as functions of time for a humid sample in the monohydrated state, kept at 45 °C in dry N_2 atmosphere.

Figure A.8 display supplementary information for the sample used for comparison in Section 3.2.3; the peak width and position of the humid sample under heating to 45 °C in a dry N_2 atmosphere. It is clear from the figures that the position shifts with time, as previously discussed, and that the peak width remains almost constant during the heating. This supports the previous observations that H_2O is retained in LiFh at the given conditions.

A.3 Hydration states - peak shape

Section 3.2.4 presents the observed behavior of a hydrated LiFh sample under exposure to CO_2 . The peak width Δq and position q of the Pseudo-Voigt profile fitted to scattered intensity on the q -range corresponding to one layer of CO_2 or the monohydrated state are displayed in Figure A.9. As previously discussed, the second peak is observed to decay quickly after the temperature is elevated, while the intensity of the one-layer state increases. As can be seen by the figures presented here, the width drops quickly, and the position shifts back to the position of the monohydrated state (before

APPENDIX A ADDITIONAL WAXS DATA

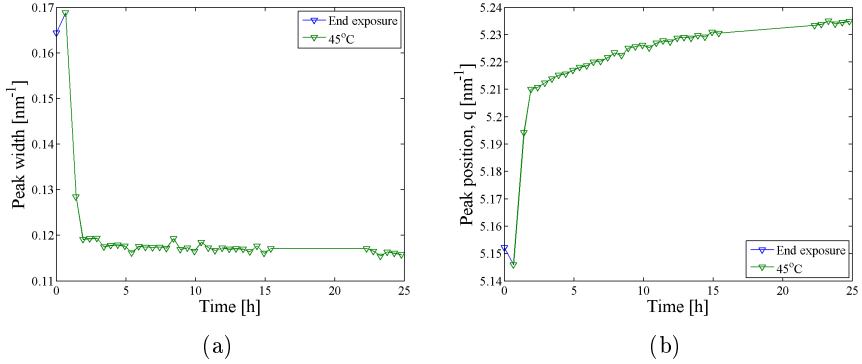


FIGURE A.9: (a) Width Δq and (b) Position q of the one-layer intercalation peak as functions of time. Humid LiFh sample after exposure to CO_2 . Flushing with N_2 at 45°C .

exposure). This is in line with a transition back to a mono-intercalated state.

With time, Δq remains stable, which indicates a stable intercalation state. A small shift towards higher q -values is observed for the intercalation peak. This shift is, as previously discussed, expected - independently of which substance occupies the interlayer. In Section 3.2.3 we observed characteristic differences in behavior of intercalated H_2O and CO_2 . As the temperature for the experiment presented here is 45°C , it is likely that the intercalated substance is H_2O .

Appendix B

Preliminary studies

This Appendix summarizes the findings of the preliminary experiments conducted for my Master's project [30] in the fall of 2011. The experiments were performed at MAX-lab in Lund, Sweden.

APPENDIX B PRELIMINARY STUDIES

B.1 Experimental results MAX-lab

B.1.1 Exposure to high pressure CO₂

Under exposure to high pressure CO₂ the clay samples display a decreased intensity of the peak corresponding to dehydrated clay. Simultaneously, another peak increases in intensity. It is due to scattering from particles with CO₂ incorporated into the guest layer, as described in Section 1.1.2. This intercalation corresponds to a change in basal d_{001} spacing of ~ 2.2 Å.

B.1.2 Choice of clay

Different clays show different intercalation dynamics. At MAX-lab, experiments were performed on NaFh and LiFh, two clays which only differ by the gallery cations Na⁺ and Li⁺. Both samples were exposed to 20 bar CO₂ at -30 °C.

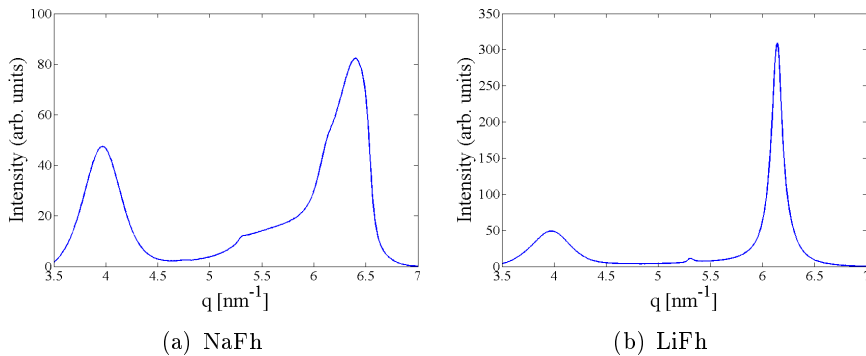


FIGURE B.1: Intensity curves of dehydrated clay samples before exposure to high pressure CO₂.

The initial measurement on NaFh, displayed in Figure B.1(a), shows trace of a monohydrated state at $q \sim 5.25 \text{ nm}^{-1}$. The intensity of this peak is sufficiently low to consider the sample dehydrated. The main contributions to scattered intensity in the initial scan come from the kapton window (q

B.1 EXPERIMENTAL RESULTS MAX-LAB

$\sim 4 \text{ nm}^{-1}$) and the peak corresponding to dehydrated clay ($q \sim 6.4 \text{ nm}^{-1}$ for NaFh and $q \sim 6.2 \text{ nm}^{-1}$ for LiFh). A ‘shoulder’ can be observed on the left side of the asymmetric 0 WL peak of NaFh. It indicates a partially ordered 0 WL state, and is possibly due to residual water in the sample.

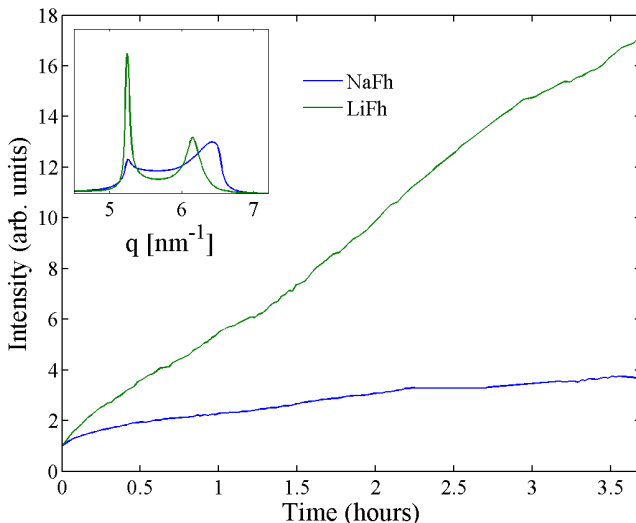


FIGURE B.2: Intensity of intercalation peak as function of time for NaFh and LiFh clay samples during exposure to high pressure CO_2 . The slopes indicate an order of magnitude faster intercalation in the LiFh sample than that of NaFh. The inset shows the intensity distributions for both samples after ~ 3.5 hours.

Figure B.2 shows how the intensity of the intercalation peak changes during exposure to CO_2 . The inset shows that the NaFh and LiFh samples partially undergo transitions to a state with interlayer distance corresponding to intercalation. The interlayer distances are $\sim 9.8 \text{ \AA}$ and $\sim 10 \text{ \AA}$ for dehydrated NaFh and LiFh, respectively. The intercalated states have similar basal spacing, namely $d_{001} \sim 12 \text{ \AA}$. This corresponds to intercalation causing changes in d_{001} -spacing of $\sim 2 \text{ \AA}$ and $\sim 1.8 \text{ \AA}$, for NaFh and LiFh.

The values differ somewhat from the change in basal d-spacing of 2.5 \AA reported by Hemmen et al [24]. However, the same group has also reported shifts of $\sim 0.3 \text{ \AA}$ within hydration states [4]. Considering the sim-

APPENDIX B PRELIMINARY STUDIES

ple method used to determine the peak positions, and that shifts have been observed, the deviation in unit cell expansion can be attributed to uncertainty and expected variations.

As can be seen in Figure B.2, the intercalation peak of the LiFh sample is much more pronounced after exposure for ~ 3.5 hours, than for NaFh. The slope of the intensity evolution reflects how the clay structure factor changes under exposure. By comparing slopes one can get an idea of the relative kinetics in the samples. The slope of LiFh exceeds that of NaFh with about a factor 10. Thus, it is clear that the intercalation process is much faster in LiFh than in NaFh.

B.1.3 Particle size

Based on the results from MAX-lab one can not conclude on whether the particle size influences the intercalation dynamics or not. Experiments with the the same conditions in term of temperature and pressure were performed on two LiFh samples, out of which one had been grinded. The fact that grain size does not appear to have a major effect on the dynamics of intercalation is in itself a useful result, as it yields one less parameter to take into account when evaluating results.

B.1.4 Temperature dependence

One of the future studies listed by E. G. Rolseth in [29] is mapping the dynamics of the intercalation process in terms of temperature and pressure. To get a preliminary indication of whether there is a significant temperature dependence, grinded LiFh was exposed to CO_2 at two different temperatures. The pressure was 20 bar. Intensity curves for the experiments are displayed in Figure B.3. Judging by the relative intensities of the peaks there seems to be a more complete transition for the sample kept at -30°C than the one kept at -15°C . The exposure time was $\sim 4\text{h}$ for both samples.

The time it takes for the intensity of the intercalation peak to exceed that of the dehydrated state is almost twice as long for the sample kept at a

B.1 EXPERIMENTAL RESULTS MAX-LAB

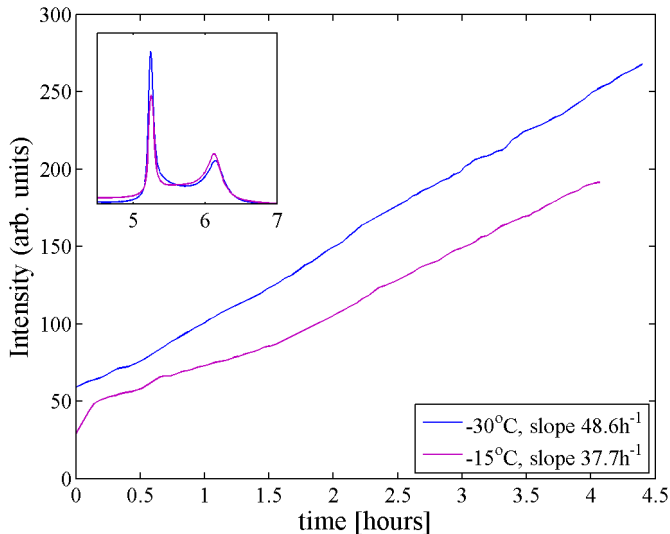


FIGURE B.3: Intensity of the CO₂ peak as function of time. The inset shows the intensity distributions after 4 hours of exposure. The slope gives an indication of the rate of intercalation. Both samples were exposed to CO₂ at 20 bar. Blue curve corresponds to -30 °C with slope 48.6 h⁻¹. Purple curve corresponds to exposure to CO₂ at -15 °C with slope 37.7 h⁻¹.

higher temperature. Slopes of linear fits to the peak intensity evolutions confirm this. The slopes are 48.6 h⁻¹ and 37.7 h⁻¹ for samples exposed to CO₂ at -30 °C and -15 °C, respectively. The intercalation seems to be faster for the colder sample, which is in accordance with the results reported by Rolseth [29]. Still, there is not an overwhelming difference in slopes. The faster process could possibly be credited to other factors, such as different amount of sample inside the test cell and resulting variations in packing of the samples. If the sample is more closely packed it would most likely result in slower intercalation.

The hypothesis before conducting the experiments was that the intercalation process would be faster for CO₂ in the liquid phase than in the gaseous phase. The results displayed in Figure B.3 are in agreement with this theory, all though not overwhelmingly convincing. As no measure-

APPENDIX B PRELIMINARY STUDIES

ments have been done for other temperatures close to the vaporization point, it is not possible to determine if the difference in intercalation rate is due to temperature differences, the phase of CO₂, or both.

B.1.5 Return to ambient conditions

After exposing a LiFh sample to high pressure CO₂ flushing with CO₂ at 1 bar was resumed while the temperature was increased to ambient level. Figure B.4(a) and B.4(b) show the resulting peak intensity distributions and evolutions with time.

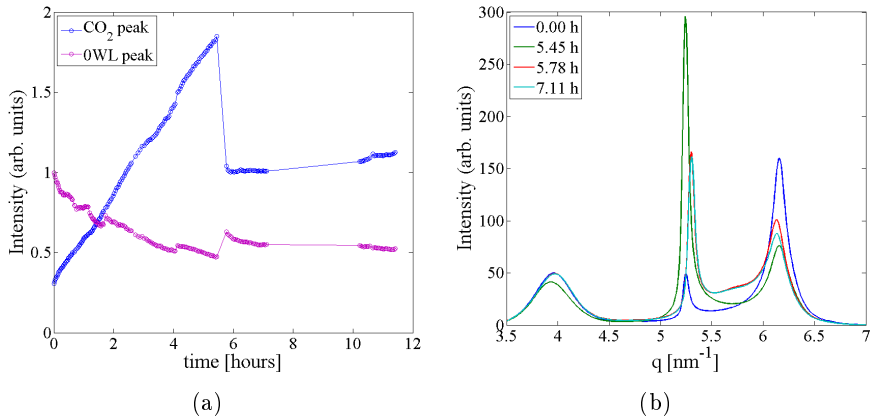


FIGURE B.4: Intensity curves for intercalation and return to ambient temperature after exposure. (a) Intensity as function of time for LiFh. After 5.5 hours conditions were changed from exposure to CO₂ at 20 bar, to flushing at 1 bar. Temperature was increased to 24 °C and eventually 30 °C. (b) One dimensional intensity distributions as function of q , for some measuring times. The intercalation peak does not drop below its initial level.

A significant drop in the intensity of the intercalation peak is observed when the conditions are changed. There is a small increase in the dehydrated peak intensity. The intensity distributions for measurements done while heating display a Hendricks-Teller peak between the peaks from CO₂ and 0 WL (Figure B.4(b)). This indicates a mixed intercalation state. It is

B.1 EXPERIMENTAL RESULTS MAX-LAB

the expected behavior when CO_2 diffuses out from the interlayer gap and the layer structure gradually goes back to its dehydrated configuration.

One would perhaps expect that this process would continue until the sample reached its initial, more or less dehydrated state. However, the figures show that the intensity of the intercalation peak does not fall to its initial value. The intensity also seems quite stable throughout the heating process. This result indicates that at least some CO_2 stays intercalated after exposure. If this is the case it would reinforce the position clays have as a candidate for CO_2 storage. Experiments where the deintercalation is studied over a longer time frame must be performed in order to get a better understanding of the dynamics of this process. The slight increase in intercalation peak intensity under heating is very interesting and unexpected behavior, considering that the intercalation process is observed to speed up for lower temperatures. More experiments will have to be performed in order to determine if this behavior is consistent. Also, the test cell should be flushed with N_2 , rather than CO_2 , to be confident that the sustained intensity is not due to the continuous supply of CO_2 .

Appendix C

Journal article draft

This is a draft for an article written in collaboration with PhD student Henrik Hemmen. It presents the main findings from my Master's thesis work regarding intercalation and retention of CO₂ in fluorohectorite clays.

The paper is still in preparation at the time of submission of this thesis. Before submitting to a journal, we plan to study the samples also with infrared spectroscopy, both to confirm the presence of CO₂ in the interlayer space with an element-specific technique, and to study the intercalation and retention in humid atmospheres.

Intercalation and Retention of Carbon Dioxide in Synthetic Fluorohectorite Clay at Near-Ambient Conditions

Henrik Hemmen,¹ Karin H. Rustenberg,¹ Tomás Plivelic,² and Jon Otto Fossum.^{1,3}

¹Department of Physics, Norwegian University of Science and Technology, Hoegskoleringen 5, N-7491 Trondheim, Norway

²MAX IV Laboratory, Lund University, SE-221 00 Lund, Sweden.

³Centre for Advanced Study (CAS) at the Norwegian Academy of Science and Letters, Drammensveien 78, N-0271 Oslo, Norway

ABSTRACT: We show using x-ray diffraction (*and I.R. spectroscopy*) that gaseous CO₂ intercalates into the interlayer space of the synthetic smectite clay fluorohectorite at conditions close to ambient. The rate of intercalation is found to be dependent on the interlayer cation, with about one order of magnitude increased rate in Li-fluorohectorite compared to Na-fluorohectorite. We further show that Li-fluorohectorite is able to retain CO₂ in the interlayer space at room temperature, which could have applications related to CO₂ capture, transport and storage. De-intercalation starts occurring at temperatures exceeding 30 °C.

1. Introduction

Interactions between CO₂ and clay have attracted interest in the scientific community in recent years, partly because geological structures are being investigated as storage sites for anthropogenic CO₂. The cap-rock formations that act as flow barriers and seals in this context are known to often contain high concentrations of clay minerals [1], and the long term integrity of these formations is a prerequisite to avoid losses to the atmosphere. [2-3]. Interactions between CO₂ and clay under reservoir conditions are however still not completely understood. In addition, several materials are under consideration for CO₂ capture or sequestration [ref to yang etal]. In this context, clay minerals have been prosed as a possible natural and cheap alternative to more complex materials [4].

Clay minerals are materials based on a two-dimensional stack of inorganic layers [5]. In some clays, non-equivalent substitutions of atoms generate a negative charge on the layer surface which is balanced by exchangeable cations. The cations allow the crystalline layers to stack together into clay particles consisting of up to several hundred layers. The subgroup of clays known as smectites has the ability to intercalate molecules into the interlayer space, thereby changing the repetition distance along the layer normal, a process which is known as swelling. Intercalation of water occurs naturally and has been extensively studied with a wide range of techniques, such as neutron [6-7] and x-ray

scattering [8-10], NMR spectroscopy [11-13], tracer experiments [14], and numerical modeling [11,15].

Experiments and simulations have shown that also CO₂ intercalates in some smectite clays, both in supercritical [4,16-22], and in gaseous/liquid form [4,16,22-27]. We have recently demonstrated that CO₂ is able to intercalate in Na-Fluorohectorite (NaFh) clay [26], at conditions close to ambient. These are not the conditions you find in the geological storage sites, but are relevant if you consider clay as a potential material for capture or sequestration of CO₂. In this context clay-containing material could have a distinct advantage, in that they are both cheap and ubiquitous, and that they can be used once and buried, saving the cost of regenerative energy, CO₂ compression, or subsurface injection [4].

Fluorohectorites are synthetic 2:1 silicates that have been used as a representative and clean model system of natural smectite clays. Synthetic clays have a homogenous charge distribution that leads to well-defined intercalation states, as opposed to natural clays which often display a coexistence of intercalation states. Synthetic clays also contain significantly fewer impurities (e.g. carbonates, (hydr)oxides, silica, and organic matter) than their natural counterparts [28].

In the present manuscript we have studied intercalation of CO₂ into Li-Fluorohectorite (LiFh) clay, which differs in structure from NaFh

only by the interlayer cation. The choice of this clay for further studies of CO₂ intercalation in fluorohectorites is due to an observed faster rate of intercalation compared to NaFh.

Intercalation experiments at different temperature and pressure conditions have been conducted. In order to investigate the potential of fluorohectorite clays for CO₂ sequestration, we have also studied de-intercalation of CO₂ when returning the sample to ambient conditions.

II. Experimental Methods

X-ray diffraction measurements were primarily performed on a Bruker NanoSTAR x-ray scattering instrument, attached to a Xenox stationary electron impact source with a copper anode, producing K_α-radiation. The scattered intensity was recorded by a two-dimensional multiwire grid Xe gas detector. The beam diameter of the setup is 400 μm and the detectable range of momentum transfer q was $(2.5 < q < 7.5) \text{ nm}^{-1}$. We also performed measurements at the I911-4 beamline at MAX-lab in Lund, Sweden, using a marCCD detector and 0.91 Å wavelength.

The LiFh sample was mounted in a custom made sample holder [26] which allowed control of temperature in the range -30°C to 45°C and pressure from ambient to 20 bar. To allow x-rays to pass through the sample, the cell had Kapton windows on both sides of the sample volume. Internal channels connected gas from valves on the surface of the cell to the sample volume, and the gas pressure was controlled by standard reduction valves.

In both x-ray setups, two-dimensional diffractograms were recorded, and then integrated over all azimuthal angles to produce plots of intensity versus scattering vector. Data reduction consisted in subtracting a background, and normalizing the intensity profiles to the peak produced by the Kapton windows (see Hemmen et al. [26] for details). The intensity and position of the intercalation peaks were found by fitting the peaks to Pseudo-Voigt profiles [29-30].

The LiFh clay used in the experiments was purchased from Corning Inc (nominal chemical formula: Li_{1.2}[(Mg_{4.8}Li_{1.2})Si₈O₂₀F₄] per unit cell [31]). At ambient conditions, the clay is in a monohydrated state. In order to dehydrate it, samples were heated in an oven at 170°C for

more than three hours. To remove residual humidity from the cell after loading the clay, and to ensure that the sample remained dry, the cell was flushed with N₂-gas. An x-ray scan was also recorded at ambient temperature and pressure while flushing N₂ to confirm that the sample remained dehydrated before starting intercalation. The sample was subsequently cooled to the target temperature before the gas was changed to CO₂. The gas outlet of the cell was closed and the pressure increased.

The CO₂ used for experiments had a purity of 99.999% (Yara Praxair, grade 5). The N₂ gas had purity 99.9999% (Yara Praxair, grade 6). To obtain a satisfactory signal-to-noise ratio, acquisition times varied from 30 to 60 minutes, depending on CO₂ pressure (i.e. its x-ray absorption).

(Details of IR-measurements to be inserted here)

III. Results

A. CO₂ Intercalation

X-ray measurements of CO₂-intercalation in NaFh and LiFh under the same conditions show about one order of magnitude faster rate of intercalation in LiFh compared to NaFh, see Figure 1. The rate of CO₂ intercalation in LiFh is however still orders of magnitude slower than the intercalation of water at ambient pressure and temperature [32].

That the CO₂ intercalation is dependent on the type of interlayer cation is not unexpected. In studies of hydration, the cations have been found to determine both the stable states at varying relative humidity [15,33-34], and whether clays exfoliate in aqueous dispersion [35]. Fripiat et al. [24] argued that the CO₂ molecules' access to the interlayer space of montmorillonite is dependent on the size of the interlayer cation. However, that the time scale for intercalation shows such strong dependence on the type of cation has to our knowledge never been shown. Giesting et al. [27] studied the differing CO₂-intercalation behaviour of K- and Ca-montmorillonite, and also performed repeated measurements at the same conditions, but reported no strong dependence of dynamics on the cations.

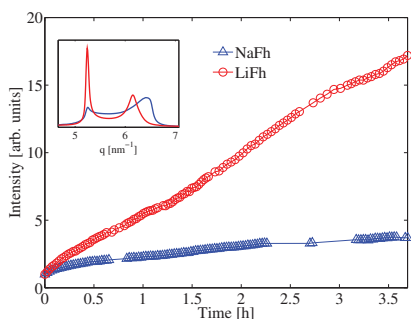


Figure 1 The intensity of the CO₂ intercalation peak as function of time for NaFh and LiFh (-30°C and 20bar), demonstrating the faster dynamics in LiFh. The inset shows the $I(q)$ -profiles for both samples after 3.5 h (left: intercalation peak; right: peak from clay that is still not intercalated).

Our previous study on NaFh [26] showed an increased intercalation rate with higher pressure, which we have reproduced for LiFh as well, see Figure 2. We have also observed intercalation at various temperatures (constant pressure: 20 bar), but the dependency between intercalation rate and temperature is still not clear to us (see inset Figure 2). In any case the rate seems to be less dependent on temperature than pressure.

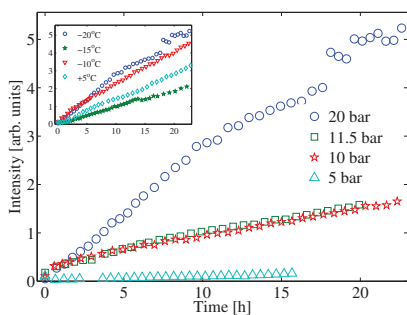


Figure 2 The intensity of the CO₂ intercalation peak in LiFh as a function of time for different pressures (constant temperature -20°C). The intercalation rate is seen to increase with higher pressure. The inset shows intercalation at 20 bars for various temperatures.

B. Retention at ambient conditions.

We have used the same setup to also test at what temperature the CO₂ leaves the clay. After a LiFh sample had been exposed to CO₂ for sufficiently long time to reach a stable maximum intensity of the CO₂ intercalation peak, we started flushing with N₂ and reheated the cell in steps of 5 °C. A plot of peak intensity vs. time for a range of temperatures is shown in Figure 3. We see that the peak intensity remains stable for temperatures up to 32 °C, where it starts to decay.

Once the intensity decrease starts, it continues until the contribution to scattered intensity from clay with intercalated CO₂ is negligible. Simultaneously, the peak corresponding to dehydrated LiFh reappears (not shown). The reason for the small increases in intensity at temperatures below 32 °C is not clear, but we assume it is due to either changes in x-ray absorption or reorganization of intercalated CO₂.

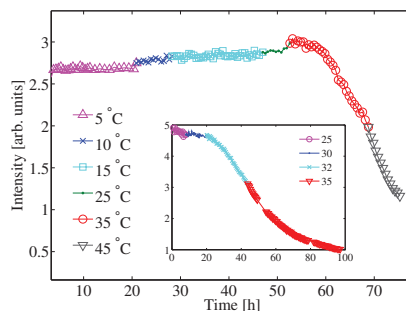


Figure 3. Intensity of the CO₂ intercalation peak during stepwise heating of a LiFh sample. The inset shows a repetition of the experiment with smaller jumps in temperature. The intensity starts decreasing for temperatures above 30 °C, indicating that CO₂ escapes the interlayer.

Figure 4 shows the behavior of the CO₂-intercalation peak in comparison with a monohydrated sample when both were heated to 45 °C in dry N₂ atmosphere. It is evident from the figure that water is retained in the LiFh structure for temperatures well beyond where deintercalation of CO₂ is observed. This behavior is as expected, since fluorohectorite has been shown to remain in the monohydrated state up

to 60 °C [8] (the reference is to a study of NaFh, but the dehydration temperature of LiFh is similar). In this case, both samples were heated directly from -20 °C to 45 °C, in order to minimize any effects of hysteresis.

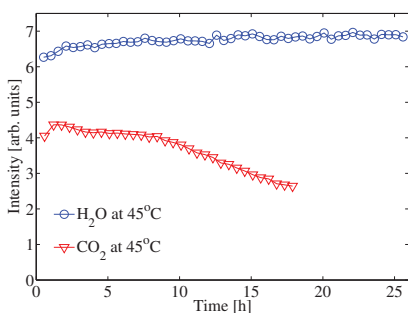


Figure 4. Intensity of intercalation peaks as a function of time at 45 °C, for a humid LiFh sample and one which has been exposed to CO₂. The intensity of the CO₂-intercalation peak starts decreasing shortly after temperature was elevated due to de-intercalation of CO₂ from the clay structure. The humid sample remains in the 1WL intercalation state, at the same conditions.

If the samples were intercalated by the same substance, one would have expected similar behavior. The observed behavior is therefore another confirmation that traces of water in the gas or cell is not the cause of intercalation. This supports our previously published observations [26] that CO₂ can penetrate the interlayer and cause expansion of fluorohectorite clays.

C. Infrared Spectroscopy.

(Not performed yet)

IV. Conclusion

We have shown that CO₂ is able to intercalate in LiFh for a range of conditions in terms of pressure and temperature. By intercalating CO₂ in NaFh and LiFh at the same conditions, we also demonstrated that the rate of intercalation is dependent on the type of interlayer cation. The rate was found to be about one order of magnitude faster with Li as counterion compared to Na.

After intercalating CO₂ in a LiFh sample, we performed in situ observations while increasing the temperature and releasing the pressure. The results showed that CO₂ is retained in LiFh at room temperature and ambient pressure.¹ The CO₂ starts to exit the interlayers only if temperature is increased to above 30 °C. Since LiFh remains in the monohydrated state up to ≈ 60 °C, we were able to confirm that residual water is not responsible by comparing the behavior of hydrated and CO₂-intercalated LiFh at 45 °C.

We believe that our findings, concerning both intercalation and de-intercalation, could have relevance for CO₂ storage, capture and transport.

V. Acknowledgements

This work has been supported by the Norwegian Research Council (grant no. 200041). The authors thank Ole Tore Buset, Pawel Sobas, and Henrik Mauroy for experimental assistance. MAX-lab is acknowledged for the beamtime provided under proposal XXX

¹ So far this is done only in dry atmosphere. IR-measurements are planned to confirm if it is also the case in humid atmospheres.

VI. References

- [1] D. R. Cole, A. A. Chialvo, G. Rother, L. Vlcek, and P. T. Cummings, *Philos. Mag.* **90**, 2339 (2010).
- [2] A. Hildenbrand, S. Schlomer, and B. M. Krooss, *Geofluids* **2**, 3 (2002).
- [3] J. Wollenweber, S. Alles, A. Busch, B. M. Krooss, H. Stanjek, and R. Littke, *Int J Greenh Gas Con* **4**, 231 (2010).
- [4] R. T. Cygan, V. N. Romanov, and E. M. Myshakin, Sandia National Laboratories Report No. Techincal report SAND2010-7217, 2010.
- [5] P. Boulet, H. C. Greenwell, S. Stackhouse, and P. V. Coveney, *J Mol Struc-Theochem* **762**, 33 (2006).
- [6] N. Malikova, A. Cadene, E. Dubois, V. Marry, S. Durand-Vidal, P. Turq, J. Breu, S. Longeville, and J. M. Zanotti, *J Phys Chem C* **111**, 17603 (2007).
- [7] M. Jimenez-Ruiz, E. Ferrage, A. Delville, and L. J. Michot, *J Phys Chem A* **116**, 2379 (2012).
- [8] G. J. da Silva, J. O. Fossum, E. DiMasi, and K. J. Maloy, *Physical Review B* **67**, 094114 (2003).
- [9] G. J. da Silva, J. O. Fossum, E. DiMasi, K. J. Maloy, and S. B. Lutnaes, *Phys. Rev. E* **66**, 011303 (2002).
- [10] E. Ferrage, B. A. Sakharov, L. J. Michot, A. Delville, A. Bauer, B. Lanson, S. Grangeon, G. Frapper, M. Jimenez-Ruiz, and G. J. Cuello, *J Phys Chem C* **115**, 1867 (2011).
- [11] P. Porion, L. J. Michot, A. M. Faugere, and A. Delville, *J Phys Chem C* **111**, 5441 (2007).
- [12] R. P. Tenorio, L. R. Alme, M. Engelsberg, J. O. Fossum, and F. Hallwass, *J Phys Chem C* **112**, 575 (2008).
- [13] R. P. Tenorio, M. Engelsberg, J. O. Fossum, and G. J. da Silva, *Langmuir* **26**, 9703 (2010).
- [14] M. Jansson and T. E. Eriksen, *J Contam Hydrol* **68**, 183 (2004).
- [15] T. J. Tambach, E. J. M. Hensen, and B. Smit, *J. Phys. Chem. B* **108**, 7586 (2004).
- [16] A. Botan, B. Rotenberg, V. Marry, P. Turq, and B. Noettinger, *J. Phys. Chem. C* **114**, 14962 (2010).
- [17] N. Yang and X. Yang, *Mol. Simul.* **37**, 1063 (2011).
- [18] J. S. Loring, H. T. Schaefer, R. V. F. Turcu, C. J. Thompson, Q. R. S. Miller, P. F. Martin, J. Z. Hu, D. W. Hoyt, O. Qafoku, E. S. Ilton, A. R. Felmy, and K. M. Rosso, *Langmuir* **28**, 7125 (2012).
- [19] H. T. Schaefer, E. S. Ilton, O. Qafoku, P. F. Martin, A. R. Felmy, and K. M. Rosso, *Int. J. Greenhouse Gas Control* **6**, 220 (2012).
- [20] A. Busch, S. Alles, Y. Gensterblum, D. Prinz, D. N. Dewhurst, M. D. Raven, H. Stanjek, and B. M. Krooss, *Int. J. Greenhouse Gas Control* **2**, 297 (2008).
- [21] E. S. Ilton, H. T. Schaefer, O. Qafoku, K. M. Rosso, and A. R. Felmy, *Environ. Sci. Technol.* **46**, 4241 (2012).
- [22] P. Giesting, S. Guggenheim, A. F. Koster van Groos, and A. Busch, *Int. J. Greenhouse Gas Control* **8**, 73 (2012).
- [23] J. Thomas and B. F. Bohor, *Clays Clay Miner.* **16**, 83 (1968).
- [24] J. J. Fripiat, M. I. Cruz, B. F. Bohor, and J. Thomas, *Clays Clay Miner.* **22**, 23 (1974).
- [25] P. Sozzani, S. Bracco, A. Comotti, M. Mauri, R. Simonutti, and P. Valsesia, *Chem Commun*, 1921 (2006).
- [26] H. Hemmen, E. G. Rolseth, D. M. Fonseca, E. L. Hansen, J. O. Fossum, and T. S. Pivelic, *Langmuir* **28**, 1678 (2012).
- [27] P. Giesting, S. Guggenheim, A. F. Koster van Groos, and A. Busch, *Environ. Sci. Technol.* **46**, 5623 (2012).
- [28] K. A. Carrado, A. Decarreau, S. Petit, F. Bergaya, and G. Lagaly, in *Handbook of Clay Science*, edited by F. Bergaya, B. K. G. Theng, and G. Lagaly (Elsevier, 2006), pp. 115.
- [29] G. K. Wertheim, M. A. Butler, K. W. West, and D. N. Buchanan, *Rev. Sci. Instrum.* **45**, 1369 (1974).
- [30] D. E. Cox, B. H. Toby, and M. M. Eddy, *Aust. J. Phys.* **41**, 117 (1988).
- [31] P. D. Kaviratna, T. J. Pinnavaia, and P. A. Schroeder, *J. Phys. Chem. Solids* **57**, 1897 (1996).
- [32] H. Hemmen, L. R. Alme, J. O. Fossum, and Y. Meheust, *Phys. Rev. E* **82**, 036315 (2010).
- [33] K. Tamura, H. Yamada, and H. Nakazawa, *Clays Clay Miner.* **48**, 400 (2000).
- [34] E. Ferrage, B. Lanson, B. A. Sakharov, and V. A. Drits, *Am. Mineral.* **90**, 1358 (2005).
- [35] N. T. Skipper, M. V. Smalley, G. D. Williams, A. K. Soper, and C. H. Thompson, *J. Phys. Chem.* **99**, 14201 (1995).

Appendix D

Poster Lofoten

This poster was presented by doctoral student Henrik Hemmen at the *International Workshop on Soft Matter Physics and Complex Flows* in Svolvær, Lofoten, Norway, May 2012.

It presents highlights from the research carried out by the Complex group at NTNU, regarding to CO₂ intercalation in fluorohectorite clays. My contribution to the poster has been experimental results from MAX-lab, related to the effect of the exchange cation on intercalation rate. Furthermore, I have contributed with results from heating experiments performed at NTNU on LiFh clay intercalated with CO₂ and water.

Carbon dioxide intercalation in a clay at near-ambient conditions

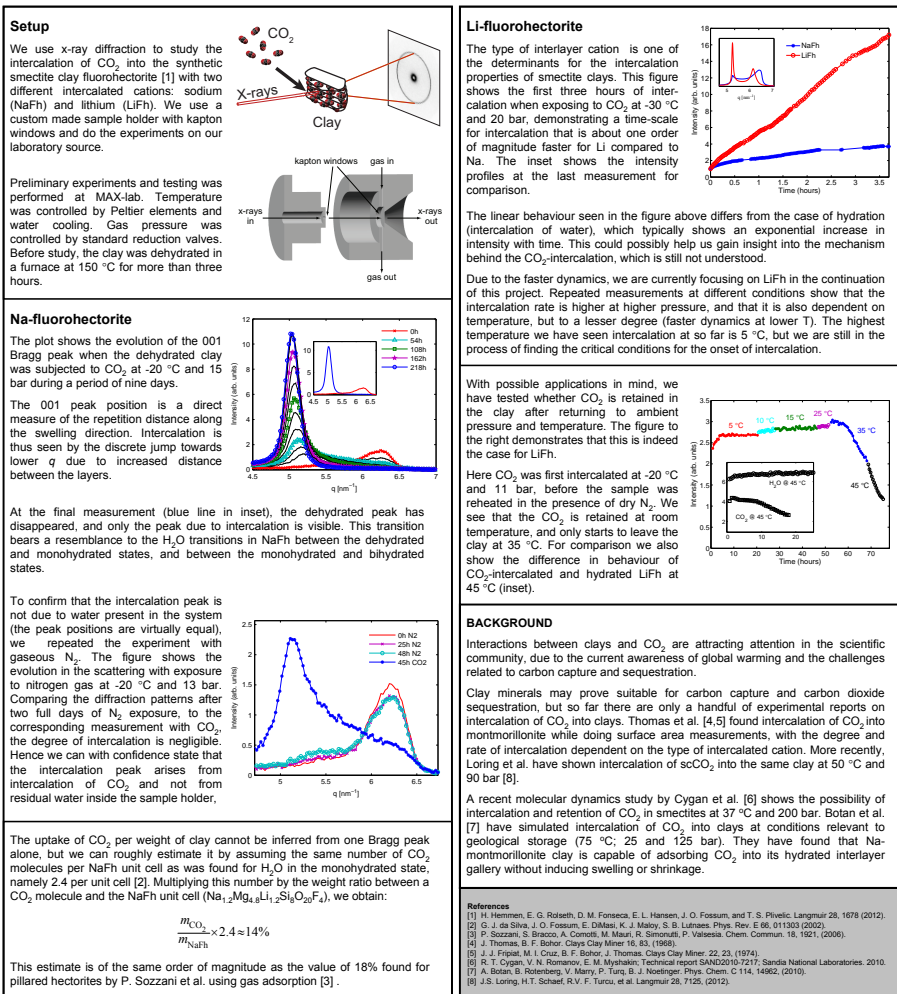
Henrik Hemmen,^{*†} Erlend G. Rolseth,[†] Karin Rustenberg,[†] Davi M. Fonseca,[‡] Elisabeth L. Hansen,[†]
Jon Otto Fossum,^{*†,§} and Tomás S. Plivelic,^{||}

[†]Department of Physics, Norwegian University of Science and Technology, Trondheim, Norway.

[‡]Department of Cancer Research and Molecular Medicine, Norwegian University of Science and Technology, Trondheim, Norway

[§]Centre for Advanced Study (CAS) at the Norwegian Academy of Science and Letters, Norway.

^{||}MAX IV Laboratory, Lund University, Lund, Sweden.



Appendix E

COMPLEX-CAS kick-off proceedings

The following paper is submitted to the Proceedings of the COMPLEX-CAS kick-off meeting. The meeting marked the beginning of the Complex national network stay at the Centre for Advanced Study (CAS) at the Norwegian Academy of Science and Letters for the academic year 2011/2012.

The paper is a short summary of the group's ongoing research related to CO₂ capture in clays at the time of the meeting. My contribution to this publication was experimental results from experiments performed at MAX-lab in Lund, Sweden, regarding the effect of the interlayer cation on intercalation rate.



@



2011-12

Center for Advanced Study
at Norwegian University of Science and Technology



CO₂ capture in clays

Henrik Hemmen, Erlend G. Rolseth, Davi. M. Fonseca, *

Elisabeth L. Hansen, Karin Rustenberg,

Jon Otto Fossum[†]

Dept. of Physics, NTNU, Trondheim, Norway

Tomás S. Plivelic

MAX IV Laboratory, Lund University, Lund, Sweden


Henrik Mauroy

Institute for Energy Technology (IFE), Kjeller, Norway


Present addresses:

* *Dept. of Cancer Research and Molecular Medicine, NTNU, Trondheim, Norway*

† *Center for Advanced Study, Norwegian Academy of Science and Letters, Oslo, Norway*




@



2011-12

Centre for Advanced Study
at Heriot-Watt University of Edinburgh, UK



Motivation

–Naturally occurring clay minerals provide a distinctive material for carbon capture and carbon dioxide sequestration.

R. T. Cygan et al., Natural materials for carbon capture. Technical report: Sandia National Laboratories 2010.

–Monte Carlo and molecular dynamics simulations (...) show that the hydrated clay system is capable of adsorbing CO₂ molecules.

A. Botan et al., Carbon Dioxide in Montmorillonite Clay Hydrates: Thermodynamics, Structure, and Transport from Molecular Simulation. Phys. Chem. C 2010.

–The evidence presented in this study clearly shows that CO₂ at about -70 °C penetrates (intercalates) the smectite structure to a degree dependent upon the nature of the replaceable interlayer cation.

J. J. Fripiat et al., Interlamellar adsorption of carbon dioxide by smectites. Clays Clay Miner. 1974.

Experiment

We study intercalation of CO_2 into fluorohectorite. Our starting point is Na-fluorohectorite (NaFh). Later we will use fluorohectorite with other intercalated cations (e.g. Li), as well as different clays.

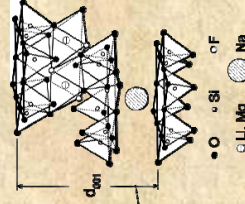
NaFh is a synthetic smectite clay. We have previously studied its properties related to intercalation of water (hydration).



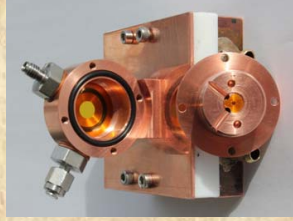
CO_2




Fluorohectorite clay




NaFh unit cell




Sample cell



@

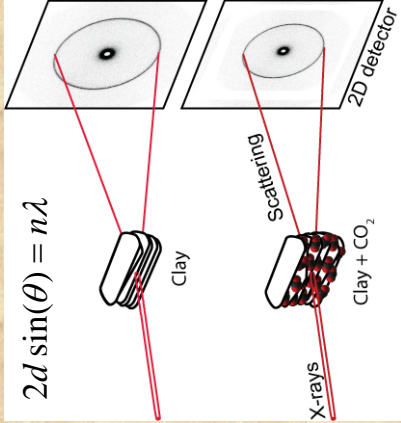


2011-12
Centre for Advanced Study
with Nanyang University of Singapore

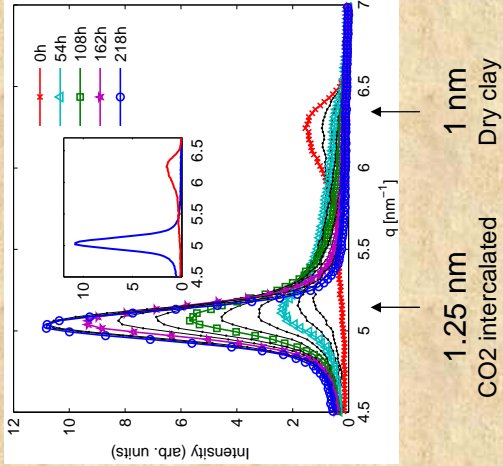


Results

With x-ray diffraction we get the average interlayer distance d from Bragg's law.

$$2d \sin(\theta) = n\lambda$$


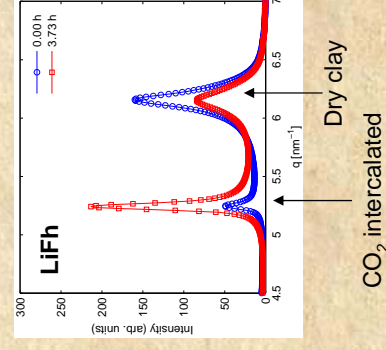
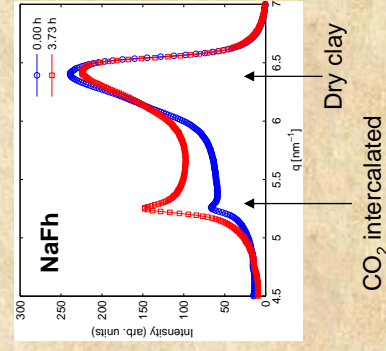
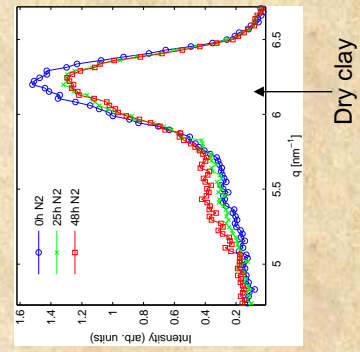
We observe CO₂ intercalation in NaFh at low temperatures and moderate pressures.
Here: -20 °C ; 15 bar




Results


To rule out intercalation of residual water in the cell, we repeated with Nitrogen gas. No intercalation with N_2 means the intercalated substance is CO_2 .

Preliminary experiments with LiFh indicate that the intercalation dynamics is orders of magnitude faster with Li as the intercalated cation, compared to Na. We will investigate this phenomenon further, possibly using other cations as well.





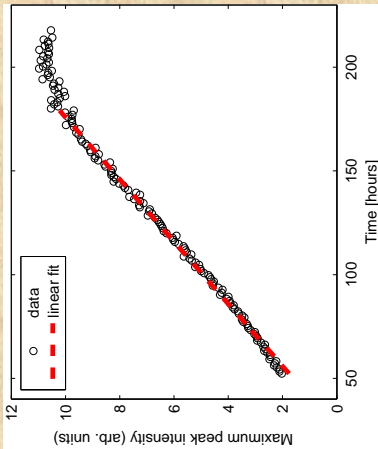
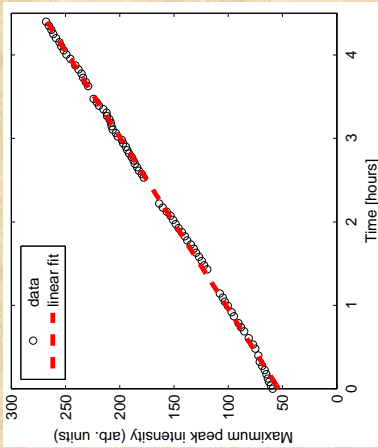
@



Results

With NaFh we observe a linear growth in peak intensity for >100h. The mechanisms behind is yet to be understood.

The linear behaviour is reproduced with LiFh. Note also the higher rate of intercalation.



Conclusions

- We have shown intercalation of CO_2 into fluorohectorite clay, at conditions close to ambient.
- With NaFh, the time scale of CO_2 intercalation (~ 1 week) is orders of magnitude slower than for water (minutes). The type of intercalated cation seems to be important in this respect, since we find faster intercalation dynamics with LiFh.
- We observe a linear growth in intercalation peak intensity as a function of time.
- Further experiments with LiFh are underway, as well as extending the study to other and natural clays.
- The first results from the project is already published in Hemmen et al. *Langmuir* 28 (3), pp 1678–1682, 2012.

List of Figures

1.1	Layer structure of 1:1 and 2:1 clays	2
1.2	Unit cell of 2:1 layered silicate clay	3
1.3	Phase diagram of CO ₂	7
1.4	X-ray scattering by an electron	10
1.5	Scattering by an atom, a molecule and a crystal lattice . . .	13
1.6	X-ray spectrum of stationary source	20
1.7	Third generation synchrotron X-ray source	22
1.8	Fundamental vibration-rotation bands of CO ₂	28
1.9	Infrared spectrum of bending mode H ₂ O	29
1.10	Fourier Transform infrared spectrometer schematics	30
2.1	The test cell	33
2.2	Sample cell mounted on Peltier and heat sink	34
2.3	Experimental setup	35
3.1	Diffraction pattern and one-dimensional representation . . .	40
3.2	Background subtraction	42
3.3	Intercalation - Scattering distribution and intensity	44
3.4	Peak width Δq , position and basal spacing - Intercalation .	47
3.5	Intercalation rate comparison - Pressure	50
3.6	Intercalation rate comparison - Temperature	51
3.7	Two-CO ₂ -layer peak	53
3.8	Stepwise increasing temperatures - CO ₂ -intercalated samples	56
3.9	Intensity distribution deintercalation	57
3.10	Intensity evolution deintercalation	58
3.11	Peak width and position - Deintercalation	60

LIST OF FIGURES

3.12	Deintercalation increasing temperatures - CO ₂ and humid . . .	62
3.13	Humidity test, deintercalation at 45°C	63
3.14	Basal spacings of humid and CO ₂ -LiFh at 45 °C	65
3.15	Intensity and evolution - Mixed intercalation	68
3.16	Peak position and width - CO ₂ intercalation mixed clay . . .	69
3.17	Intensity and evolution - Deintercalation mixed clay	72
3.18	Natural hectorite	73
3.19	IR spectra - Background and LiFh film	76
3.20	IR ratio spectrum LiFh film	77
A.1	Intercalation - Intensity of CO ₂ peak as function of time. . .	86
A.2	Peak widths intercalation	88
A.3	Peak positions intercalation	89
A.4	Basal spacing - Intercalation	90
A.5	Deintercalation at increasing temperatures, CO ₂ and humid	91
A.6	Widths and positions - Deintercalation increasing temperature	92
A.7	Intensity, widths and position - Deintercalation at 45°C . .	94
A.8	Humidity test, deintercalation at 45 °C - Width and position	95
A.9	Peak position and width - Deintercalation mixed state . . .	96
B.1	Dehydrated NaFh and LiFh samples	98
B.2	Intensity evolutions of NaFh and LiFh	99
B.3	Temperature comparison; -30 °C and -15 °C	101
B.4	Intercalation and return to ambient temperature	102

Bibliography

- [1] P. Boulet, H. C. Greenwell, S. Stackhouse, and P. V. Coveney. Recent advances in understanding the structure and reactivity of clays using electronic structure calculations. *Journal of Molecular Structure-Theochem*, 762, 2006.
- [2] N. Malikova, A. Cadene, E. Dubois, V. Marry, S. Durand-Vidal, P. Turq, J. Breu, S. Longeville, and J. M. Zanotti. Water diffusion in a synthetic hectorite clay studied by quasi-elastic neutron scattering. *Journal of Physical Chemistry C*, 111, 2007.
- [3] M. Jimenéz-Ruiz, E. Ferrage, A. Delville, and L.J. Michot. Anisotropy on the collective dynamics of water confined in swelling clay minerals. *The Journal of Physical Chemistry A*, 116(10), 2012.
- [4] H. Hemmen, L. R. Alme, J. O. Fossum, and Y. Meheust. X-ray studies of intercalated water absorption and mesoporous water transport in a weakly hydrated clay. *Physical Review E*, 82, 2010.
- [5] G. J. da Silva, J.O. Fossum, E. DiMasi, K. J. Måløy, and S.B. Lutnæs. Synchrotron X-ray scattering studies of water intercalation in a layered synthetic silicate. *Physical Review E*, 66, 2002.
- [6] G. J. da Silva and Jon Otto Fossum, E. DiMasi, and Knut Jørden Måløy. Hydration transitions in a nanolayered synthetic silicate: A synchrotron x-ray scattering study. *Physical review B*, 67, 2003.
- [7] E. Ferrage, B. Lanson, B. A. Sakharov, and V. A. Drits. Investigation of smectite hydration properties by modeling experimental X-

BIBLIOGRAPHY

- ray diffraction patterns: Part I. montmorillonite hydration properties. *American Mineralogist*, 90(8-9), 2005.
- [8] P. Porion. Structural and dynamical properties of the water molecules confined in dense clay sediments: A study combining h-2 nmr spectroscopy and multiscale numerical modeling. *Journal of Physical Chemistry C*, 111, 2007.
- [9] R. P. Tenório, L. R. Alme, M. Engelsberg, J. O. Fossum, and F. Hallwass. Geometry and dynamics of intercalated water in na-fluorhectorite clay hydrates. *Journal of Physical Chemistry C*, 112, 2008.
- [10] M. Jansson and T. E. Eriksen. In situ anion diffusion experiments using radiotracers. *Journal of Contaminant Hydrology*, 68, 2004.
- [11] T. J. Tambach, E. J. M. Hensen, and J. M. Smit. Molecular simulations of swelling clay minerals. *Journal of Physical Chemistry B*, 108, 2004.
- [12] T. J. Tambach, P. G. Bolnius, E. J. M. Hensen, and J. M. Smit. Hysteresis in clay swelling induced by hydrogen bonding: Accurate prediction of swelling states. *Langmuir*, 2006.
- [13] E. Ferrage, B. A. Sakharov, L. J. Michot, A. Delville, A. Bauer, B. Lanson, S. Grangeon, G. Frapper, M. Jimenez-Ruiz, and G. J. Cuello. Hydration properties and interlayer organization of water and ions in synthetic Na-smectite with tetrahedral layer charge. part II. toward a precise coupling between molecular simulations and diffraction data. *Journal of Physical Chemistry C*, 115, 2011.
- [14] M. Alexandre and P. Dubois. Polymer-layered silicate nanocomposites: preparation, properties and uses of a new class of materials. *Materials Science & Engineering R-Reports*, 28, 2000.
- [15] D. R. Cole, A. A. Chialvo, G. Rother, L. Vlcek, and P. T. Cummings. Supercritical fluid behavior at nanoscale interfaces: Implications for CO₂ sequestration in geologic formations. *Philosophical Magazine*, 90, 2010.

BIBLIOGRAPHY

- [16] A. Hildenbrand, S. Schlömer, and B. M. Krooss. Gas breakthrough experiments on fine-grained sedimentary rocks. *Geofluids*, 2(1), 2002.
- [17] J. Wollenweber, S. Alles, A. Busch, B. M. Krooss, H. Stanjek, and R. Littke. Experimental investigation of the CO₂ sealing efficiency of caprocks. *International Journal of Greenhouse Gas Control*, 4, 2010.
- [18] John S. Loring, Herbert T. Schaef, Romulus V. F. Turcu, Christopher J. Thompson, Quin R.S. Miller, Paul F. Martin, and Jianzhi Hu. In situ molecular spectroscopic evidence for CO₂ intercalation into montmorillonite in supercritical carbon dioxide. *Langmuir*, 2012.
- [19] H. T. Schaef, E. S. Ilton, O. Qafoku, P. F. Martin, A.R. Felmy, and K.M. Rosso. In situ xrd study of Ca²⁺ saturated montmorillonite (STx-1) exposed to anhydrous and wet supercritical carbon dioxide. *International Journal of Greenhouse Gas Control*, 6(0), 2012.
- [20] A. Busch, S. Alles, Y. Gensterblum, D. Prinz, D. N. Dewhurst, M. D. Raven, H. Stanjek, and B. M. Krooss. Carbon dioxide storage potential of shales. *International Journal of Greenhouse Gas Control*, 2, 2008.
- [21] E. S. Ilton, H. T. Schaef, O. Qafoku, K. M. Rosso, and A. R. Felmy. In situ x-ray diffraction study of Na⁺ saturated montmorillonite exposed to variably wet super critical CO₂. *Environmental Science & Technology*, 46, 2012.
- [22] Paul Giesting, Stephen Guggenheim, Augustus Koster van Groos, and Andreas Busch. Carbon dioxide intercalation in Na- and Ca-exchanged montmorillonite. *Geophysical Research Abstracts*, 2011.
- [23] Paul Giesting, Stephen Guggenheim, August F. Koster van Groos, and Andreas Busch. Interaction of carbon dioxide with na-exchanged montmorillonite at pressures to 640 bars: Implications for CO₂ sequestration. *International Journal of Greenhouse Gas Control*, 8, 2012.
- [24] H. Hemmen, E. G. Rolseth, D. M. Fonseca, E. L. Hansen, J. O. Fossum, and T. S. Plivelic. X-ray studies of carbon dioxide intercalation in Na-fluorohectorite clay at near-ambient conditions. *Langmuir*, 28, 2012.

BIBLIOGRAPHY

- [25] J. J. Fripiat, B.F. Bohor M. I. Cruz, and Jr. J. Thomas. Interlamellar adsorption of carbon dioxide by smectites. *Clays and Clay Minerals*, 22, 1973.
- [26] Paul Giesting, Stephen Guggenheim, August F. Koster van Groos, and Andreas Busch. X-ray diffraction study of K- and Ca-exchanged montmorillonites in CO₂ atmospheres. *Environmental Science & Technology*, 46, 2012.
- [27] J. Thomas and B. F. Bohor. Surface area of montmorillonite from dynamic sorption of nitrogen and carbon dioxide. *Clays and Clay Minerals*, 16, 1968.
- [28] P. Sozzani, S. Bracco, A. Comotti, M. Mauri, R. Simonutti, and P. Valsesia. Nanoporosity of an organo-clay shown by hyperpolarized xenon and 2d NMR spectroscopy. *Chemical Communications*, 18, 2006.
- [29] E. G. Rolseth. Carbon dioxide intercalation in sodium fluorohectorite clay. Master's thesis, NTNU, Norwegian University of Science and Technology, 2011.
- [30] Karin Rustenberg. Preparations for x-ray studies of capture, storage and release of CO₂ in clays. Master's thesis, NTNU, Norwegian University of Science and Technology, 2011.
- [31] R. M. Tenório, M. Engelsberg, J. O. Fossum, and G.J da Silva. Intercalated water in synthetic fluorhectorite clay. *Langmuir*, 26, 2010.
- [32] J. O. Fossum. Physical phenomena in clays. *Physica A*, 270, 1999.
- [33] F. Bergaya, B. Theng, and G. Lagaly. *Handbook of Clay Science*. Elsevier, 2006.
- [34] S. A. Solin. Clays and intercalation compounds: Properties and physical phenomena. *Annual Review of Materials Science*, 27, 1997.
- [35] T.N. Balnton, D. Majumdar, and S. M. Melpolder. Microstructure of clay-polymer composites. *Advances in X-ray Analysis*, 42, 2000.
- [36] J. Budjak. Effect of the layer charge of clay minerals on optical properties of organic dyes. a review. *Applied Clay Science*, 34, 2006.

BIBLIOGRAPHY

- [37] R. T. Cygan, V. N. Romanov, and E. M. Myshakin. Natural materials for carbon capture. Technical report, Sandia National Laboratories, 2010.
- [38] P. D. Kaviratna, . J. Pinnavaia, and P. A. Schroeder. Dielectric properties of smectite clays. *Journal of Physics and Chemistry of Solids*, 57(12), 1996.
- [39] Josef Brey, Wolfgang Seidl, Alexander J. Stoll, Kurt G. Lange, and Thomas U. Probst. Charge homogeneity in synthetic fluorohectorite. *Chemistry of Materials*, 13, 2001.
- [40] S. Yang, W. Lewis, M. Suyetin, E. Bichoutskaia, J. E. Parker, C. C. Tang, D. R. Allan, P. J. Rizkallah, P. Hubberstey, N. R. Champness, K. Mark Thomas, A. J. Blake, and M. Schroeder. A partially interpenetrated metal-organic framework for selective hysteretic sorption of carbon dioxide. *Nature Materials*, 1, 2012.
- [41] Inc. Universal Industrial Gases. Nitrogen (N_2) properties, uses and applications.
<http://www.uigi.com/nitrogen.html>. retrieved 13.05.2012.
- [42] J. Als-Nielsen and D. McMorrow. *Elements of modern X-ray physics*. Wiley, 2 edition, 2011.
- [43] D. Moore and J. Reynolds. *X-ray diffraction and the identification and analysis of clay minerals*. Oxford University Press, 2 edition, 1997.
- [44] S. Hendricks and E. Teller. X-ray interference in partially ordered layer lattices. *The Journal of Chemical Physics*, 10, 1942.
- [45] H. Winick. *Synchrotron Radiation Sources: A Primer*. World Scientific, 1994.
- [46] P. R. Griffiths and J. A de Haseth. *Fourier Transform Infrared Spectrometry*. John Wiley & Sons, Inc., 2007.
- [47] Thermo Nicolet. Introduction to fourier transform infrared spectrometry. Information booklet, 2001.
- [48] Andy Hammersley. *FIT2D Reference Manual*. ESRF, 2004.

BIBLIOGRAPHY

- [49] L. A. G. Aylmore. Microporosity in montmorillonite from nitrogen and carbon dioxide sorption. *Clays and Clay Minerals*, 25, 1977.
- [50] Umberto del Pennino, Ezio Mazzega, and Luciano Poppi. Interlayer water and swelling properties of monoionic montmorillonites. *Journal of Colloid and Interface Science*, 84(2), 1981.
- [51] N.T. Skipper, K. Refson, and J. D. C. McConnell. Computer calculation of water-clay interactions using atomic pair potentials. *Clay Minerals*, 24, 1989.
- [52] G. de Koeijer et al. CO₂transport - depressurization, heat transfer and impurities. *Elsevier Energy Procedia*, 4, 2011.
- [53] Antonin Chapoy et al. Effect of common impurities on the phase behaviour of carbon dioxide rich systems: Minimizing the risk of hydrate formation and two-phase flow. *SPE Journal*, 16, 2011.
- [54] Alexandru Botan, Benjamin Rotenberg, Virginie Marry, Pierre Turq, and Benoît Noetinger. Carbon dioxide in montmorillonite clay hydrates: Thermodynamics, structure, and transport from molecular simulation. *Journal of Physical Chemistry C*, 114, 2010.
- [55] Z. Zhou, W. D. Gunter, B. Kadatz, and S. Cameron. Effect of clay swelling on reservoir quality. *Journal of Canadian Petroleum Technology*, 35, 1996.
- [56] Jean-Rémi Butruille and Thomas J. Pinnavaia. Alumina pillared clays a alkylation catalysts. In *Clays: Controlling the Environment*, 1993.
- [57] J. Madejová and P. Komadel. Baseline studies of the clay minerals society source clays: Infrared methods. *Clays and Clay Minerals*, 49, 2001.
- [58] J. M. Green, K. J. C. MacKenzie, and H. J. Sharp. Thermal reactions of synthetic hectorite. *Clays and Clay Minerals*, 18, 1970.
- [59] William F. Jaynes, Samuel J. Traina, and Jerry M. Bigham. Preparation and characterization of reduced-charge hectorites. *Clays and Clay Minerals*, 40(4), 1992.

BIBLIOGRAPHY

- [60] Lawrence E. Bowman, Bruce J. Palmer, Bruce C. Garrett, John L. Fulton, Clement R. Yonker, David M. Pfund, and Scott L. Wallen. Infrared and molecular dynamics study of D₂O rotational relaxation in supercritical CO₂ and Xe. *Journal of Physical Chemistry*, 100, 1996.